NOTE TO USERS

Dynamic Behavior of Drill-Shaft-Drive Assembly Subjected to Cutting Loads

Komanduri Vishnuvardhan Nagarajan

A Thesis

In

The Department

Of

Mechanical and Industrial Engineering

Presented in Partial Fulfillment of the Requirements

for the Degree of Master of Applied Science at

Concordia University

Montréal, Québec,

Canada

February 2005

Your file Votre référence
ISBN: 0-494-04421-7
Our file Notre référence
ISBN: 0-494-04421-7

ABSTRACT

Dynamic Behavior of Drill-Shaft-Drive Assembly Subjected to Cutting Loads

Komanduri Vishnuvardhan Nagarajan

Drilling is one of the most important and common machining operations carried out in manufacturing industry. In drilling, the parameters such as hole-roundness, location and size, and interior surface finish are important for the proper functioning in the assembly. All of these parameters are related to the orbital motion of the drill during the drilling operation, which mainly arises from the lateral vibrations of the twist drill in a plane. In order to understand the dynamics of the process during drilling, a simplified two-dimensional model for the transverse motion of the drill rotating in a hole with clearance is employed. The model can be assumed analogous to that of an unbalanced rotor with a mass-less shaft rotating in a bearing with clearance. When the drill rotates freely in the hole, the overall stiffness is equal to the stiffness of the drill alone. When the drill comes in contact with the workpiece and if the radial displacement of the drill is greater than the radial clearance between the drill and the hole, the stiffness and damping of the workpiece contribute to the overall stiffness and damping of the drill. This introduces non-linearity in terms of discontinuous stiffness. Fourth-order Runge-Kutta method has been employed to solve the governing equations and to obtain the orbital plots of the drill center. The model includes parameters such as the drill rotational speed, clearance between the drill and the hole, stiffness ratio of workpiece and drill, dry friction between the

workpiece and the drill, and cutting force modulation factor. The effects of these parameters on the drill orbital motion and hole-quality of the workpiece are investigated.

Experimental investigations are carried out to identify the factors responsible for the typical orbital motion of twist drill. In the experiments the motion of the spindle was found to be significant and hence the simple two-dimensional model will be inadequate to study the drill dynamics. Hence a finite element analysis (FEA) is performed in order to predict the dynamic behavior, considering the complete machine tool system such as, multiple diameter belt drive pulley, bearings, spindle, chuck (or tool holder) and drill bit. The finite element model results are compared with the measured results and reasonable agreement was seen between the two.

ACKNOWLEDGEMENTS

The author is sincerely thankful to his supervisors Dr. Rama B. Bhat and Dr. V. N. Latinovic for their enthusiastic guidance and continuous support during the course of this work.

I would like to thank the technical support staff in Mechanical and Industrial Engineering Department, John Elliot, Brian Cooper, Gilles Huard, Brad Luckhart, and Danny Juras.

The help and useful discussions during the course of this work are gratefully acknowledged from my colleagues and friends.

Finally, I thank my parents and my brother for their continuous moral support throughout the research period.

TABLE OF CONTENTS

LIST OF FIGURES

LIST OF TABLES

LIST OF SYMBOLS

Notation	Description	Unit
A	Area of cross section	m^2
C_d	Linear damping coefficient	Ns/m
C_{dx}, C_{dy}	Linear damping coefficients in X and Y directions	Ns/m
EI	Flexural rigidity	Nm^2
F_{imb}	Imbalance radial cutting force	N
F_{imb}^{**}	Imbalance cutting force magnitude	N
F_n	Radial impact force	N
F_t	Tangential rub force	N
F_x	Radial rub-impact force in X direction	N
F_y	Radial rub-impact force in Y direction	N
F_{imbx}, F_{imby}	Imbalance cutting forces in X and Y directions	N
F_{nx}, F_{ny}	Random noise forces in X and Y directions	N
F_{sx}, F_{sy}	Side forces in X and Y directions	N
H(R-δ)	Heaviside function	-
I_{xx}, I_{yy}, I_{zz}	Mass moment of inertia	kgm^2
I_x, I_y, I_z	Area moment of inertia	m^4
k	Linear stiffness for zero gap system [28]	N/m

K_d	Stiffness of drill	N/m
K_w	Radial stiffness of workpiece	N/m
K_{dx}, K_{dy}	Drill stiffness in X and Y directions	N/m
l	Length	m
m	Combined rotational mass	kg
N	Rotational speed	rpm
O_d	Drill center	-
O_h	Hole center	-
P	Power transmitted	$watt$
R	Radial displacement of drill	m
T_1	Tight side tension	N
T_2	Slack side tension	N
v	Velocity of belt	m/s
$W(z)$	Lateral deflection of beam	m
X'	Velocity in X direction	m/s
Y'	Velocity in Y direction	m/s
X, Y	Cartesian coordinates defining drill bit displacement	-
x, y	Non-dimensional cartesian coordinates defining drill bit displacement	-
α	Stiffness ratio	-
α^*, β	Mass Proportional and Stiffness Proportional damping constants	-
β^*	Half the angle of groove	rad

δ	Radial clearance between hole and drill	m
θ	Angle of wrap	rad
λ	Amplitude modulation factor	-
μ	Friction coefficient	-
μ_x , μ_y	Friction coefficient in X and Y directions	-
μ^*	Friction coefficient between belt and groove of the pulley	-
υ	Poisson's ratio	-
ξ , ξ_i^*	Damping ratio	-
ρ	Frequency ratio	-
τ	Non-dimensional time	-
ϕ	Phase angle	rad
ω	Forcing frequency	rad/s
ω_n	Natural frequency of the system	rad/s

CHAPTER 1

INTRODUCTION

1.1 General

Twist drill is widely used tool in manufacturing for drilling holes. It consists of a cylindrical body with two helical flutes cut into it. Twist drills are usually made of high speed steel. Of course, a few cheaper varieties are made of high carbon steel. They are made in various sizes to suit the work and are provided with either a tapered shank or cylindrical shank. Figure 1.1 [1] describes the salient geometric features of a standard twist drill.

The shank portion is used for gripping the drill in the machine and the body is the working portion of the drill. The most prominent feature of the drill body is the two helical flutes which end up in two straight cutting lips at their intersection with the conical point surfaces. Such a condition occurs only for predetermined combinations of the flute contour, lead of the helix and the point angle. Thus, if the point angle is changed, the cutting edges become either concave or convex. The rake angle and clearance angles on the cutting lips vary widely from near the web towards the drill periphery.

The distance between the straight cutting edges, called the web thickness, is necessary to protect the drill point and stiffen the drill. The chisel edge formed by the intersection of the two conical surfaces at the web, act as a secondary cutting edge. In order to reduce

the frictional forces between the drill and the hole, the drill diameter is decreased over a portion of its circumference leaving a narrow margin land at the full diameter to support the drill body against the hole-surface.

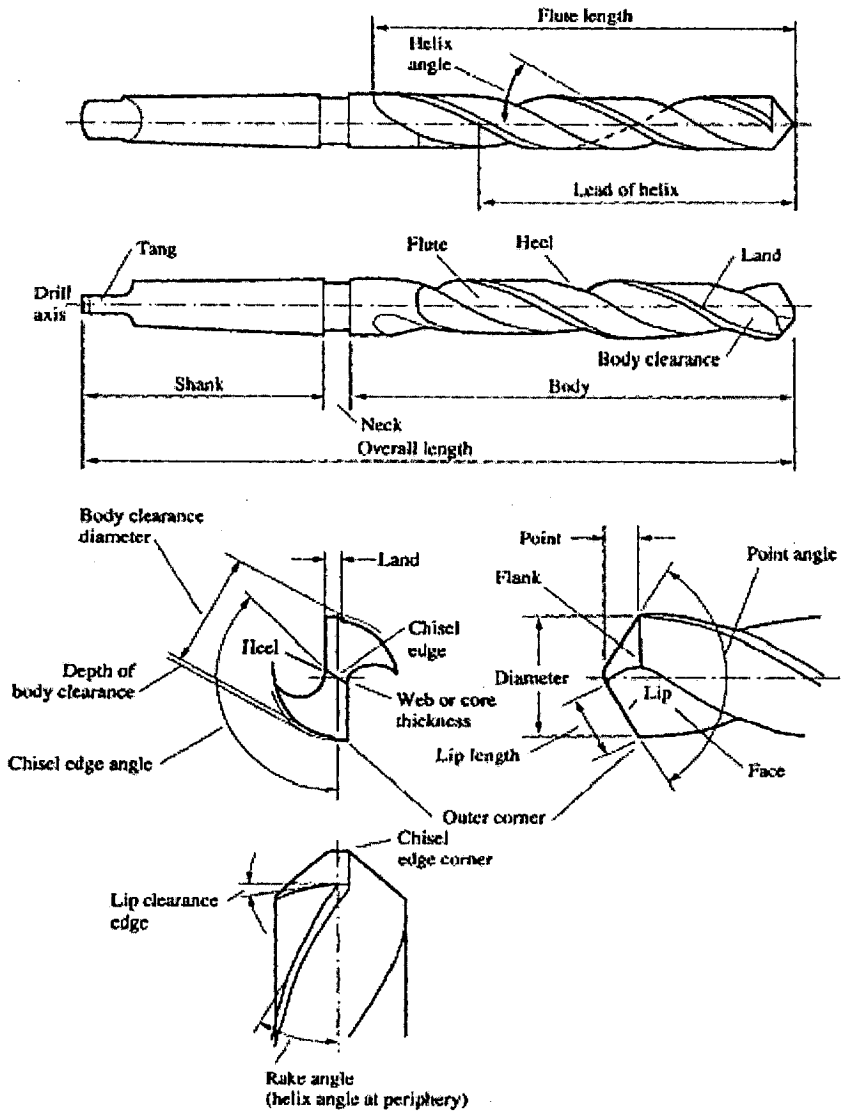

Figure1.1: Drill Geometry [1]

1.2 Drilling Process

The cutting mechanics of a twist drill is unique amongst all metal cutting tools. The cutting velocity developed by the rotation of the tool (with respect to the workpiece) varies widely along the cutting regions starting with zero at the centre and increasing linearly to a maximum at the periphery. This and the variation of the cutting angles together produce vastly differing cutting mechanics-from a severe, extrusion type of process at the chisel edge centre, to normal lathe-tool cutting, at the periphery. As the rotating drill is fed into the work material, the chips produced are removed from the cutting region by the screw action of the helical flutes. The chips traverse the flutes and are ejected at the hole-mouth.

The following virtues are attributed to the twist drilling process:

1. It is a remarkably simple process to generate circular holes.

2. A very simple machine tool is suitable for the purpose, and for small applications, a hand-drill can be used. In general, almost any machine tool that provides a relative rotation between the drill and the workpiece can be used for drilling.

3. A wide range of work materials can be drilled with a standard twist drill and with modifications to the drill point; tough work materials can also be drilled. Tool maintenance is relatively simple-a limited amount of skill is sufficient to regrind drills.

Nevertheless, numerous drawbacks are also associated with drilling, mostly owing to the geometrical characteristics of a twist drill:

1. Chip removal is inefficient at best, requiring frequent withdrawal of the drill to un-clog the chips along the flutes. This limits the maximum depths reachable, and the productivity of the process.

2. Severe cutting process imposes large forces on the drill-tip, leading to undesirable tool-deflection and vibration, in turn resulting in poor quality of holes. This characteristic also imposes limits on the maximum metal-removal rate possible.

3. Tool-life is relatively low (particularly with tough work materials), necessitating frequent tool regrinding.

Although relatively accurate holes can be machined with a standard twist drill, the above factors make twist drilling in general, a mere preliminary operation. If holes require higher accuracy and surface finish, further processing such as reaming, boring, etc., is required. The depth of holes is commonly limited to five to six times the diameter of the drill. In establishing the objectives of the present investigation, a literature survey was carried out and is presented below.

The ability to drill holes of precise size, shape, orientation, and position is important to a wide range of design applications, including joining, assembly and fluid flow, to name a few. It is likely that the hole-quality is influenced by several factors, such as tool geometry, process conditions, drill dynamics, thermal phenomenon, material properties, and the complex interactions of the drill and the hole-wall. Research for understanding these factors affecting the hole-quality started as early as 1860s.

1.3 Survey of Work Done

The extensive use of drilling in the engineering industry has led to consumption of millions of drills per annum, and a correspondingly high expenditure of man-hours and machine-hours have given rise in recent years to an increasing volume of research to improve the efficiency of drilling. Because of vast scale of drilling operations, even a slight increase in the general level of drill performance would yield important practical and economic benefits.

D. F. Galloway [1] has performed experiments to determine the influence of various factors such as drill shape, and particularly to those elements such as relief angle, point angle, relative lip height, which can be controlled by drill user. It was found that the relative lip height has effect on the hole-accuracy. The unbalanced forces acting on the drill with a larger lip height tend to displace the geometric axis of the drill from the axis of rotation towards a position where the resultant forces on the lips are in balance, however, the cutting conditions at the two lips are different which results in lobed holes because of a lateral bending of the drill.

The effect of cutting action on the hole quality was studied by C. H. Kahng, and I. Ham [2]. They also investigated on improving the hole-quality, by using sequential processes like boring and reaming followed by drilling operation. It was found that one can improve the hole-quality only to certain extent and ideal improvements cannot be expected under normal conditions. The inaccuracy in the total spindle-adapter-drill system was found to affect the accuracy of the hole. The spindle-adapter-drill system is

deflected when the drill begins to penetrate the workpiece. As the depth of the hole increases, the deflection of the drill becomes progressively larger, and consequently, the drill path tend to drift further away from true axis. By increasing the feed rate, the thrust forces were affected greatly and lateral displacement in the drill and non-parallelism increased. Due to lack of rigidity in the spindle-adapter-drill system, especially in the drill, it is inevitable that the end of the drill point offsets from the true axis of the system. The causes of roundness error in twist drilling are found to be due to relative lip height, and point centricity in the chisel edge.

R. Venkatraman, J. Lambert, and F. Koenigsberger [3] designed special kind of dynamometers to measure the radial forces generated during drilling. It was found that there was radial-force difference on the drill, and this force difference caused bending of the drill, which in turn caused error in the roundness and parallelism. M. Tsuwa, Y. Hasegawa, and H. Kimura [4] studied the relationship between the radial-forces and oversized hole-geometry in twist drilling, and found that the magnitude of the radial-force is related to the degree of stability in the drilling operation, which is called as walking phenomenon.

The factors affecting the oversize of the holes and parallelism were also studied by M. W. Burnham [5-6]. He found that excessive axial force causes the drill to buckle and the dynamic loads cause the drill bit to vibrate at their natural frequencies, possibly causing the portion of the drilled holes to widen slightly and even deviate from straight line. These problems were found to be particularly apparent when small holes (<2 mm in

diameter) are drilled to depths of 80 diameters and greater. Many authors S. Kaldor, and E. Lenz [7], S. M. Wu, and J. M. Shen [8], T. R. Chandrupautla [9], W. D. Webster, J. Rotberg, and A. Ber [10], S. V. Muthukrishnaselvam, and C. Sujatha [11], E. J. A. Armarego, A. J. R. Smith, and Z. J. Gong [12], C. DE Beer [13], have made considerable contributions to the modeling and optimization of the drill point geometry and drill wear, which affects the hole-accuracy.

A. G. Ulsoy, and O. Tekinalp [14] analyzed the dynamics of twist drill, developing a dynamic model for the transverse vibration of drill bit, and validated it experimentally. The model included the effects of drill rotation speed and feed rate as well as drill bit length, diameter and material properties. The characteristic equation obtained based on the model has two roots at constant rotation speed. At zero rotation speed these roots coincided and when the rotation speed is increased these roots diverge from each other in a linear manner. Thus, when one eigenvalue is increasing, the other one decreased and became zero when the rotation speed of the drill bit reached the zero speed fundamental frequency. This rotation speed is called the critical rotational speed. At this zero fundamental frequency speed the rotating shaft become very soft and even small transverse forces cause large deflections. Thus, it was found that the drill transverse natural frequencies are shown to depend on the rotation speed and transverse instability occurred at a critical speed where the natural frequency vanished.

M. Kronenberg [15], D. D. Rosard [16], B. Dawson, and W. Carneige [17] have done considerable amount of studies pertaining to the helix angle of drill which determines the

ability of the drill to remove chips from the drilled holes, which in turn affects the performance regarding the drilled hole quality. It was found that the resistance of a twisted profile to torsion loading is approximately 85% higher than that of an untwisted bar having the same profile. A possible explanation of the out-of-roundness of certain drilled holes was given by E. B. Magrab, and D. E. Gilsinn [18] with governing systems of differential equations of motion developed by considering the drill bit as a twisted Euler beam under axial loading that is clamped at both ends and were solved for finding the buckling loads, natural frequencies and mode shapes of twist drill. It was found that the obtained modes exhibited a complex out-of-plane twisting-type of motion.

Considering the importance of structural dynamic response of the drilling operation both in terms of drilling hole accuracy, as well as, drill wear and breakage J. C. MacBain, K.G. Harding, and O. Tekinalp [19], M. Kohring [20] studied the vibration modes and frequencies of the drill both in terms of understanding the phenomena governing the drilling process, and in terms of generating appropriate analytical models of the drill's structural dynamic behavior. Vibration modes of drill for different boundary conditions were found using Laser Holographic Interferometry. The holographic results showed, quite clearly, the nature of the drill's mode shapes. For the case of lower modes, the drills responded in a manner quite similar to a simple beam having either clamped-clamped or clamped-hinged boundary conditions. Based on the measured frequencies for the case of the drill blank, it was found that the actual boundary conditions are closer to the classical clamped-clamped case for the first bending and the first torsion mode but closer to the clamped-hinged case for the second and third bending modes. There is, however, some

flexibility and /or clearance at the drill tip-hole interface; it was found that the effect of clearance can cause nonlinear jumps to occur in the drill's natural frequencies that are dependent on the drill's amplitude of vibration. There can also be some flexibility at the drill holder depending on the mass and stiffness characteristics of the holder. This last condition can lead to independent modes of vibration when the holder and drill act as one single elastic structure. It was found that the drill's natural frequencies showed an increasing trend with increasing drill hole-depth. The bending frequencies increase at a rate greater than the torsion frequencies which results in out-of-roundness holes.

The non-circular holes arising due to spin and whirling of the drill and its interaction with the hole boundary was studied by P.G. Reinhall, and D. W. Storti [21]. According to them, when the drill has penetrated completely through the plate, creating a hole, the support of the drill tip is lost and the drill is free to undergo whirling motions due to gyroscopic and centrifugal forces. These forces become very large at high speeds of 20,000-60,000 rpm that are not quite uncommon. Due to its whirling motion, the drill eventually collides with the hole-wall, removes some plate material and bounces away. This process is repeated many times before the drill can be stopped. If the motion is periodic, the drill repeatedly removes material from a few sites around the hole-wall, and a non-circular hole is produced. To study this phenomenon, a simplified model of the drilling process was discussed. The study showed that selecting a drill speed allows the virtual elimination of a specific periodic trajectory and offers a possible remedy for the problem of non-circular-hole production.

A. G. Ulsoy [22] studied the dynamic characteristics of the twist drill by lumped parameter dynamic model in terms of basic geometric and process parameters. The model incorporated the effects of drill length and diameter, as well as rotation speed and feed rate. It is used to represent the general dynamic characteristics of the drill bit both before and during the contact with the workpiece. The results showed that the fundamental natural frequency decreases with increasing rotation speed, and this is confirmed with experimental data. A critical rotation speed exists at which the fundamental natural frequency goes to zero, resulting in transverse instability. This critical speed is increased by decreasing the drill length, increasing drill diameter, or decreasing the feed. Thus high speed drilling of small holes with long drills is clearly the most difficult, from the transverse stability point of view. The model shows that externally applied control forces could be used to increase effective damping and stiffness.

H. Fujii, E. Marui, and S. Ema [23] analyzed the role of chisel edge and the development of whirling vibrations of the drill as the drill penetrates into the workpiece which results in the distorted polygon-like shape of the drilled hole, with its odd number of lobes. Three types of drills with different thicknesses are used for the study; it was found that whirling vibration, which has an elliptical orbit, is a self-exited vibration accompanied by a phase lag with respect to the revolution of workpiece. It was also found that there is a considerable influence of chisel edge on whirling vibration, the restraining effect of the chisel edge on the drill whirling vibration becoming stronger as the chisel length is increased. In addition, the restraining effect of the chisel edge seemed also to increase with an increase in drill feed, probably because of the increase in the unbalanced cutting

force of the chisel edges that acts as a damper against the vibration. When the vibration energy supplied by the regenerative effect at the major cutting edge becomes sufficiently large to exceed the restraining effect of the chisel edge, which usually occurs due to increasing in hole depth, the amplitude of the whirling vibration increases rapidly. The chisel edge was qualitatively found to function as a vibration damper.

In order to predict the initiation boundary of the whirling, H. Fujii, E. Marui, and S. Ema [24] considered drills with varying web thickness, more importantly widely varied point angles, relief angles and helix angles of drill point geometry at the major cutting edge. The influence of flank surface configuration of the major cutting edge was also studied in particular. The analysis of the major cutting edge influence on the vibration showed that a part of the flank surface tends to collide against the workpiece for certain time span in one cycle of whirling and consequently acts as a vibration damper. The tendency is concretely expressed by a flank collision index which represents the flank surface configuration. It was also found that the initiation boundary of the whirling can be predicted from two parameters, one being the chisel edge length, and the other, the flank collision index.

S. J. Lee, K. F. Eman, and S. M. Wu [25] developed a mathematical model to investigate the factors for the drill wandering motion and validated experimentally. The experiments have shown that the penetration of the drill into workpiece results in the skidding of the chisel edge on the surface of the workpiece due to the factors such as chisel edge eccentricity, unbalanced forces due to differences in lip height and half point angles. The

different degrees of sharpness of cutting edges, and transverse deflection of the drill, resulted in the production of distorted polygon-shaped hole always having odd number of sides during drill entry and change in the profile of the hole gradually into round shape with increasing hole-depth. S. Ema, H. Fujii, and E. Marui [26] studied the improvement of drilling accuracy and productivity which depend on whirling vibration of drill considering the vibration analysis in drilling workpiece with a pilot hole. The effect of workpiece rotation, feed rate and pilot hole diameter on the whirling vibrations are examined. The whirling of the drill within four revolutions of workpiece was calculated. The study showed that the drill vibrates at finite amplitude at the beginning and that after half revolution is gradually increased by the regenerative effect. It has been noticed that the whirling vibration is quite regular and its frequency during one revolution of work-piece is about nine. The frequency of the whirling vibration in one workpiece revolution is defined as whirling number. The effect of feed rate and the workpiece number of revolutions on the whirling number shows that all the whirling numbers are odd; therefore a distorted polygon with odd number corresponding to whirling number is formed on the workpiece surface. When the feed rate is faster, the value of whirl number becomes small and is dominated by either 5 or 7 whirl number. The effect of workpiece rotation on whirl number was not found, but when the feed rate is lower, this effect was recognized. When the pilot hole diameter is increased the whirling number increased and vice-versa.

Lateral vibrations of the drill which are responsible for lobed holes produced during drilling are modeled using the Euler-Bernoulli beam theory by O. Tekinalp, and

A. G. Ulsoy [27]. The model included the most important properties of the drill bit and of the drilling operation, such as the cross-sectional geometry, the drill helix angle, rotational speed of the drill bit, the thrust force, torque, and cutting forces generated during drilling. Equations of motion are derived in an inertial frame and then transformed to a rotating fluted frame for convenience of the solution. The transformed equations of motion are discretized using finite element techniques. The model did not include rotary inertia effects, gyroscopic moments, or shear deflection, since these effects are negligible in drill bits that are typically quite slender. The results obtained were found to be in good agreement with the known analytical solutions.

The dynamics of the drill was found to play a crucial role in determining hole-quality. A two-dimensional model for drill bit transverse vibrations which has the same form as a basic rotodynamic model of an unbalanced rotor with mass-less shaft rotating in a bearing with clearance is formulated by S. A. Basile [28]. Such a model helps in identifying valuable process information for controlling the drilling process. It was found that the drill tip wanders away from the desired hole location upon entering the material and while cutting it. The tool vibrates on the side-wall of the hole during the cutting process, causing an oversized and/or out-of- roundness hole with a poor interior surface finish. Factors such as improper sharpening of the drill, cutting force imbalance, drill deflections, and misalignment of the hole-axis are some of the major causes for initial drill wander. However, after drill tip enters into the material, the motion of the drill is confined to the clearance between the drill and the side-wall of the hole. The lobed patterns, three-lobed being the most dominant, were found to be arising from the drill

dynamics. This behavior varies with rotational speed, eccentricity, and the radial-forces experienced during drilling. The studies showed that production of non-circular hole is sensitive to the selection of drill rotation speed, eccentricity of the spindle-drill axis, and modulation of cutting forces. The results showed that the modulation of the cutting force with proper amplitude and phase will change the non-circular holes to a round hole. Also increasing the rotational speed will create a hole that is approximately round. Although the roundness errors will be reduced by parameter selection and/or modulation, the hole-oversize, which is determined by drill tip geometry, will not be significantly reduced and may increase.

A. Stephenson, and J. S. Agapiou [29], performed drilling tests on 3.8 cm × 3.8 cm × 5 cm samples of grey cast iron. Four-component piezoelectric drill dynamometer was used to measure the radial and thrust forces on the drill cutting edges in x and y directions with the drill diameters of 20.7 mm and 21.1 mm, respectively, at rotational speeds of 1150 and 2300 rev/min. The net radial-force was measured to be less than 200 N.

The variation of torque, thrust, and radial cutting forces was also studied by D. M. Rincon, and A. G. Ulsoy [30]. An analytical model for drill bit transverse vibrations was developed for studying the drilling performance resulting in lobed holes, burr formation and tool breakage. The studies showed that the mean cutting forces are not affected by changes in the relative motion of the drill centre. The changes in the relative motion of the drill, however, do affect the variations of forces. There is an increase in the range of torque and thrust for increasing ranges of drill relative motion. The model thus provides a

basic understanding of the mechanisms which give rise to variations in the cutting forces observed.

An extensive work was done by Z. Zhixiong, and L. Cheng [31] on the mechanism of chatter vibration during the initial penetration in drilling, and the drill point skidding on the workpiece at the beginning of the drilling operation which resulted in wandering motion of drill. Experimental investigations through time domain data, orbital plots and power spectrum analysis of displacement and cutting forces was also done. A comparison was made between the situation of the drill rotating with workpiece stationary, and the workpiece rotating with the drill stationary. The mechanism for wandering motion of the drill point is analyzed using the regenerative vibration principle, the velocity component principle and the mode coupling principle. The results showed that at the moment the drill point contacts the workpiece in the penetration process, the chisel edge skids on the workpiece, and then it stabilizes at a new position, and begins to enter the workpiece. The skidding is a random motion which is mainly dependent on the geometry of the chisel edge, workpiece surface, rigidity of the drill and the spindle system, and drill conditions. The polygon like hole due to wandering of the drill in drilling is formed by the bending vibration of the drill point relative to drill body and the rotating motion of the drill point relative to workpiece. When the wandering motion is caused in drilling, the bending vibration of the drill is a regenerative self-excited vibration. All three self-excited vibration principles in metal cutting (i.e., regenerative chatter vibration principle, velocity component principle and mode coupling self-excited principle) are simultaneously reflected in the drill wandering motions.

A study was done by Z. Katz, and A. Poustie [32] on the influence of specific aspects of the drill geometry on the location accuracy of the hole. This work presents a view on the potential dependence of the hole quality on the drill wandering. The study shows that the hole-location accuracy is dependent on the behavior of the drill at the onset of drilling. During the first few revolutions after the contact, the drill point deflects away from the spindle-axis owing to the factors such as workpiece imperfections, chisel edge eccentricity, and walking of chisel edge. The drill does not have a true point but has a flat edge and as the drill rotates while contacting the workpiece the edge walks on its corners around and away from spindle axis. Initially, the drill point is constrained only by the narrow contact area between the main cutting edges and the bottom of the hole. Along the direction perpendicular to the main cutting edges, the point is free to move a substantial distance until the increasing contact forces on the drill point prevent further deflection. Once the outer corners enter the workpiece, the hole-location becomes finalized.

1.4 Objectives and Scope of Work

There are several factors that can potentially influence the quality of the hole of a drilling operation beyond simply choosing the correct machining parameters, and geometric parameters of the drill. Some of these include machine tool itself, the condition of the drill bit, and the dynamics of the process. The structural dynamics of the machine tool, the dynamics of the cutting process and workpiece tool interactions all affect the quality of the hole-profile. In industrial machining operations, it is often assumed that the machine tool system is rigid for the cutting process. This assumption makes machining operation easier to setup and simple to control.

Drilling machines are composed of many sub-assemblies. Spindle is the most important element from a machining stand point. The spindle is the part of the machine that holds the tool and is most directly subjected to the cutting forces during drilling. In addition, the dynamics of the spindle will be transferred directly to the tool, which affects the surface finish and the profile of the hole being drilled. The survey of the work done showed that an extensive study was done regarding the aspects of hole-accuracy, and location. Analytical models were also presented concerning the dynamics of the drill, but all the developed analytical models for the study of structural dynamics considered twist drill alone for the analysis. The present work considers complete machine-tool system and studies the structural dynamics of the complete system.

1.5 Organization of Thesis

In Chapter 1, an introduction to the twist drill nomenclature and the drilling process is explained. A complete literature review is provided, which gives an insight into the research done for analyzing the factors responsible for the production of out-of-roundness holes. It also provides the motivation and scope of the thesis undertaken.

In Chapter 2, a basic two-dimensional mathematical model of a drill rotating in a hole with clearance is considered [28], and the equations of motion for the transverse vibration of the drill bit are derived that identifies the process conditions affecting the hole quality and helps in the interpretation of drilling signal patterns produced during the hole-making process. Simulation results are presented and discussed.

Chapter 3 discusses experimental investigations on the drilling machine/tool system. Details of experimental modal analysis of machine /tool system are also presented.

In Chapter 4, finite element model for the entire machine tool structure is presented. The analysis done using ANSYS 8.1 for the dynamic response of the structure subjected to the cutting forces is also presented.

Chapter 5 presents conclusions of the work undertaken and recommendations for the future work.

CHAPTER 2

TWO-DIMENSIONAL MODEL FOR TRANSVERSE VIBRATIONS OF TWIST DRILL

2.1 Discrete Model Introduction

The two-dimensional model equations for drill bit transverse vibrations as given in [28] form the basis for the present study. The equations of motion derived in this Chapter, help in identifying valuable process information for controlling the drilling process. The drill tip wanders away from the desired hole location upon entering the material and while cutting it. The tool vibrates on the side-wall of the hole during the cutting process, causing an oversized and/or out-of-roundness hole with a poor hole surface finish. Factors such as uneven sharpening of the drill, cutting force imbalance, drill deflections, and misalignment of the hole-axis are some of the major causes for initial drill wander. However, after drill tip enters into the material, the motion of the drill is confined to the clearance between the drill and the side-wall of the hole.

2.2 Formulation of Equations of Motion

In order to derive the transverse motions of the drill vibrating against the side-wall of its hole, a basic rotodynamic model of an unbalanced rotor with a mass-less shaft rotating in a bearing with clearance is considered [28]. The model includes the effect of hole-clearance and cutting force imbalance. The rotating drill bit is considered as a single mass symmetrically supported and rotating in a hole with clearance. The vertical sliding spindle housing, the spindle and the drill bit chuck provide the supporting structure for

the rotating drill bit. These support elements of the rotating drilling system are considered as linear spring and damper elements. The hole in the workpiece causes the overall system stiffness to increase when the transverse motion exceeds the clearance. The overall system stiffness is represented by a bilinear spring. When the drill rubs on the side of the hole, there is an abrupt increase in the radial stiffness of the system and a friction force is generated tangential to the contact surface. The diagram of the simplified model and the coordinate systems used in the derivations of the equations of motion and the forces acting on the drilling systems are shown in the figures 2.2.1 and 2.2.2, respectively.

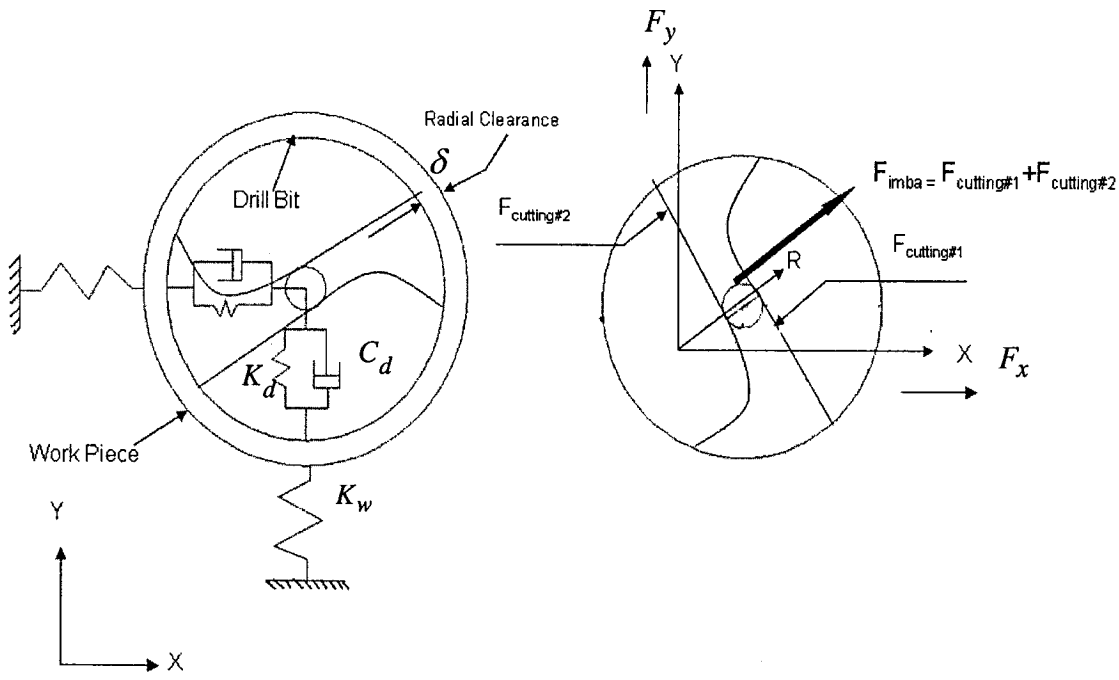

Figure 2.2.1: Simplified Model

Figure 2.2.2: Forces Acting on Drill

The model is excited by an imbalance in the cutting forces, misalignment side forces, and random forces arising during the cutting process. The imbalance forces result from an uneven sharpening of the cutting edges, spindle or tool holder run-out, and uneven wear during the drilling process. The side forces arise as a result of misalignment of the drill and the hole-axes. The random forces result from variations in the microstructure of the workpiece, unevenness in the cutting edges, and fluctuations of the friction forces acting on the drill.

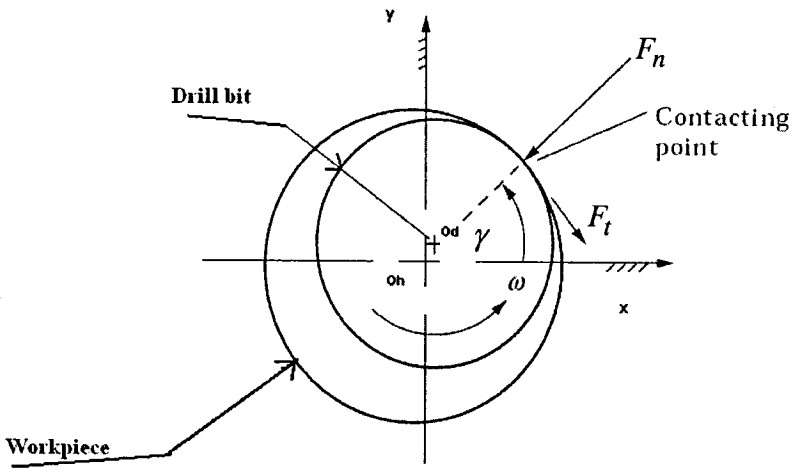

Figure 2.2.3: Two-dimensional Model

The two degree of freedom model of the drill-workpiece system is shown in figure 2.2.1; m is the combined rotational mass of the drill inside the hole with radial clearance δ. With reference to the figure 2.2.3 for the simplest case considered when the drill bit hits the workpiece once during the drilling process the drill makes intermittent contacts with the hole, resulting in a complex dynamic behavior. The centers of the drill

bit and the hole are O_d and O_h, respectively. It is supposed that the workpiece is mass-less, and provides only a stiffness to the drill when it comes in contact with it.

For simplicity it is also assumed that, in X and Y directions, the stiffness coefficients are $K_{dx} = K_{dy} = K_d$, and the damping coefficients $C_{dx} = C_{dy} = C_d$. The non-linearity in the form of discontinuous stiffness is caused by the radial clearance δ between the drill and the workpiece. When the drill freely rotates in the hole, the overall stiffness of the system is equal to the stiffness of the drill K_d alone. If the drill and the workpiece come in contact and if the radial displacement of the drill exceeds the clearance δ, the stiffness of the workpiece K_w contributes to the overall system stiffness. When rub happens during the process of cutting as shown in the figure 2.2.3, the radial impact force F_n and the tangential rub force F_t can thus be expressed as

$$F_t = \mu F_n \text{ where, } F_n = \begin{cases} 0, for R < \delta \\ (R-\delta)K_w, for R \geq \delta \end{cases} \quad (1)$$

where μ is the coefficient of friction between the drill land and the wall of the hole. The frictional force produced due to the rubbing will be acting in the opposite direction of motion. Let μ_x and μ_y represents the coefficients of friction (Coloumb) in X and Y directions, respectively.

Further, K_w is the radial stiffness of workpiece and $R = \sqrt{X^2 + Y^2}$ is the radial displacement of the drill bit. The free body diagram showing the forces acting on the drill is given in the figure 2.2.2, where F_x and F_y represent the rub-impact forces in the

directions X and Y, respectively. These forces arise whenever the radial displacement of drill bit exceeds the clearance and the forces are given by,

$$F_x = -F_n \cos\gamma + F_t \sin\gamma \tag{2}$$

$$F_y = -F_n \sin\gamma - F_t \cos\gamma \tag{3}$$

where, $\cos\gamma = \frac{X}{R}$ and $\sin\gamma = \frac{Y}{R}$ so that

$$F_x = -\left(\frac{R-\delta}{R}\right) K_w (X - \mu_x Y) H(R-\delta) \tag{4}$$

$$F_y = \frac{R-\delta}{R} K_w (-Y - \mu_y X) H(R-\delta) \tag{5}$$

where, $H(R-\delta)$ is Heaviside function.

The Heaviside step function is defined as a discontinuous function whose value is zero for negative inputs and one elsewhere. $H(x)=0$ for $x \le 0$ and $H(x)=1$ for $x>0$. The Heaviside function is often used in differential equations as a "switch", for example, to model a system where a steady force is applied after a certain time, but not before. Hence, $H(R-\delta)=0$ for $R \le \delta$ and $H(R-\delta)=1$ for $R > \delta$.

If F_{imbx}, F_{imby} represent the imbalance forces (differences in forces on cutting edges) acting on the drill in X and Y directions, respectively, the equations of motion in Cartesian form are given by

$$m\ddot{X} + C_d \dot{X} + K_d X = F_x + F_{imbx} + F_{sx} + F_{nx} \tag{6}$$

$$m\ddot{Y} + C_d \dot{Y} + K_d Y = F_y + F_{imby} + F_{sy} + F_{ny} \tag{7}$$

where, F_{sx}, F_{sy} and F_{nx}, F_{ny} are side forces and random noise forces in X and Y directions, respectively, and $\ddot{X} = \frac{d^2X}{dt^2}$, $\dot{X} = \frac{dX}{dt}$, $\ddot{Y} = \frac{d^2Y}{dt^2}$, and $\dot{Y} = \frac{dY}{dt}$. The equations of motion (6) and (7) are non-dimensionalized in order to compare behavior of different physical systems. The following non-dimensional groups are introduced [28]:

$$\left.\begin{aligned} &\text{Damping ratio, } \xi = \frac{C_d}{2m\omega_n}, \text{ Stiffness ratio, } \alpha = \frac{K_w}{K_d}, \text{ and} \\ &\text{Frequency ratio, } \rho = \frac{\omega}{\omega_n}, \text{ where } \omega_n = \sqrt{\frac{k}{m}} \text{ and } k = \frac{4K_dK_w}{\left(\sqrt{K_d}+\sqrt{K_w}\right)^2} \end{aligned}\right\} \quad (8)$$

The time t is non-dimensionalized as $\tau = t\omega_n$ and the displacements X, Y are non-dimensionalized by radial clearance (gap) δ, $\frac{X}{\delta} = x$ and $\frac{Y}{\delta} = y$. Now considering the equation (6) and rewriting the equation by substituting F_x from (4) and with $\mathrm{H} = H(R-\delta)$ we get,

$$m\frac{d^2X}{dt^2} + C_d\frac{dX}{dt} + K_dX = -\left(\frac{R-\delta}{R}\right)K_w(X-\mu_xY)H(R-\delta) + F_{imbx} + F_{sx} + F_{nx}$$

$$m\frac{d^2X}{dt^2} + C_d\frac{dX}{dt} + K_dX + HK_wX\left(1-\frac{\delta}{\sqrt{X^2+Y^2}}\right) - H\mu_xK_wY\left(1-\frac{\delta}{\sqrt{X^2+Y^2}}\right) = F_{imbx} + F_{sx} + F_{nx}$$

$\frac{dX}{dt} = \frac{dX}{d\tau} \times \frac{d\tau}{dt}$ and $\tau = t\omega_n$ hence,

$$\frac{d\tau}{dt} = \omega_n, \frac{dX}{dt} = \frac{dX}{d\tau}\omega_n, \frac{d^2X}{dt^2} = \frac{d^2X}{d\tau^2}\omega_n^2$$

$$m\omega_n^2 \frac{d^2X}{d\tau^2} + C_d\omega_n \frac{dX}{d\tau} + K_d X + HK_w X\left(1 - \frac{\delta}{\sqrt{X^2+Y^2}}\right) - H\mu_x K_w Y\left(1 - \frac{\delta}{\sqrt{X^2+Y^2}}\right) = F_{imbx} + F_{sx} + F_{nx}$$

Dividing through out by $m\omega_n^2$ we get,

$$\frac{d^2X}{d\tau^2} + \frac{C_d\omega_n}{m\omega_n^2}\frac{dX}{d\tau} + \frac{K_d X}{m\omega_n^2} + \frac{HK_w X}{m\omega_n^2}\left(1 - \frac{\delta}{\sqrt{X^2+Y^2}}\right) - \frac{H\mu_x K_w Y}{m\omega_n^2}\left(1 - \frac{\delta}{\sqrt{X^2+Y^2}}\right) = \frac{F_{imbx}}{m\omega_n^2} + \frac{F_{sx}}{m\omega_n^2} + \frac{F_{nx}}{m\omega_n^2}$$

Now dividing through-out by the clearance gap δ we get,

$$\frac{d^2\left(\frac{X}{\delta}\right)}{d\tau^2} + \frac{C_d\omega_n}{m\omega_n^2}\frac{d\left(\frac{X}{\delta}\right)}{d\tau} + \frac{K_d\left(\frac{X}{\delta}\right)}{m\omega_n^2} + \frac{HK_w\left(\frac{X}{\delta}\right)}{m\omega_n^2}\left(1 - \frac{\delta}{\sqrt{X^2+Y^2}}\right) - \frac{H\mu_x K_w\left(\frac{Y}{\delta}\right)}{m\omega_n^2}\left(1 - \frac{\delta}{\sqrt{X^2+Y^2}}\right) = \frac{F_{imbx}}{m\omega_n^2\delta} + \frac{F_{sx}}{m\omega_n^2\delta} + \frac{F_{nx}}{m\omega_n^2\delta}$$

From the relations considered in (9) and from $\frac{X}{\delta} = x, and \frac{Y}{\delta} = y$ we get,

$$\frac{d^2(x)}{d\tau^2} + 2\xi\frac{d(x)}{d\tau} + \frac{K_d}{k}x + H\frac{K_w}{k}x\left(1 - \frac{1}{\sqrt{x^2+y^2}}\right) - H\mu_x\frac{K_w}{k}y\left(1 - \frac{1}{\sqrt{x^2+y^2}}\right) = \frac{F_{imbx}}{k\delta} + \frac{F_{sx}}{k\delta} + \frac{F_{nx}}{k\delta}$$

From, $k = \frac{4K_dK_w}{\left(\sqrt{K_d}+\sqrt{K_w}\right)^2}$, $\alpha = \frac{K_w}{K_d}$ we can obtain a relation for K_w and K_d in terms of α so that, $\frac{K_d}{k} = \frac{\left(1+\sqrt{\alpha}\right)^2}{4\alpha}, \frac{K_w}{k} = \frac{\left(1+\sqrt{\alpha}\right)^2}{4}$.

Hence, the equation can now be expressed in non-dimensional form as,

$$\ddot{x} + 2\xi\dot{x} + \frac{\left(1+\sqrt{\alpha}\right)^2}{4\alpha}x + H\frac{\left(1+\sqrt{\alpha}\right)^2}{4}x\left(1 - \frac{1}{\sqrt{x^2+y^2}}\right) - H\mu_x\frac{\left(1+\sqrt{\alpha}\right)^2}{4}y\left(1 - \frac{1}{\sqrt{x^2+y^2}}\right) = \frac{F_{imbx}}{k\delta} + \frac{F_{sx}}{k\delta} + \frac{F_{nx}}{k\delta} \quad (9)$$

where, $\ddot{x} = \frac{d^2x}{d\tau^2}$, and $\dot{x} = \frac{dx}{d\tau}$.

Since the system is symmetric, the equations of motion in the non-dimensional form for y-direction follow the same procedure and hence, it can be expressed as,

$$\ddot{y}+2\xi\dot{y}+\frac{\left(1+\sqrt{\alpha}\right)^2}{4\alpha}y+H\frac{\left(1+\sqrt{\alpha}\right)^2}{4}y\left(1-\frac{1}{\sqrt{x^2+y^2}}\right)+H\mu_y\frac{\left(1+\sqrt{\alpha}\right)^2}{4}y\left(1-\frac{1}{\sqrt{x^2+y^2}}\right)=\frac{F_{imby}}{k\delta}+\frac{F_{sy}}{k\delta}+\frac{F_{ny}}{k\delta} \tag{10}$$

where, $\ddot{y}=\frac{d^2y}{d\tau^2}$, and $\dot{y}=\frac{dy}{d\tau}$.

2.3 Cutting Force Imbalance Consideration

The cutting action of the twist drill is complex in nature and the radial-forces provide a good indication of the drill radial motions. S. A. Basile [28] performed experiments for finding the radial-forces and the thrust forces. He found that the thrust force exhibited oscillation at three times the drill bit rotational speed and it was also found that the radial and axial motions have a direct effect on the drilling process. This effect was represented as amplitude modulation of cutting forces. Hence the imbalance forces are given by,

$$F_{imbx}=F^*_{imb}\{1-\lambda\sin(3\rho\tau)\}\cos(\rho\tau+\phi) \text{ and} \tag{11}$$

$$F_{imby}=F^*_{imb}\{1-\lambda\sin(3\rho\tau)\}\sin(\rho\tau+\phi) \tag{12}$$

Where λ is an amplitude modulation factor and ϕ is phase angle, the forces, (11) and (12) are substituted in the equations of motion (9) and (10) respectively, which gives the complete equations of motion for the forced vibrations.

2.4 Stiffness Ratio

The stiffness ratio α indicates the degree of nonlinearity of the system, and a value of one indicates a linear stiffness model. To estimate the stiffness ratio, the radial stiffness without contacting the side-wall of the hole is modeled as a cantilever beam with the mass lumped at half length, and the radial stiffness when contacting the side-wall of the hole is modeled as the stiffness of a beam fixed at one end, and hinged at the drill tip with mass lumped at half the length.

Case i: Radial stiffness of the drill when it is not in contact with the hole. The drill is considered as a cantilever beam. Let l be the length of the cantilever beam with area of cross-section A , flexural rigidity EI , where I is the moment of inertia of the cross-section of the cantilever about neutral axis, and E is the modulus of elasticity. The beam is shown in the figure 2.4.1.

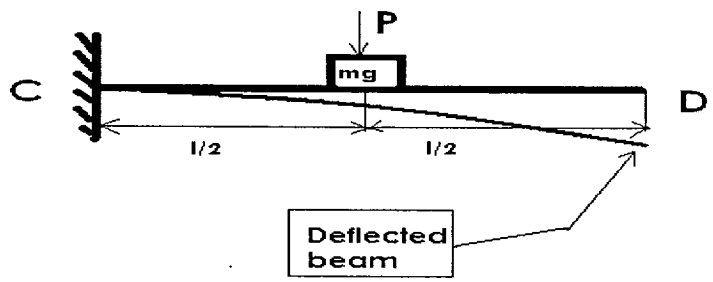

Figure 2.4.1: Lumped Mass Beam Model without Touching the Workpiece

Considering the mass of the beam lumped at a distance $\frac{l}{2}$ from fixed end **C**, the deflection at the mid span of the beam is given by

$W = \left(\frac{Pl^3}{24EI}\right)$ and the stiffness , $K_d = \left(\frac{24EI}{l^3}\right)$.

Case ii: Radial stiffness of the drill when it is in contact with the hole.

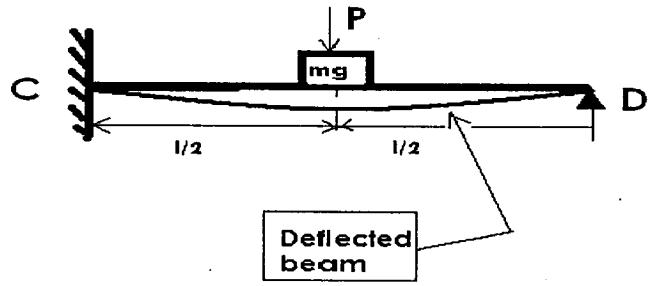

Figure 2.4.2: Lumped Mass Beam Model with Touching the Workpiece

For this case, the beam will be fixed at one end and propped at the other, due to which a reaction force will exist at the propped end as shown in the figure 2.4.3.

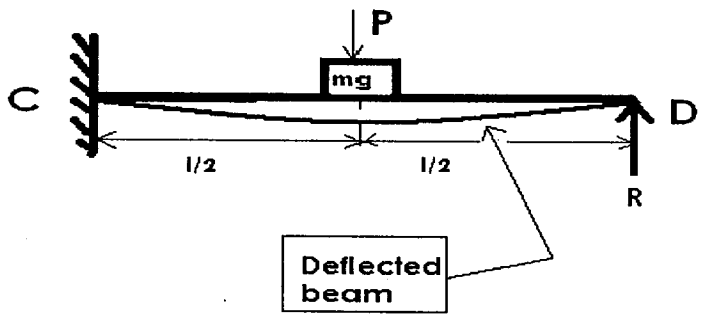

Figure 2.4.3: Lumped Mass Beam Model with Reaction Force

Since the deflection is zero at the end **D**, the deflection at mid span of the beam can be obtained as,

$$EIW = -\frac{5}{96}P\frac{l^3}{8} + \frac{Pl^2}{32}\frac{l}{2}, \text{ and hence, } W = \frac{7}{768}\left(\frac{Pl^3}{EI}\right)$$

The radial stiffness for this case is $K_T = \frac{768EI}{7l^3}$

Since, $K_T = K_d + K_W$ hence the work piece stiffness is given by

$$K_W = \frac{768EI}{7l^3} - \frac{24EI}{l^3} = \left(\frac{600EI}{7l^3}\right)$$

Hence, the stiffness ratio $\alpha = \left(\frac{\frac{600\ EI}{7l^3}}{24\ \frac{EI}{l^3}}\right) = 3.57$

2.5 Simulation Results

The following simulation results consist of orbits of drill central line motion obtained by plotting the time varying displacements in x and y directions, by solving the equations (10) and (11) for various values of stiffness ratio α, amplitude modulation factor λ, forcing frequency N, and force imbalance ratio $\frac{F^*_{imb}}{k\delta}$ using the fourth-order Runge-Kutta method.

2.5.1 Drill Central Line Motion (Varying α)

Figures 2.5.1 to 2.5.10 show the drill central line motions obtained in x and y directions by considering damping ratio ξ 0.07, force imbalance ratio $\frac{F^*_{imb}}{k\delta}$ of 0.2, modulation factor λ of 1.3, coefficient of friction 0.25, forcing frequency N of 41.9 rad/sec (400 rpm), which is also the rotational speed of the drill, F_{sx}, F_{sy}, F_{nx}, and $F_{ny} = 0$, and for various values of stiffness ratio α as simulation parameters. In all the figures, a three lobed type of orbital response is observed. The variation in the stiffness ratio resulted in the change in the orbit amplitude but did not affect the shape of the orbit. For all the above cases a radial clearance gap δ of 0.038 mm, and measured natural frequency [28] of 507.1 rad/sec (80.7 Hz) is considered.

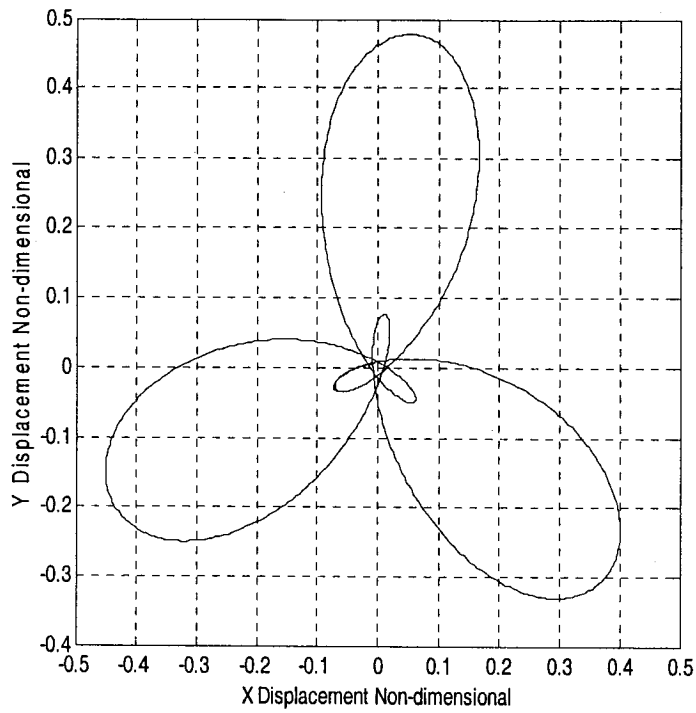

Figure 2.5.1: Orbit of Drill Central Line Motion for $\alpha = 1$

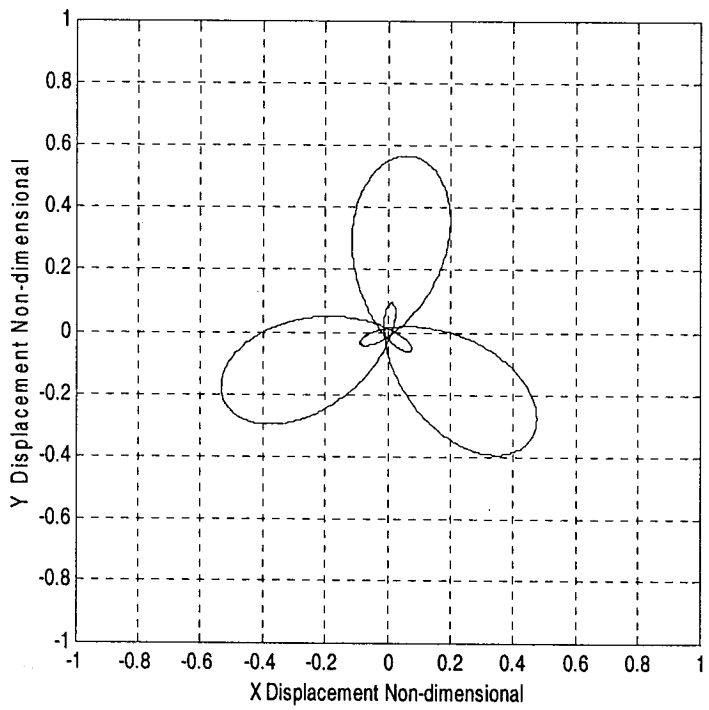

Figure 2.5.2: Orbit of Drill Central Line Motion for $\alpha = 1.4$

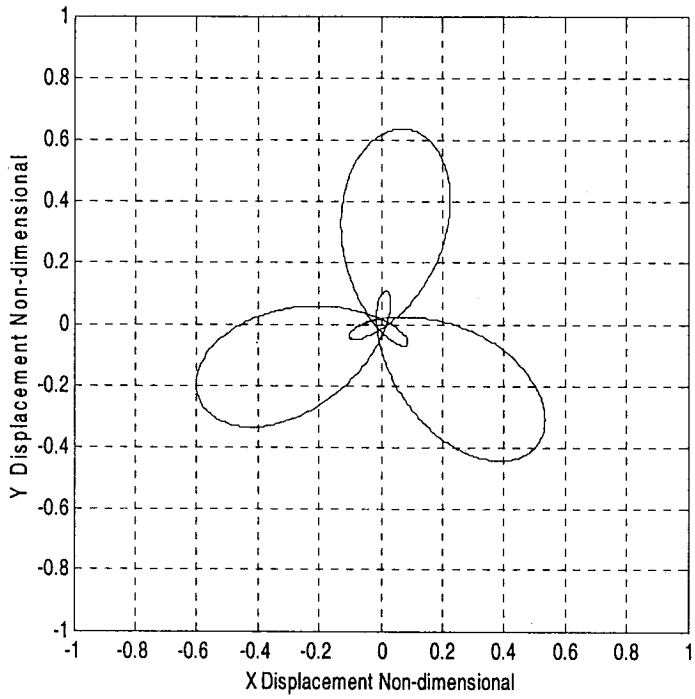

Figure 2.5.3: Orbit of Drill Central Line Motion for $\alpha = 1.8$

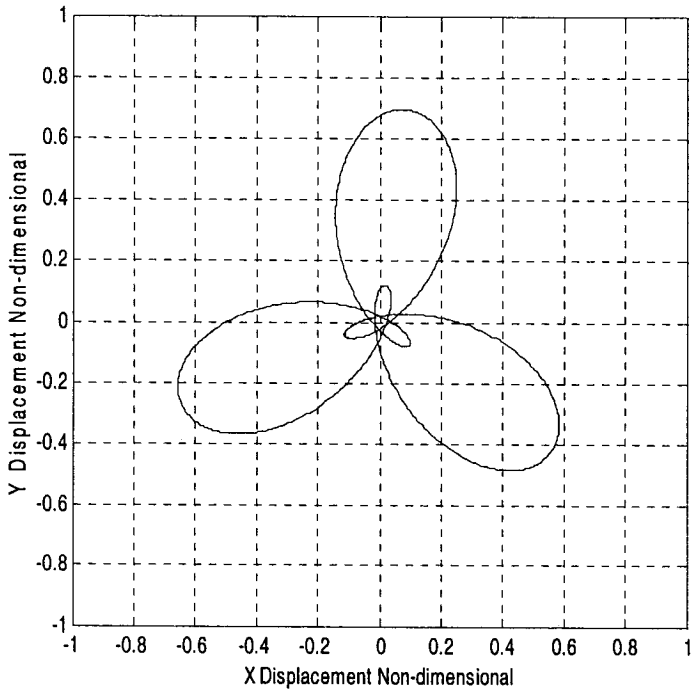

Figure 2.5.4: Orbit of Drill Central Line Motion for $\alpha = 2.2$

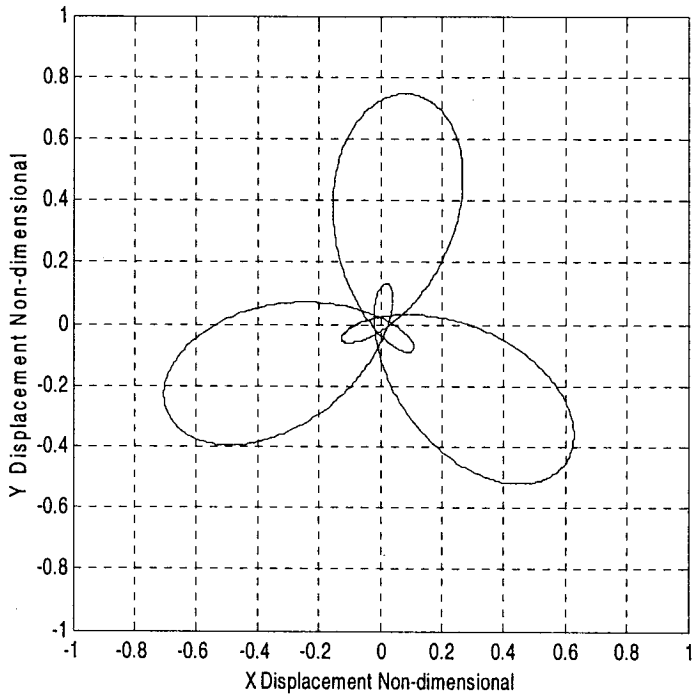

Figure 2.5.5: Orbit of Drill Central Line Motion for $\alpha = 2.6$

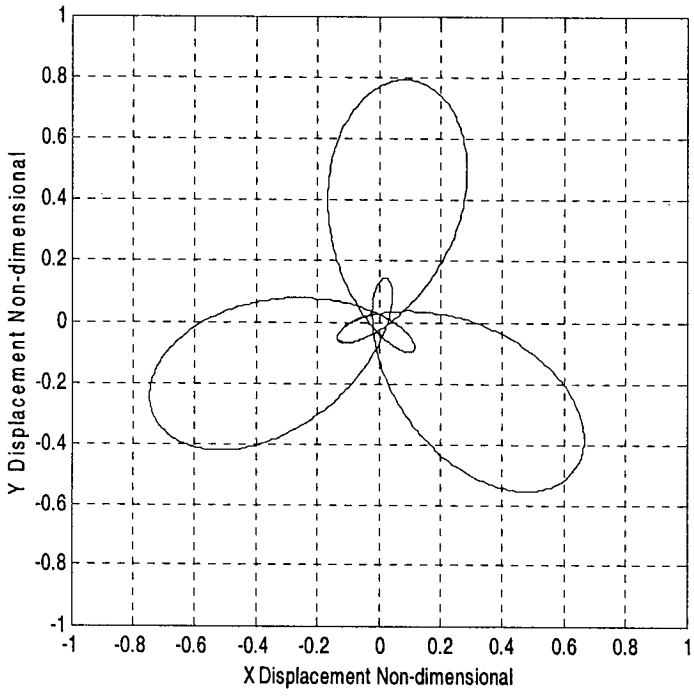

Figure 2.5.6: Orbit of Drill Central Line Motion for $\alpha = 3$

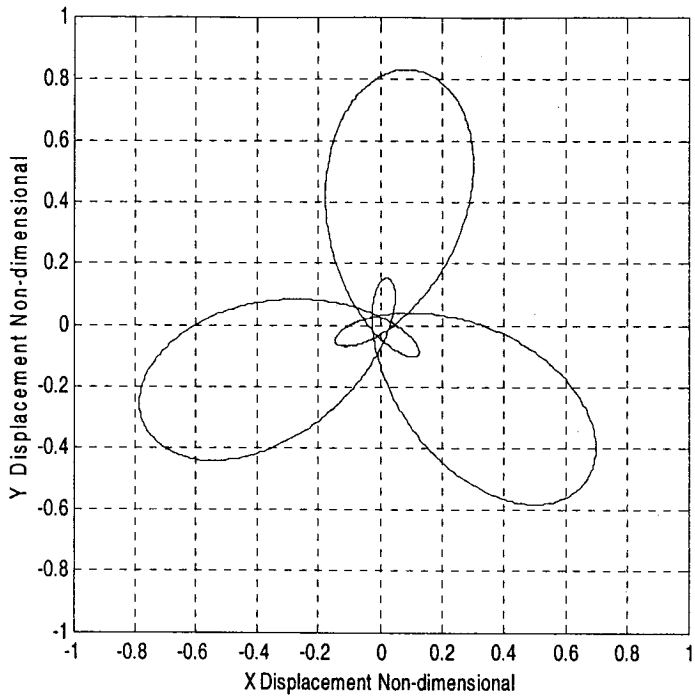

Figure 2.5.7: Orbit of Drill Central Line motion for $\alpha = 3.4$

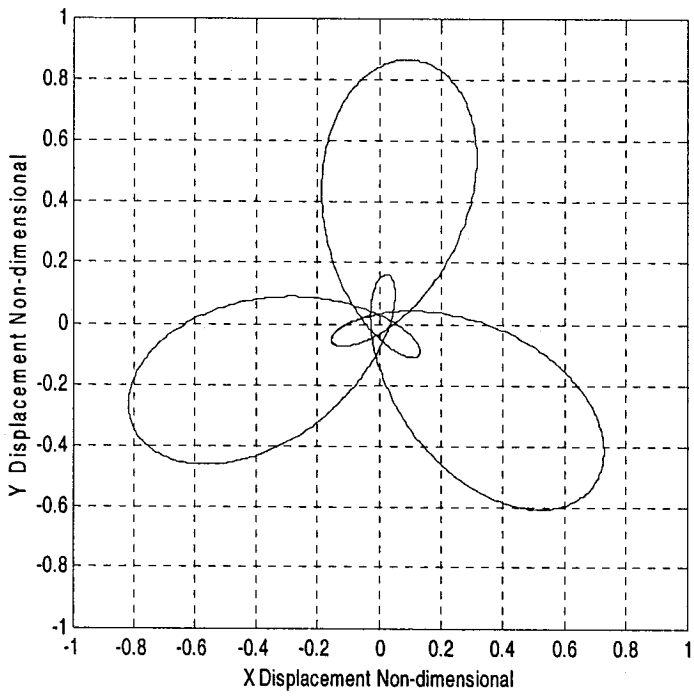

Figure 2.5.8: Orbit of Drill Central Line Motion for $\alpha = 3.8$

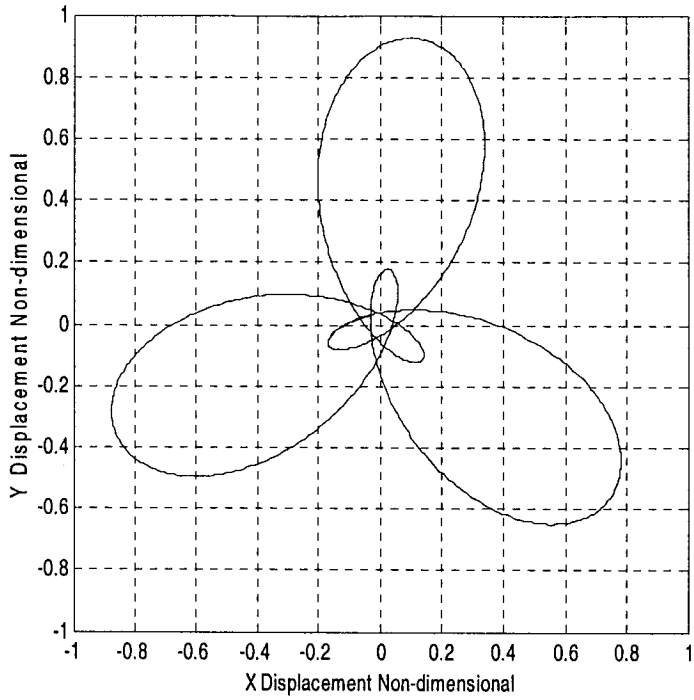

Figure 2.5.9: Orbit of Drill Central Line Motion for $\alpha = 4.2$

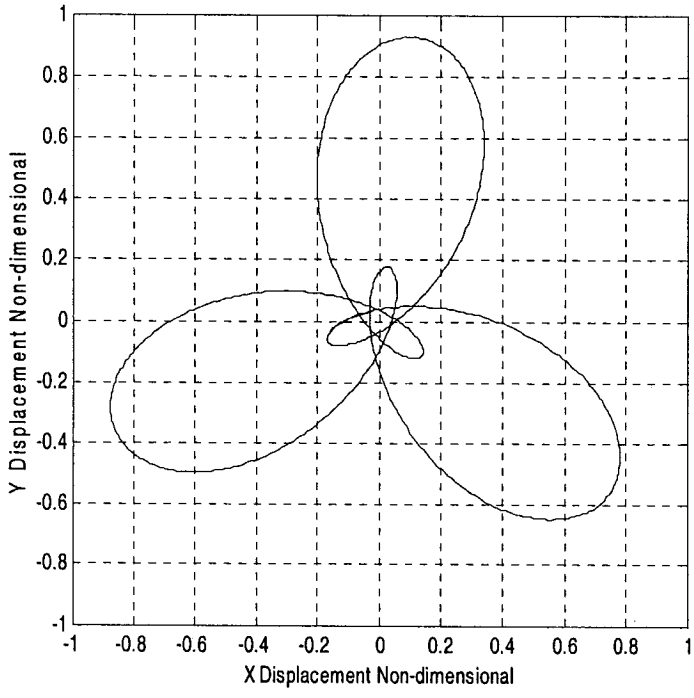

Figure 2.5.10: Orbit of Drill Central Line Motion for $\alpha = 4.6$

2.5.2 Drill Central Line Motion (Varying λ)

For the figures 2.5.11 to 2.5.17 the simulation parameters used are, damping ratio ξ of 0.07, force imbalance ratio $\frac{F^*_{imb}}{k\delta}$ of 0.2, coefficient of friction 0.25, forcing frequency N of 41.9 rad/sec (400 rpm), stiffness ratio α of 4.57, F_{sx}, F_{sy}, F_{nx}, and $F_{ny} = 0$, and for various values of modulation factor λ. The change in the modulation factor has resulted change in the orbital shape from circle to a three lobed pattern, as well as, change in the amplitude of the orbit. For all the above cases a radial clearance gap δ of 0.038 mm, and measured natural frequency [28] of 507.1 rad/sec (80.7 Hz) is considered.

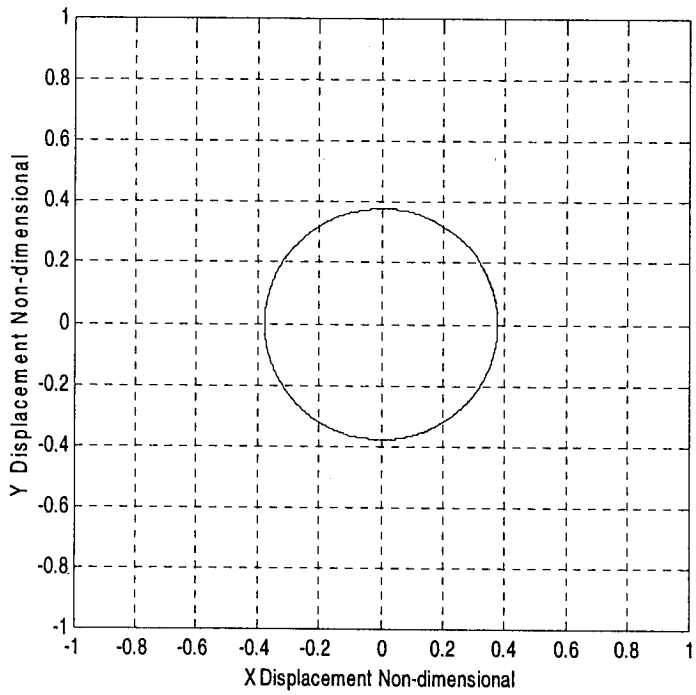

Figure2.5.11: Orbit of Drill Central Line Motion for $\lambda = 0$

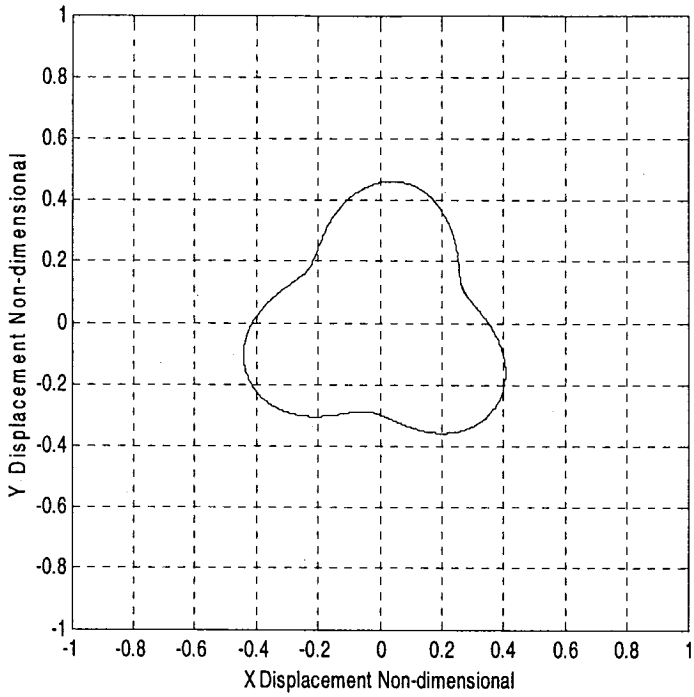

Figure 2.5.12: Orbit of Drill Central Line Motion for $\lambda = 0.2$

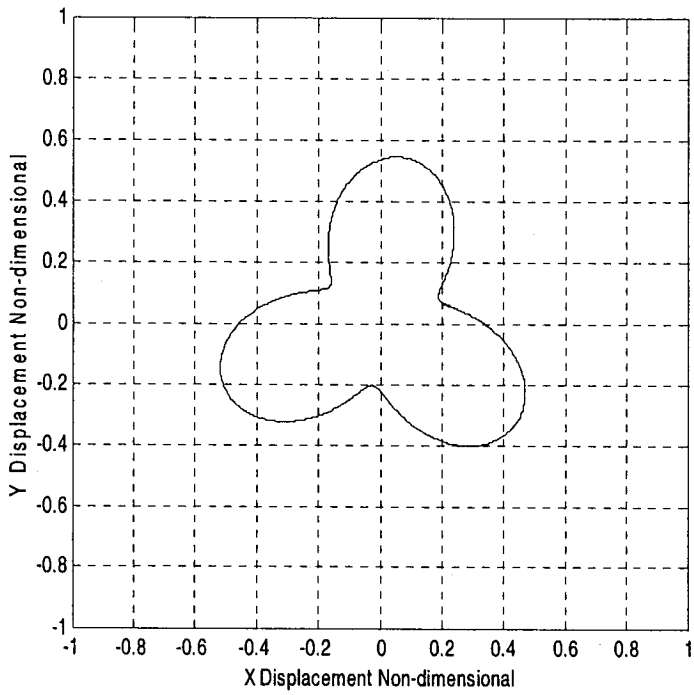

Figure 2.5.13: Orbit of Drill Central Line Motion for $\lambda = 0.4$

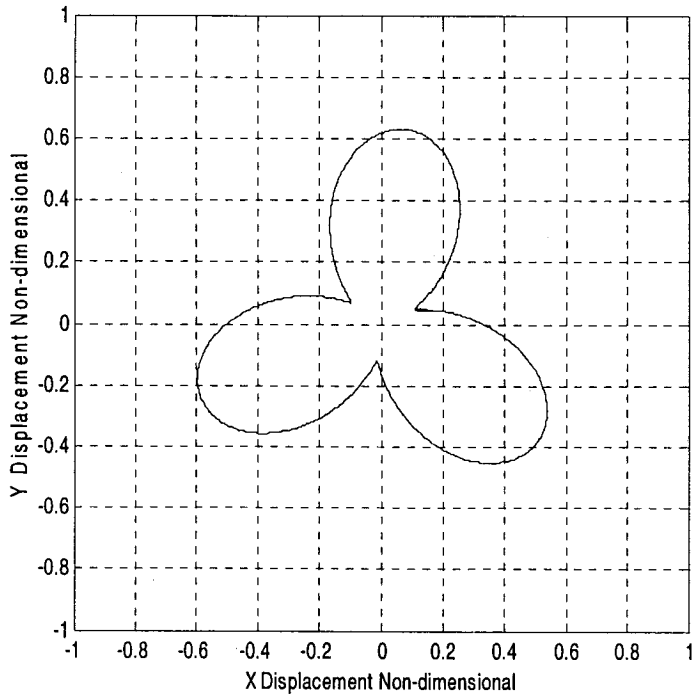

Figure 2.5.14: Orbit of Drill Central Line Motion for $\lambda = 0.6$

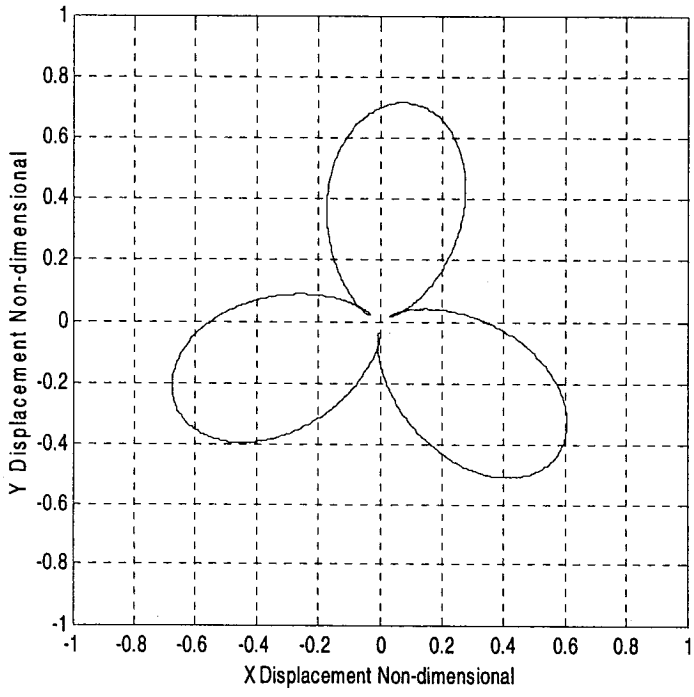

Figure 2.5.15: Orbit of Drill Central Line Motion for $\lambda = 0.8$

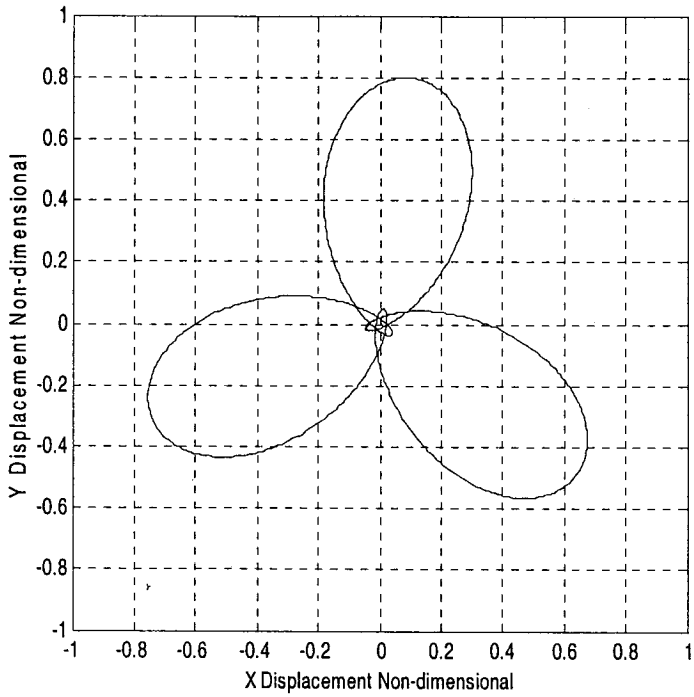

Figure 2.5.16: Orbit of Drill Central Line Motion for $\lambda = 1$

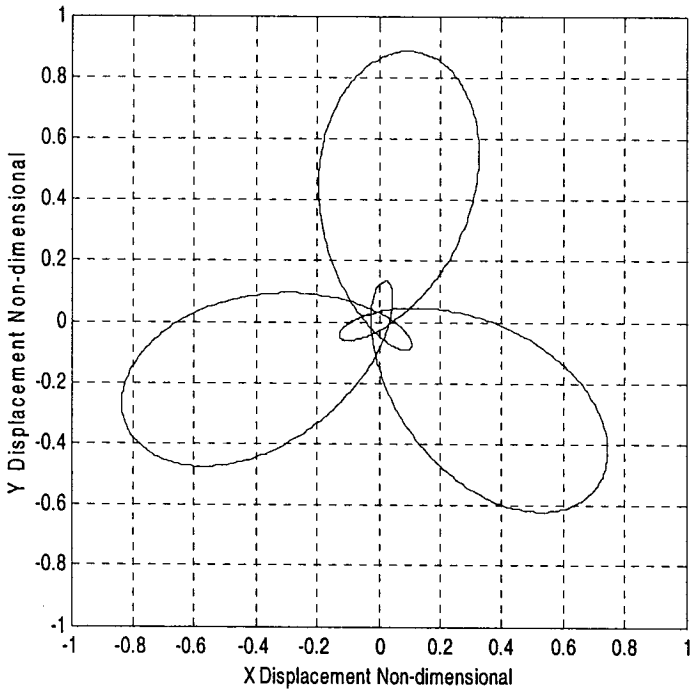

Figure 2.5.17: Orbit of Drill Central Line Motion for $\lambda = 1.2$

2.5.3 Drill Central Line Motion (Varying N)

For the figures 2.5.18 to 2.5.32 the simulation parameters used are damping ratio ξ of 0.07, force imbalance ratio $\frac{F^*_{imb}}{k\delta}$ of 0.2, coefficient of friction 0.25 and stiffness ratio α of 4.57, F_{sx}, F_{sy}, F_{nx}, and $F_{ny} = 0$, and for various values of forcing frequency. The variation of forcing frequency resulted in the change in the shape and amplitude of the orbit. For all the above cases a radial clearance gap δ of 0.038 mm, and measured natural frequency [28] of 507.1 rad/sec (80.7 Hz) is considered.

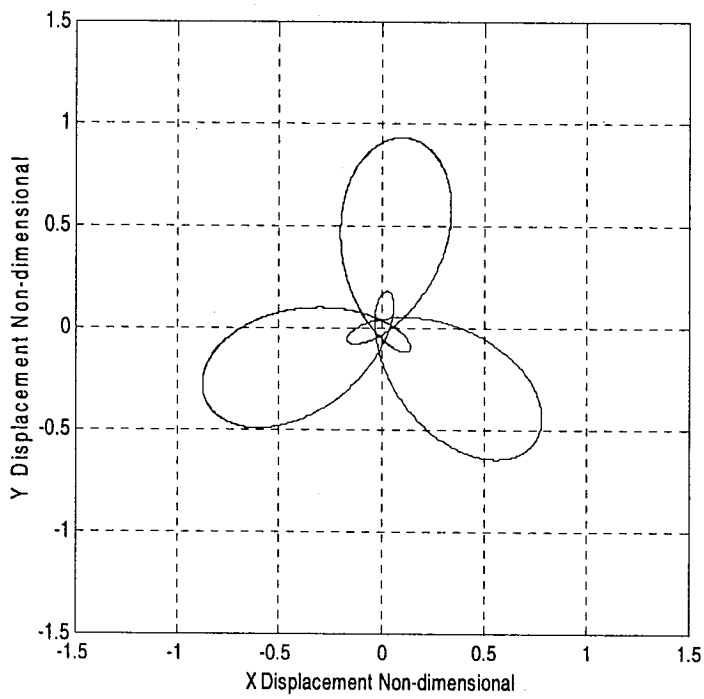

Figure 2.5.18: Orbit of Drill Central Line Motion for N= 400 rpm

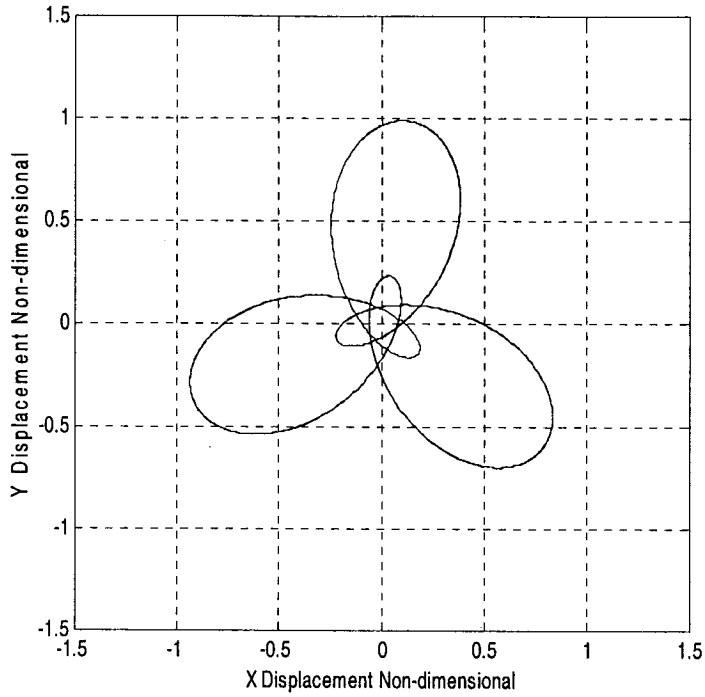

Figure 2.5.19: Orbit of Drill Central Line Motion for N=500 rpm

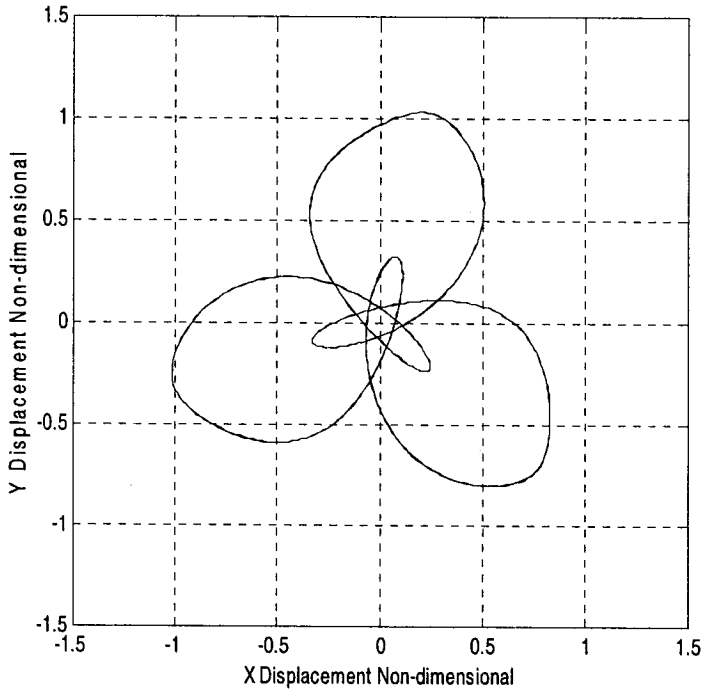

Figure 2.5.20: Orbit of Drill Central Line Motion for N=600 rpm

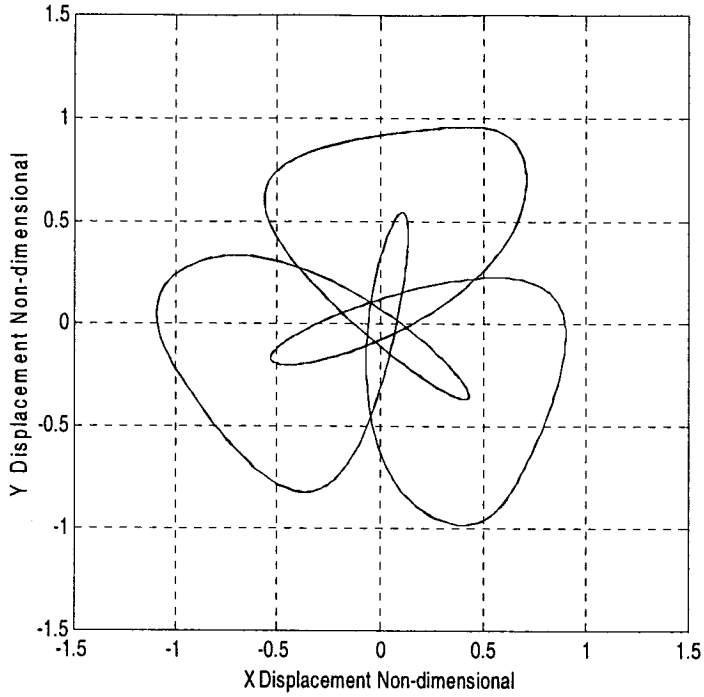

Figure 2.5.21: Orbit of Drill Central Line Motion for N=700 rpm

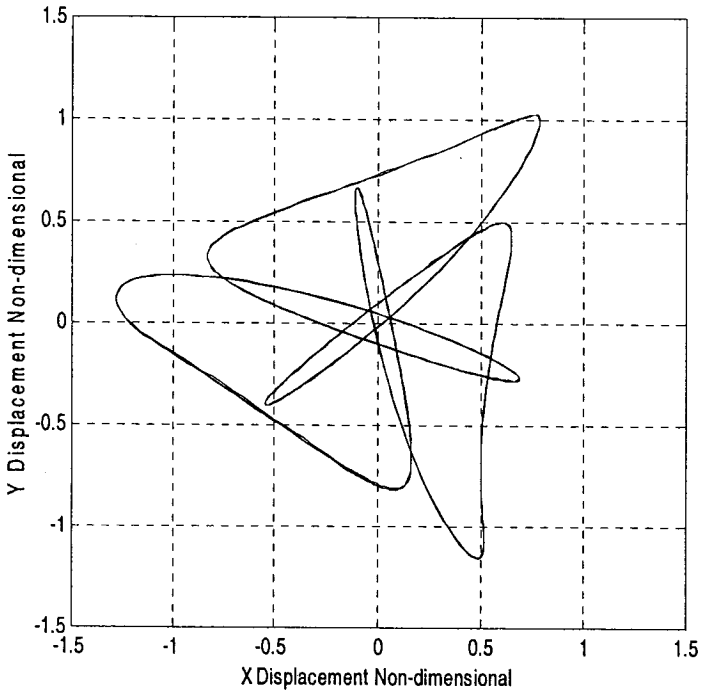

Figure 2.5.22: Orbit of Drill Central Line Motion for N=800 rpm

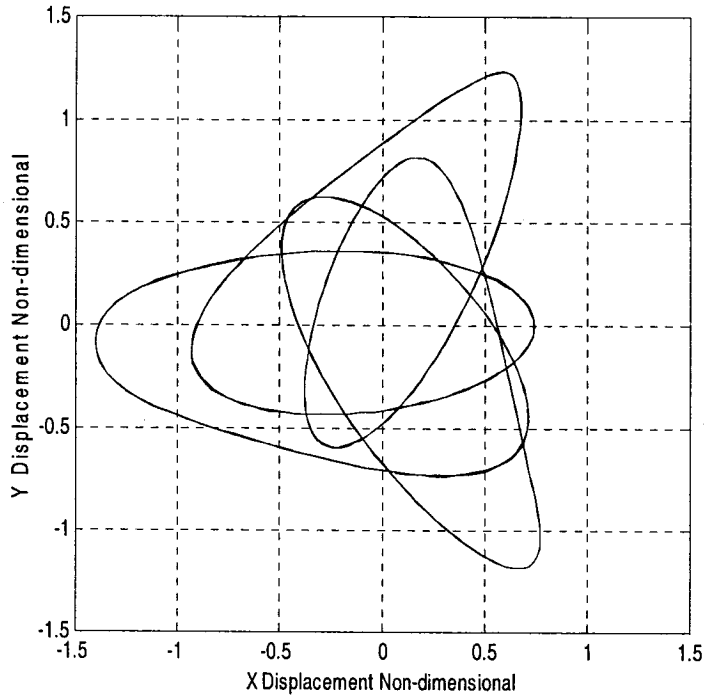

Figure 2.5.23: Orbit of Drill Central Line Motion for N=900 rpm

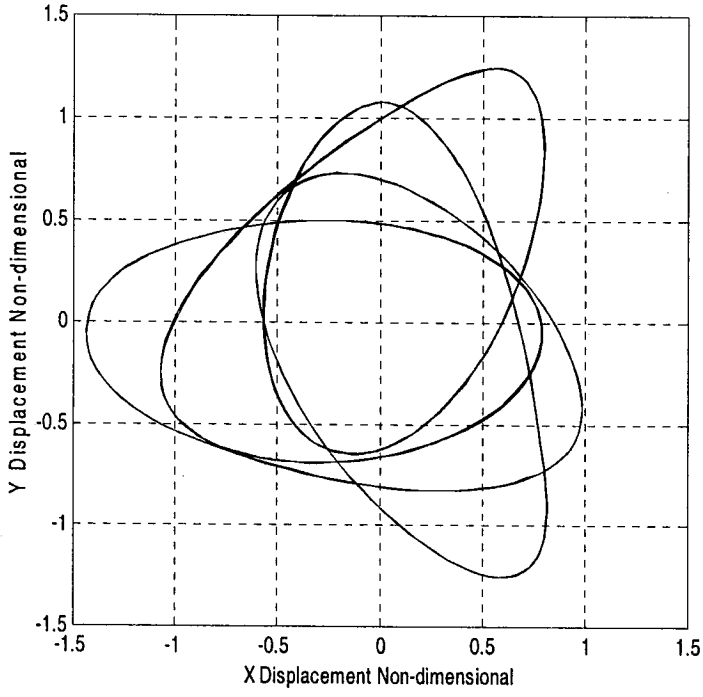

Figure 2.5.24: Orbit of Drill Central Line Motion for N=1000 rpm

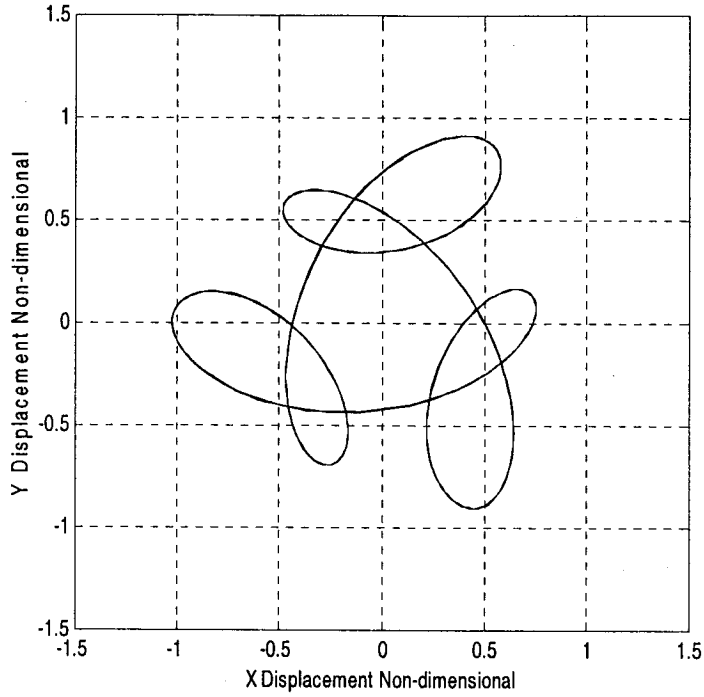

Figure 2.5.25: Orbit of Drill Central Line Motion for N=1100 rpm

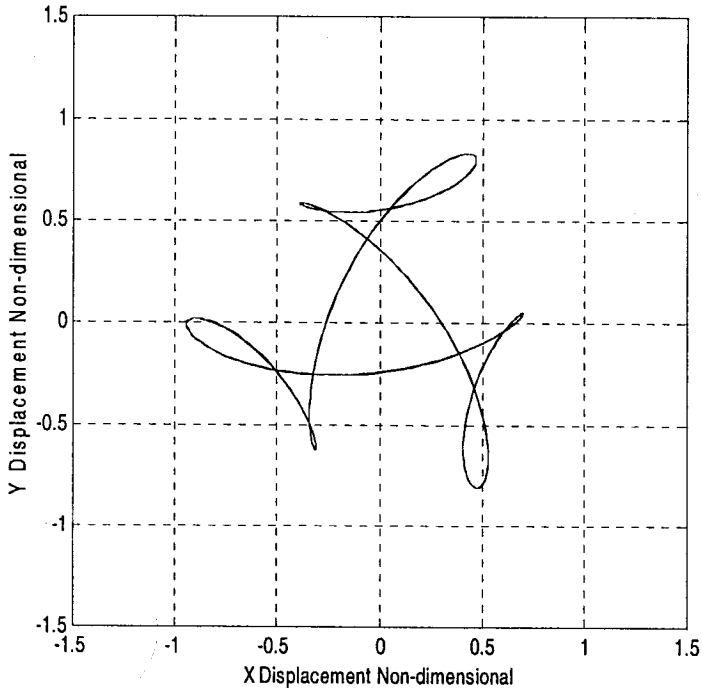

Figure 2.5.26: Orbit of Drill Central Line Motion for N=1200 rpm

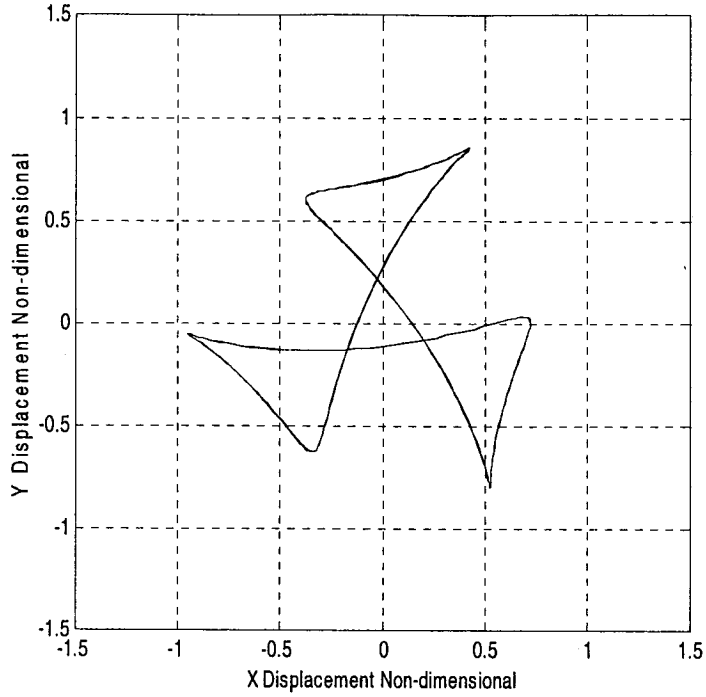

Figure 2.5.27: Orbit of Drill Central Line Motion for N=1300 rpm

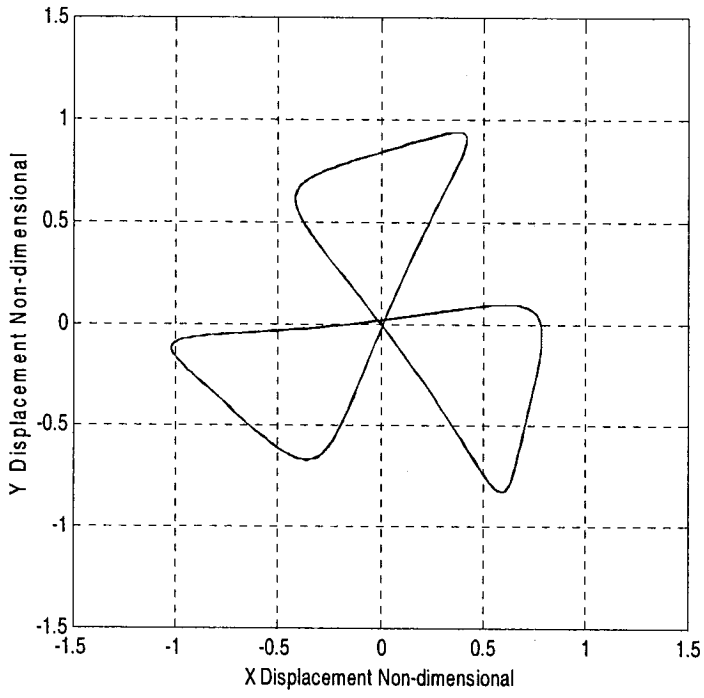

Figure 2.5.28: Orbit of Drill Central Line Motion for N=1400 rpm

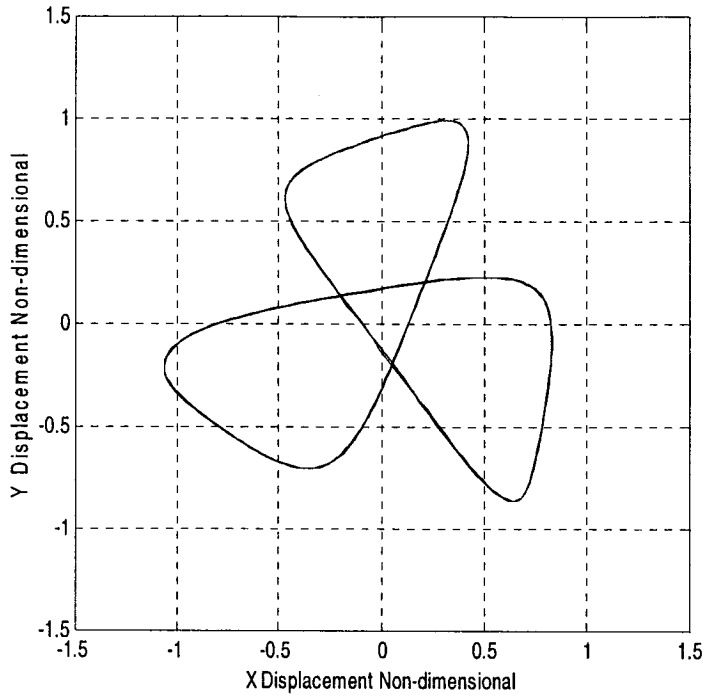

Figure 2.5.29: Orbit of Drill Central Line Motion for N=1500 rpm

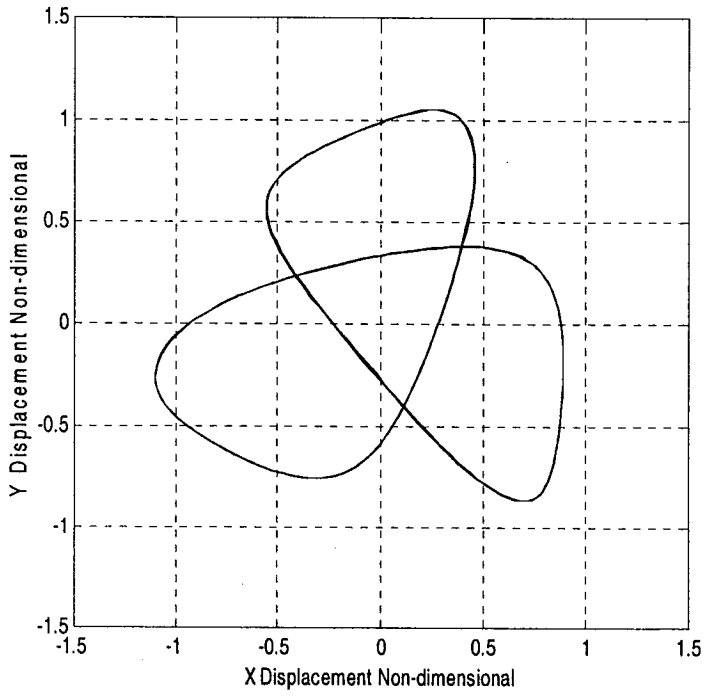

Figure 2.5.30: Orbit of Drill Central Line Motion for N=1600 rpm

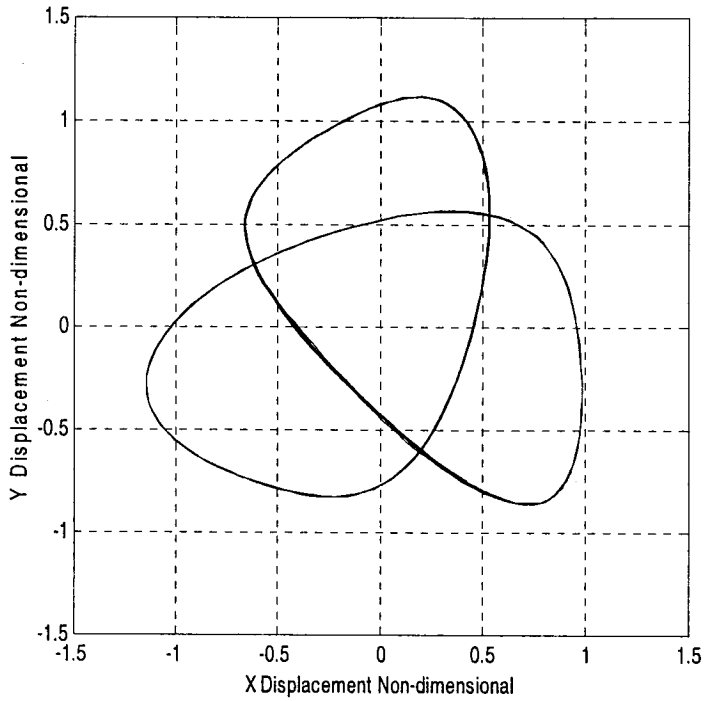

Figure 2.5.31: Orbit of Drill Central Line Motion for N=1700 rpm

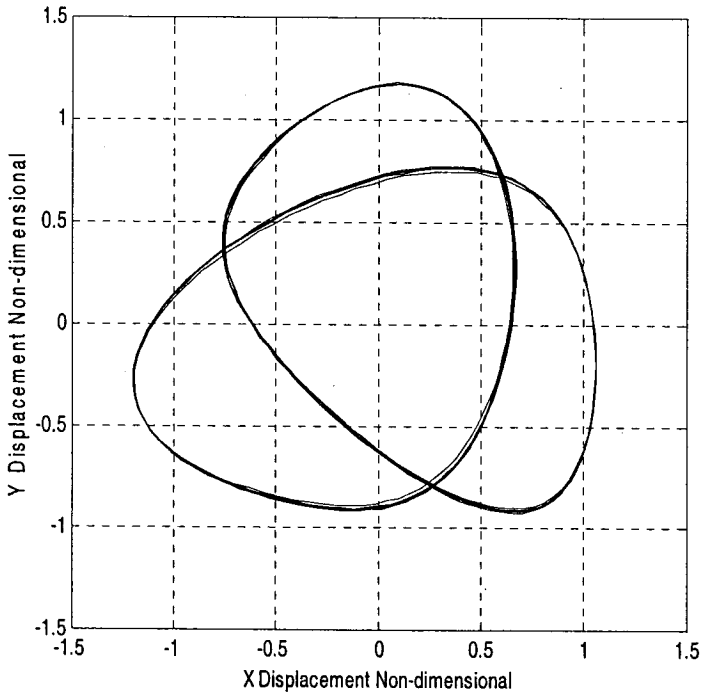

Figure2.5.32: Orbit of Drill Central Line Motion for N=1800 rpm

2.5.4 Drill Central Line Motion (Varying Force Imbalance Ratio $\frac{F^*_{imb}}{k\delta}$)

For the figures from 2.5.32 to 2.5.46 the simulation parameters used are the damping ratio ξ of 0.07, coefficient of friction 0.25, forcing frequency N of 41.9 rad/sec (400 rpm) and stiffness ratio α of 4.57 and modulation factor λ of 1.3, F_{sx}, F_{sy}, F_{nx}, and F_{ny} = 0, and for various values of force imbalance ratio. The variation of radial imbalance force amplitude has significant affect on the amplitude of the orbit. A three lobed orbit is observed and as the imbalance force amplitude increases, the sides of the lobes get distorted due to the hitting of the side wall of the hole which brings a sudden instability in the twist drill. For all the above cases a radial clearance gap δ of 0.038 mm, and measured natural frequency [28] of 507.1 rad/sec (80.7 Hz) is considered.

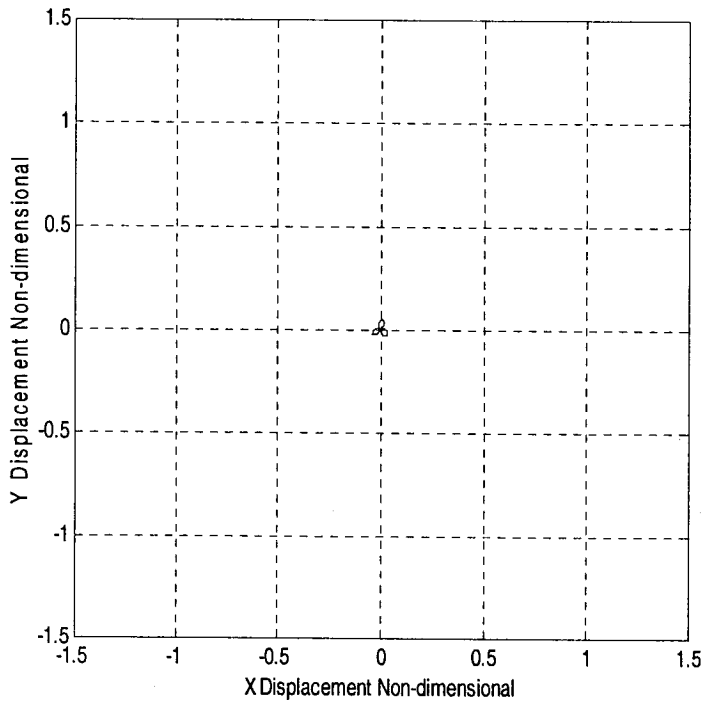

Figure 2.5.33: Orbit of Drill Central Line for $\frac{F^*_{imb}}{k\delta}$ = 0.01

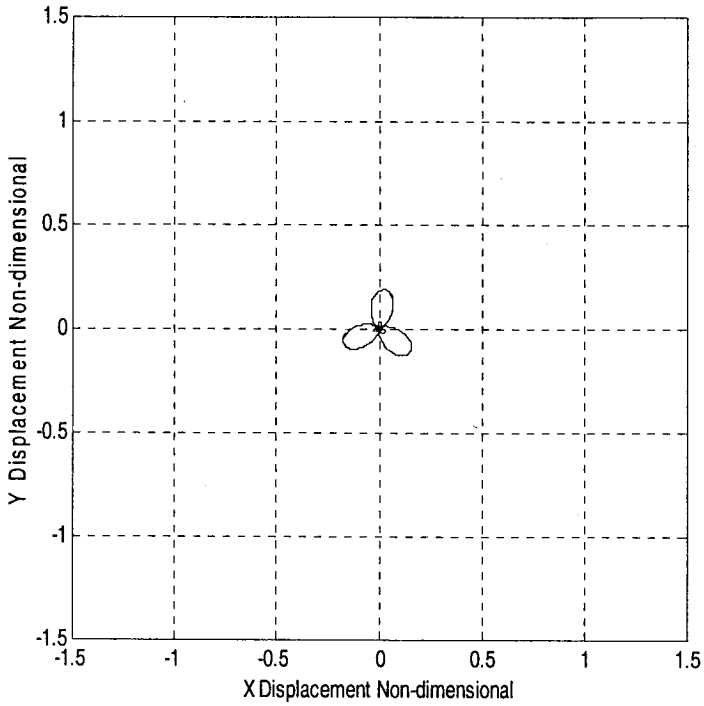

Figure 2.5.34: Orbit of Drill Central Line for $\frac{F^*_{imb}}{k\delta} = 0.04$

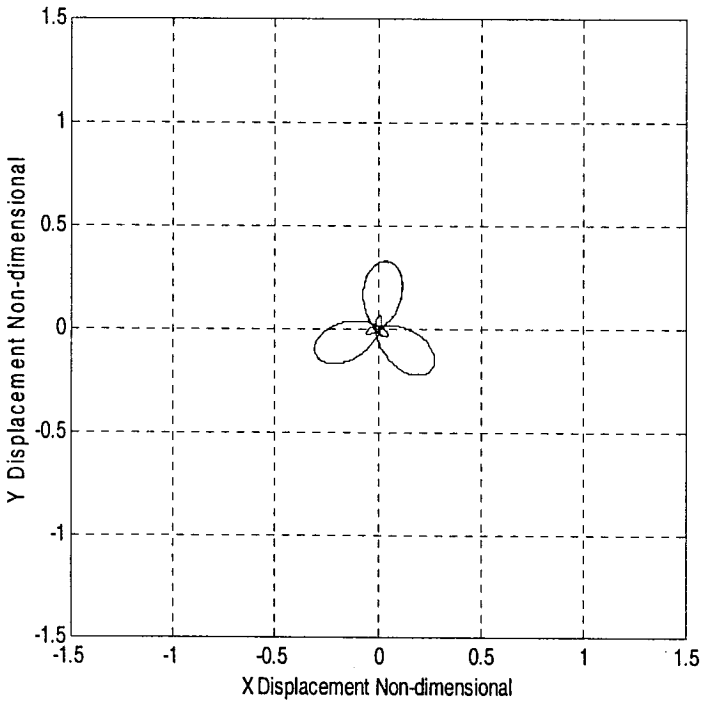

Figure 2.5.35: Orbit of Drill Central Line for $\frac{F^*_{imb}}{k\delta} = 0.07$

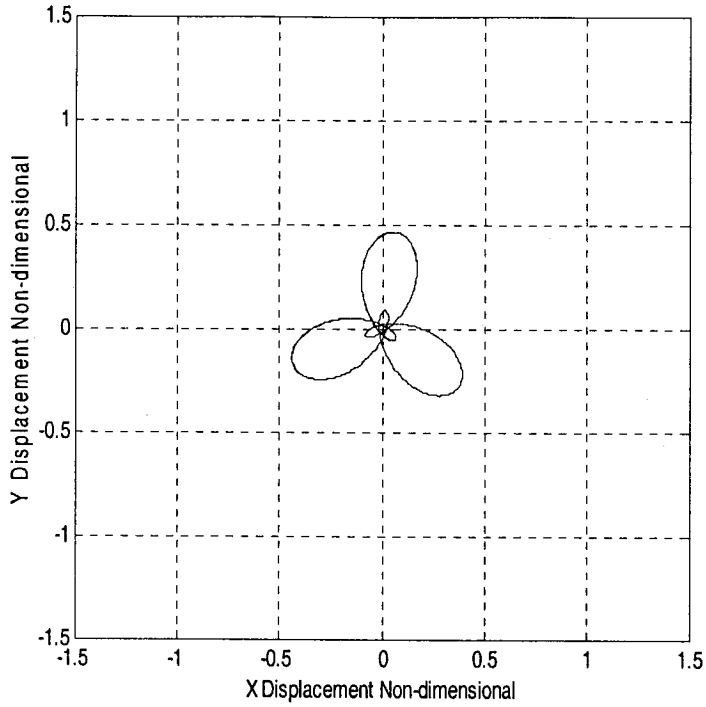

Figure 2.5.36: Orbit of Drill Central Line for $\frac{F^*_{imb}}{k\delta} = 0.1$

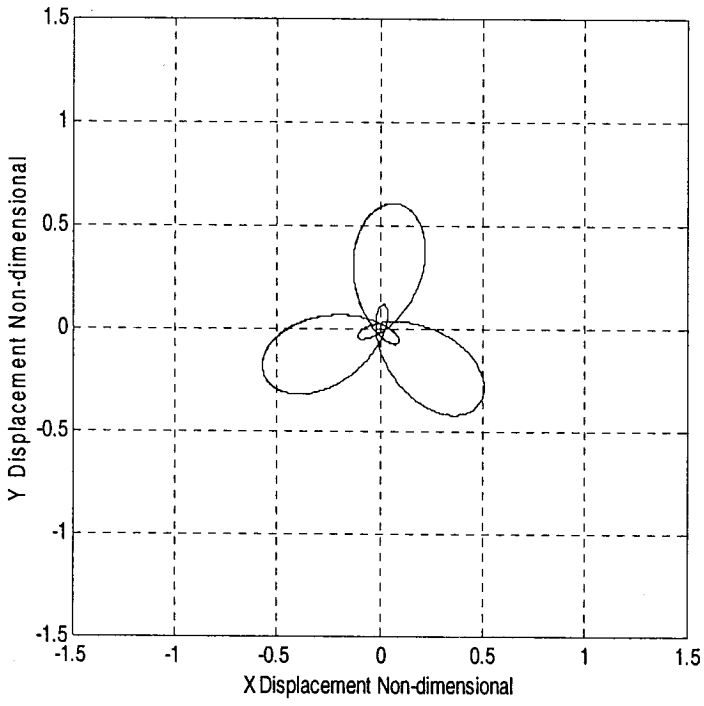

Figure 2.5.37: Orbit of Drill Central Line for $\frac{F^*_{imb}}{k\delta} = 0.13$

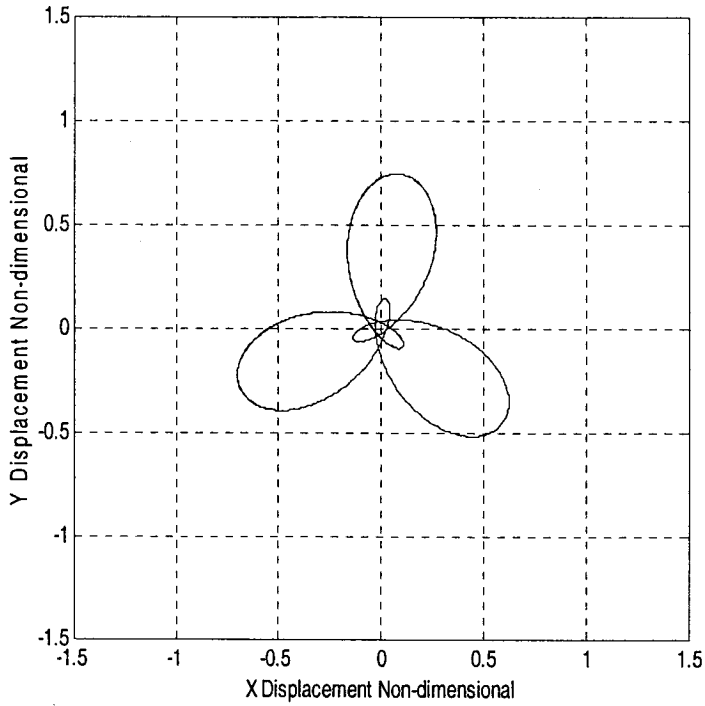

Figure 2.5.318: Orbit of Drill Central Line for $\frac{F^*_{imb}}{k\delta} = 0.16$

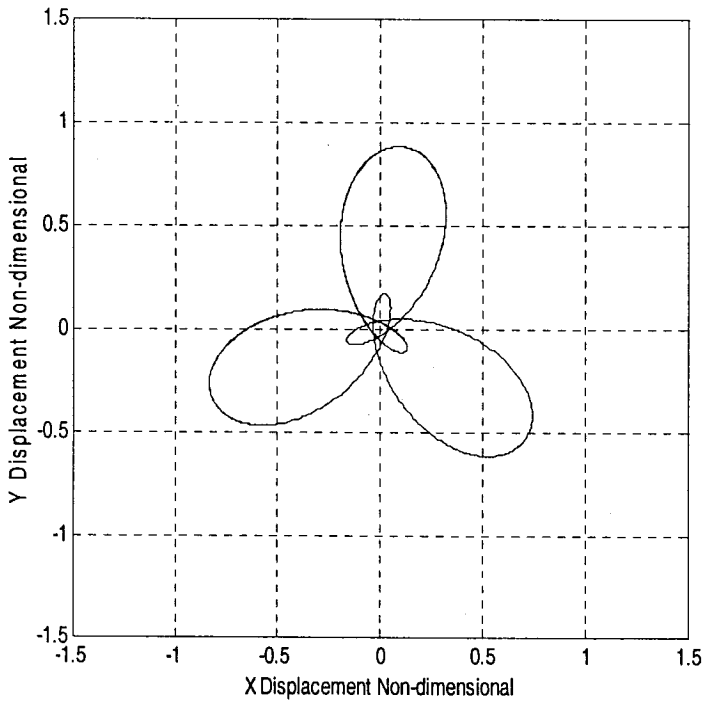

Figure 2.5.39: Orbit of Drill Central Line for $\frac{F^*_{imb}}{k\delta} = 0.19$

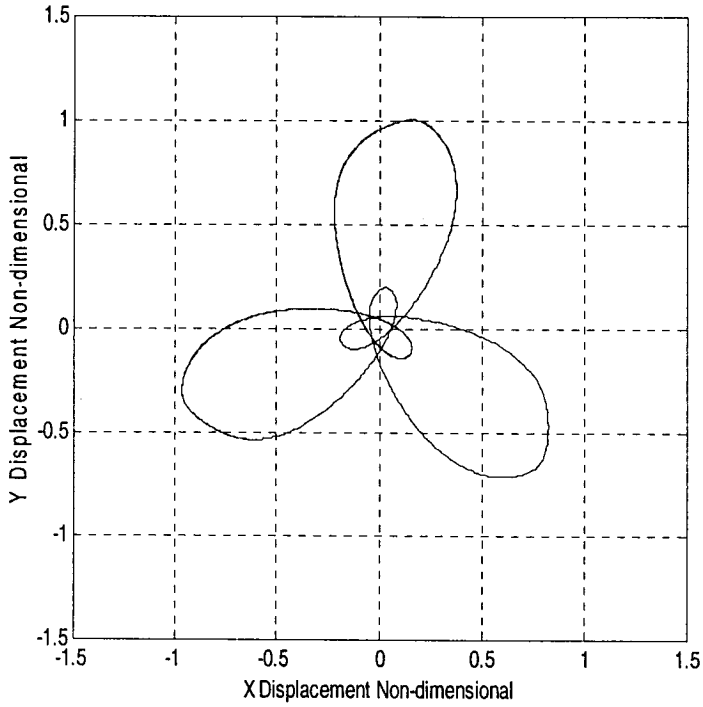

Figure 2.5.40: Orbit of Drill Central Line for $\frac{F^*_{imb}}{k\delta} = 0.22$

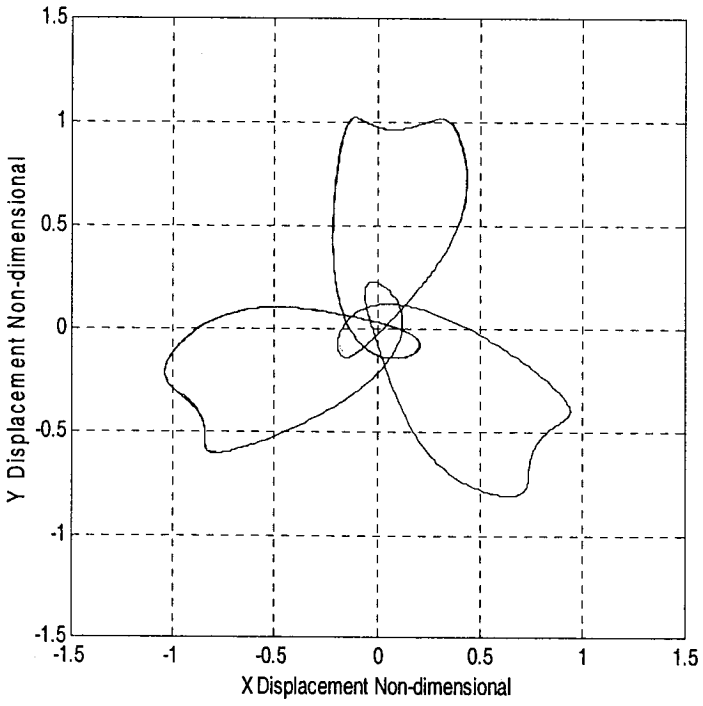

Figure 2.5.41: Orbit of Drill Central Line for $\frac{F^*_{imb}}{k\delta} = 0.25$

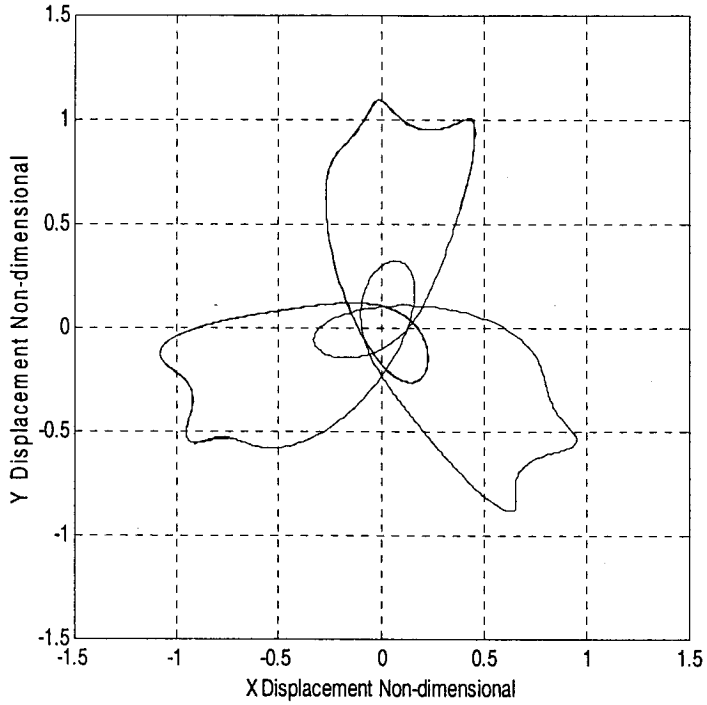

Figure 2.5.42: Orbit of Drill Central Line for $\frac{F^*_{imb}}{k\delta} = 0.28$

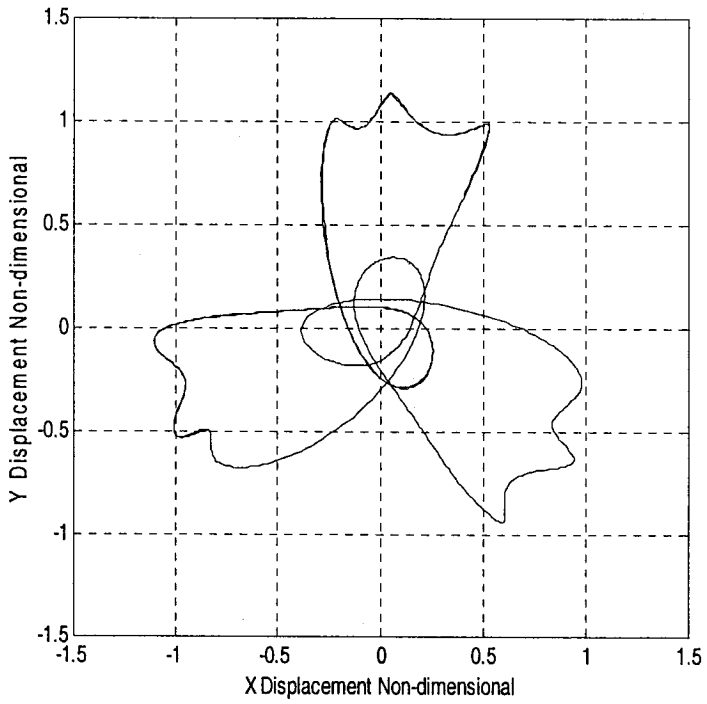

Figure 2.5.43: Orbit of Drill Central Line for $\frac{F^*_{imb}}{k\delta} = 0.31$

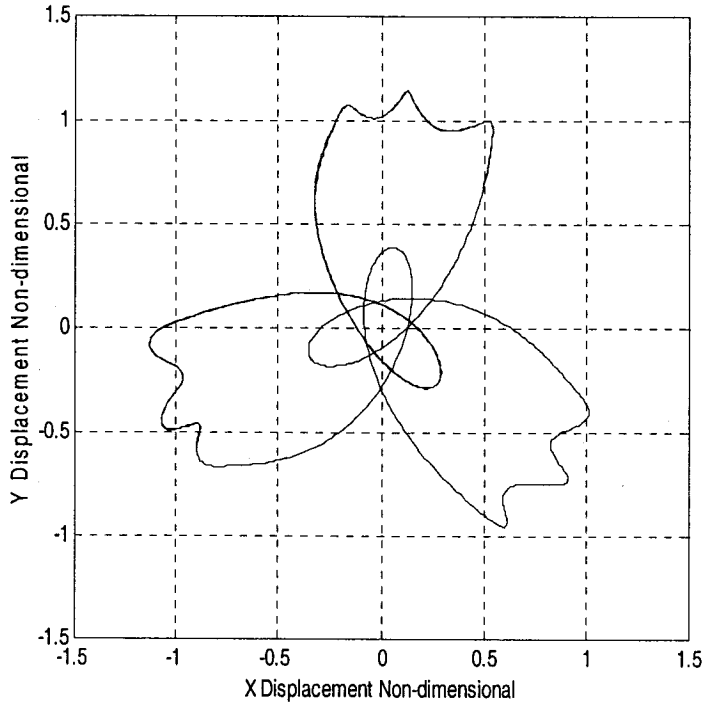

Figure 2.5.44: Orbit of Drill Central Line for $\frac{F^*_{imb}}{k\delta} = 0.34$

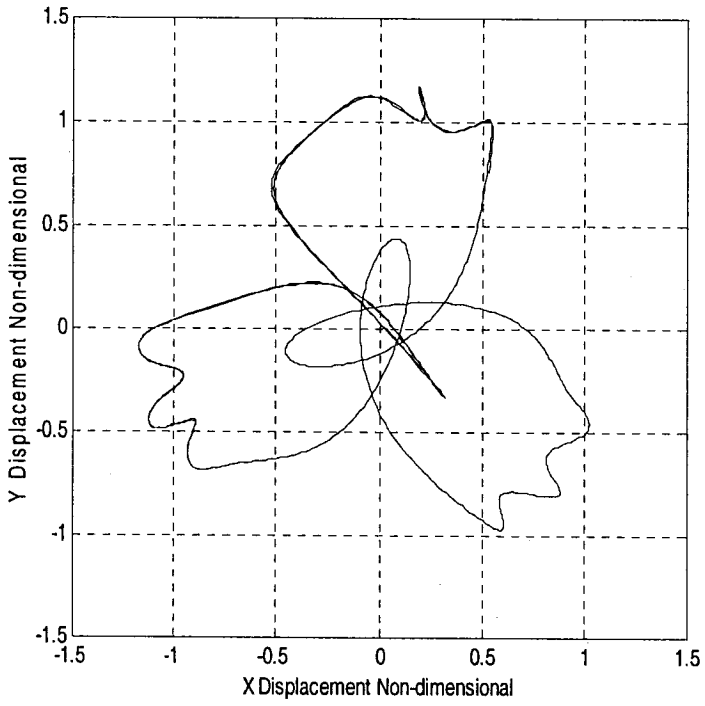

Figure 2.5.45: Orbit of Drill Central Line for $\frac{F^*_{imb}}{k\delta} = 0.37$

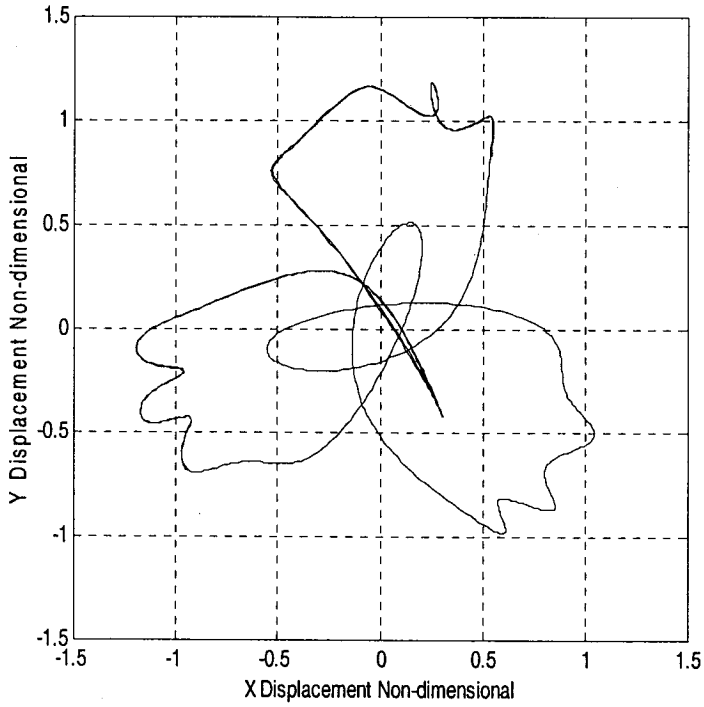

Figure 2.5.46: Orbit of Drill Central Line for $\frac{F^*_{imb}}{k\delta}$=0.4

2.6 Summary

In the present Chapter a two-dimensional model for drill bit transverse motion has been presented in the non-dimensional form. Simulation results were also presented in order to study the effect of various parameters on the transverse motion of twist drill. In the next chapter, details of the experiments performed to study the effect of drilling machine components on the transverse motion of the drill are presented.

CHAPTER 3

EXPERIMENTAL INVESTIGATION

In the previous Chapter, a discrete mathematical model for the drill-workpiece system was derived incorporating the imbalance of cutting forces acting on the cutting edge of the twist drill. This model is simplistic and treats the drill which is strictly a continuous system on a discrete system. Moreover, the drill is treated as fully clamped at the spindle, while in practice the spindle which is supported on bearings is a flexible system. In order to study the dynamic behavior of the drill-spindle-drive system more realistically, it is essential to measure such dynamic responses in an actual system.

In this Chapter, the drill press is analyzed for the factors responsible for the orbital motions of the twist drill. Modal testing experiment is done to determine the bending fundamental frequency of the machine-tool structure. Five experiments were carried out with two different diameters of drill bit.

None of the previous studies concerning the study of structural dynamics considered the vibrations of the spindle and tool as a whole. In reality the machine tool mechanical structure is an assembly of several mechanical modules, including the spindle unit, tool holder and the drive system that actuate them. The dynamics of these components are a reality. Non-contacting type proximity pickups were used to measure the orbital motion of the twist drill near the drill tip; accelerometers were used to measure the vibrations

near the spindle. An electronic package with lab view software was used to obtain the data.

3.1 Experimental Set-up, Description and Instruments

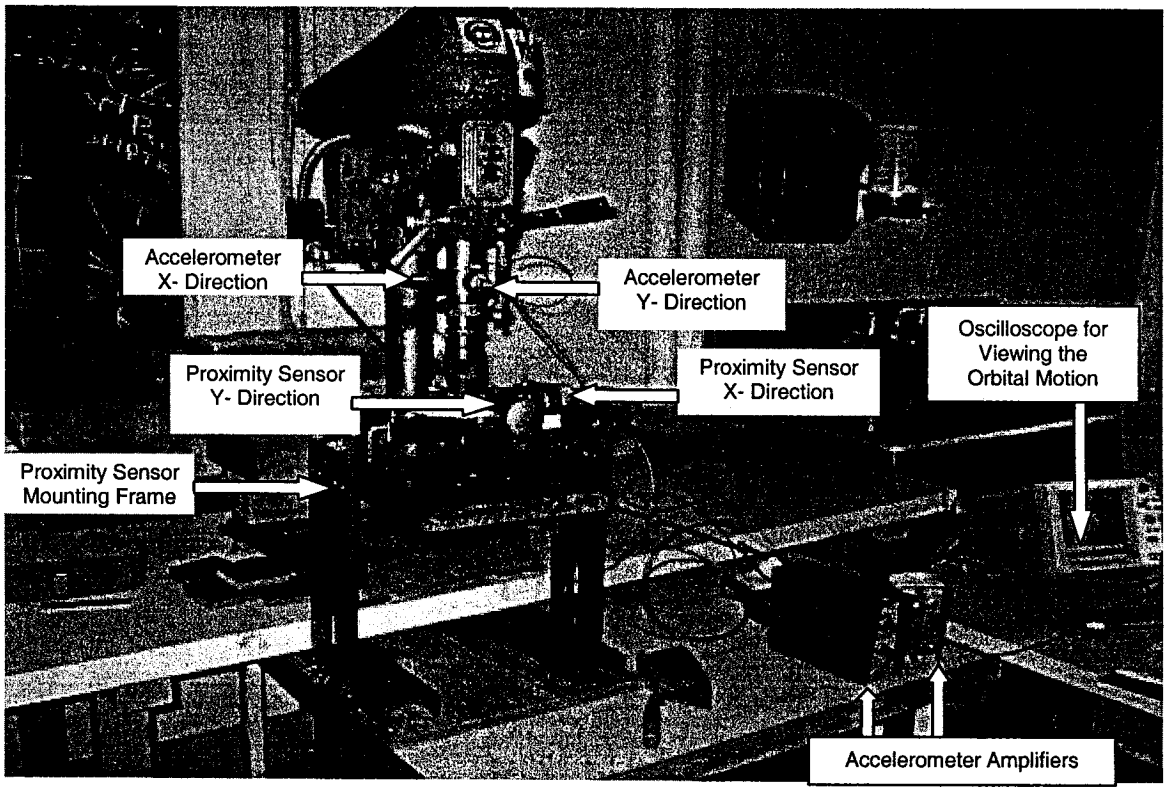

Figure 3.1: Experimental Set-up

3.1.1 Non-contacting Displacement Transducers

The transverse motion of the drill (displacement along X and Y directions, Z being the axis of rotation of the drill) are measured using proximity pickups or the non-contacting displacement transducers. The eddy current developed due to the rotation of the drill bit relative to the sensors, modulates the oscillator voltage signal which is demodulated to provide an output signal proportional to the displacement. This displacement signal can

be recorded and analyzed. The output of this transducer is a time varying continuous voltage analogous to the quantity being measured and a scale factor or a calibration constant determines the value of the measured quantity.

In order to make the precision non-contact displacement measurements in the experiment, Kaman Instrumentation Displacement Measuring System Model KD-2310 is used. The system includes a sensor, a 3 m coaxial cable and a signal conditioning electronics package. The principle of impedance variation caused by eddy currents induced in a conductive metal target is used in the system. The coupling between the sensor and the target is dependent upon their displacement or the gap between them. The output voltage of the system is proportional to the distance between the face of the sensor and the metallic target. KD-2310 systems are most stable when the target is near the face of the sensor. Also, the sensitivity to the cable movement, dielectric constant, magnetic field, etc., is the greatest when the target is at full-scale displacement.

3.1.2 Accelerometers

The accelerometers are used to measure the transverse motion of the spindle (acceleration along X and Y directions). Kistler 4382 type uni-axial piezoelectric type accelerometers were mounted on the spindle as shown in the figure 3.1 one in each direction (X and Y), which measures the accelerations.

3.1.3 Data Acquisition System (DAQ)

The specifications of the DAQ card used in the experiment are given in Appendix. The devices can scan multiple channels at the same maximum rate as their single-channel rate. In this experiment four channels at the scan rate of 256 scans per second for each channel were used

3.2 Proximity Pickups Mounting, Installation and Calibration

Two proximity probes were mounted as shown in the figure 3.1 on a sensor mounting frame that is fabricated to measure the response amplitude in both X and Y directions near the drill tip (target surface). Every care has been taken to isolate the mounting frame from the machine bed to prevent the vibrations coming out from it there-by isolating the sensor frame. The twist drill cutter consists of helical flutes, since the periphery of the drill is not a smooth surface; this mechanical run-out is added to the vibration signal detected by the proximity probe. The periphery of the rotating drill presents a target that moves laterally across the proximity probe's magnetic field as a consequence, the system's output reflects not only the drill vibration and the mechanical run-out, but also the superimposed effects of circumferential variations in the drill surface conditions as well as electrical conductivity and permeability variations just below the drill surface. In order to provide a smooth surface to the drill a cylindrical shell of one inch height and internal diameter of the shell equal to the diameter of the drill is glued on to the helical surface at a distance of one inch from the cutting edge as shown in the figure 3.2. The mass of the cylindrical shell is very much less compared to the mass of the drill. Hence, any effect of mass unbalance coming out due to this can be neglected. Now the proximity

pickups are installed near to this smooth targeted surface in X and Y directions, respectively.

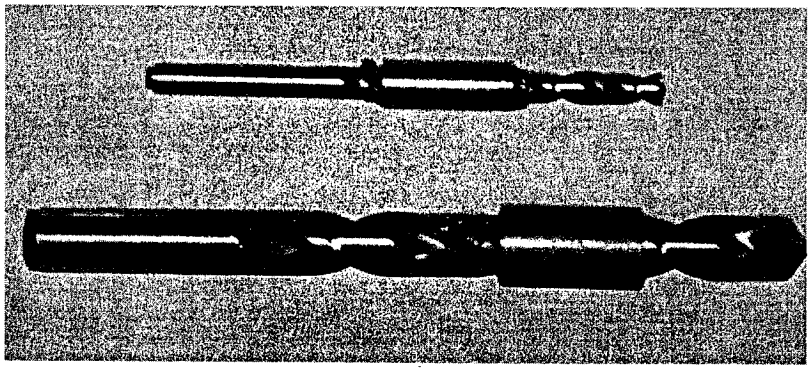

Figure 3.2: Twist Drills

Once the proximity pickups are installed they are calibrated for the operation. The High Accuracy Band calibration procedure (Kaman Instrumentation manual) was carried out.

The calibration procedures are as follows:

1. Install the sensor in the calibration or application fixture, ensuring that when the target is at its closet point to the sensor there is a gap (off set). With curved targets, decreasing offset will improve linearity. Never allow the target to strike the sensor.

2. Define the reduced measurement span one will use.

3. Position the target so that it is at the end of the desired span, plus offset. Adjust the linearity control until the output reads the desired maximum voltage.

4. Position the target at the beginning of the defined span (plus offset) and adjust the zero control to read the desired voltage at that point. The desired voltage does not have to be zero.

5. Position the target at the mid-point between the end points of the desired span.

6. Reposition the target so that it is at the far end of the span relative to the sensor. Note the difference between the actual reading and the desired reading. Adjust the linearity control until the out put reads the desired voltage level, then continue past the desired reading by an amount equal to the first difference one noted. This technique is called 100% oversetting and is used to reduce the number of iterations needed to calibrate the system.

7. Repeat the steps 3 through 6 as many times as necessary until one reaches the desired output voltage at each point. No further adjustment of the zero, gain and linearity controls

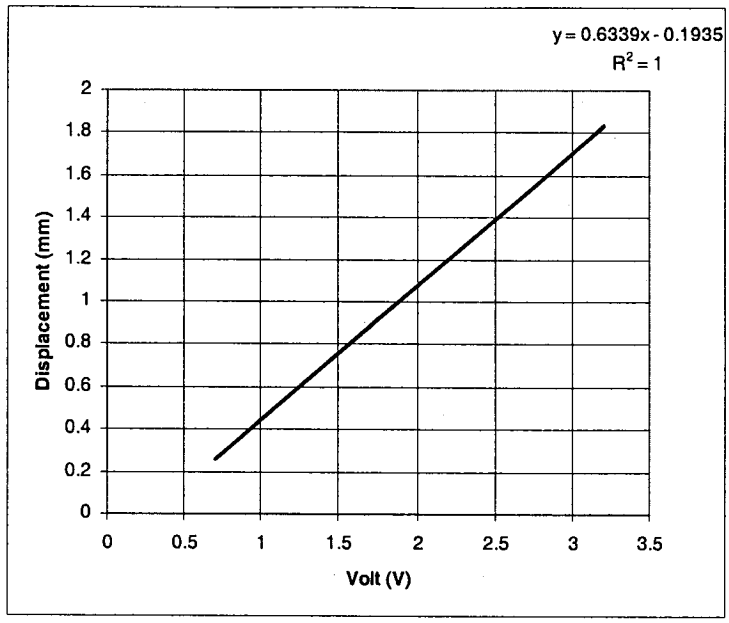

Figure 3.2.1: Calibration Curve for X-direction Sensor for 6.35 mm Diameter Drill

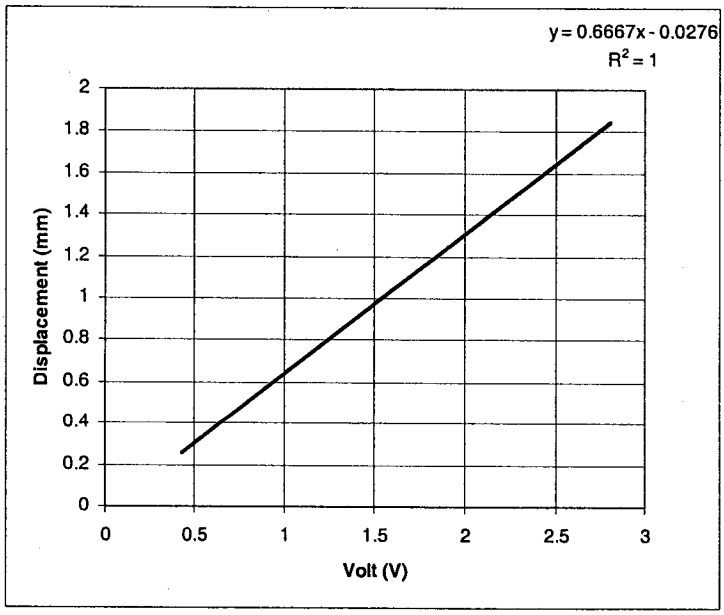

Figure 3.2.2: Calibration Curve for Y-direction Sensor for 6.35 mm Diameter Drill

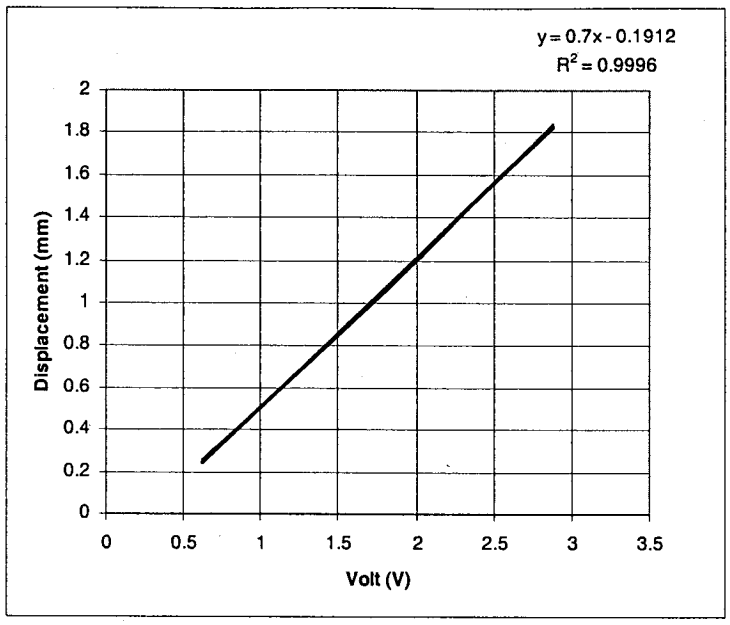

Figure 3.2.3: Calibration Curve for X-direction Sensor for 12.7 mm Diameter Drill

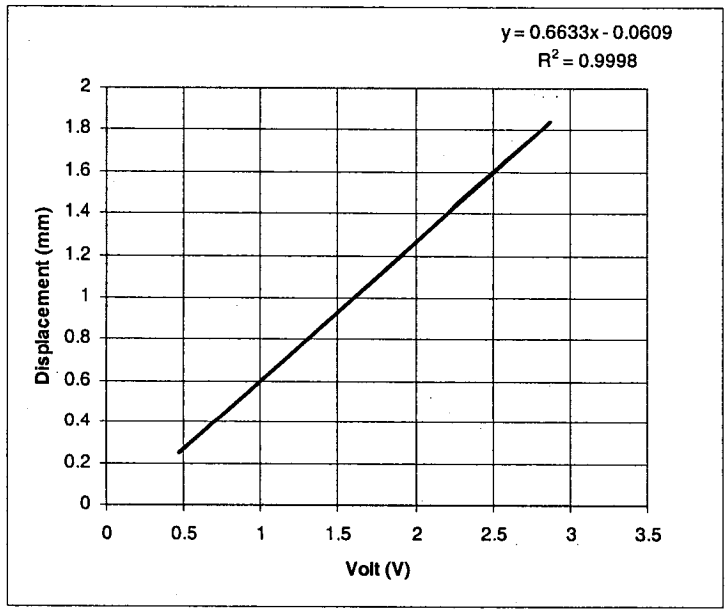

Figure 3.2.4: Calibration Curve for Y-direction Sensor for 12.7 mm Diameter Drill

will be needed when proper calibration is obtained. Figures 3.2.1 to 3.2.4 shows the calibration curves obtained.

3.3 Accelerometer Calibration

In most applications, it is important to know the exact accelerometer sensitivity at various frequencies of interest. This data can only be achieved through periodic calibration. The ratio of the output signal to the applied motion is the accelerometer's sensitivity. The sensitivity of an accelerometer is usually expressed in mV/g (voltage mode) or pC/g (charge mode) at a given frequency. Calibration of an accelerometer is to accurately determine the sensitivity at various frequencies throughout the frequency range of interest. The unknown accelerometer is attached to the back-to-back standard accelerometer and thus, both accelerometers experience the same motion. At each frequency of interest, the g-level is precisely set by measuring the output of the standard accelerometer. At the same time or alternately, the output of the unknown accelerometer is measured and sensitivity (mV/g or pC/g) versus frequency report is set.

In the present study the accelerometers are mounted on to a platform, a random excitation was given to the platform and the frequency report was set with respect to a reference accelerometer. The analyzer used for this purpose is Brunel-2035 type. The measured calibration factors for the accelerometers arranged in X and Y directions were 4.81 mV/m/sec^2 and 10.5 mV/m/ sec^2, respectively.

3.4 Modal Testing of Drill Machine Spindle-tool System

An experimental modal analysis for the total machine tool structure is performed; figure 3.4 represents a schematic for the experimental set-up. The drill tip is excited with a hammer in the x-direction and the resulting vibrations are measured with the proximity sensor arranged near the drill tip. In order to verify that the results are reliable, the same experiment is repeated many times to ensure good repeatability. The vibration response is captured in the oscilloscope. A similar kind of experiment is repeated in y-direction and the measured fundamental bending natural frequency is found to be between 148-150 Hz in both directions.

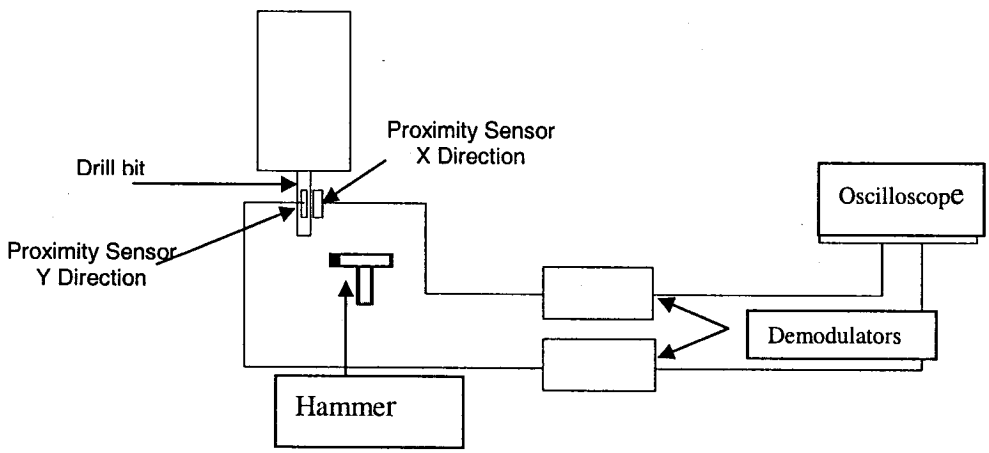

Figure 3.4: Schematic Sketch for Modal Analysis

3.5 Experimental Investigation

The following experiments were carried out:

Part-1: Tracing the free orbit of the spindle cutter (or spindle-tool) system by dismounting the belt drive from the driven pulley and rotating the driven pulley with hand by giving small increments in counter-clockwise direction.

Part-2: Tracing the free orbit of the spindle cutter (or spindle-tool) system by mounting the belt drive on to the driven pulley at low speed position (445 rpm) and rotating the driven pulley by hand in small increments by pulling the belt drive in counter-clockwise direction.

Part-3: Tracing the free orbit of the spindle cutter (or spindle-tool)system by mounting the belt drive on to the driven pulley at medium speed position (930 rpm) and rotating the driven pulley by hand in small increments by pulling the belt drive in counter-clockwise direction.

Part-4: Tracing the free orbit of the spindle cutter (or spindle-tool) system by mounting the belt drive on to the driven pulley at high speed position (1795 rpm) and rotating the driven pulley by hand in small increments by pulling the belt drive in counter-clockwise direction.

Part-5: Measurement of whirl orbits of the spindle cutter (or spindle-tool) system at speeds of rotations of 445 rpm, 930 rpm, and 1795 rpm.

The experiments were performed at no load conditions, owing to the reason that the drill press possesses only manual feed. Since maintaining a constant feed rate through out the cutting process is not possible, the experiments were confined only to no cutting

conditions. The signals sensed by the proximity sensors and accelerometers are routed into the data acquisition system package, which consists of demodulators, data acquisition card and a computer with lab view software to capture the signals and analyze them.

3.6 Signal Processing

Raw vibration signals always are invariably contaminated with noise which may partially obscure the desired components. Thus, the most frequent signal conditioning operation is filtering. Analog to Digital signal conversion is often the first step in data acquisition, with filtering performed computationally from the digitized signal. However, low-pass analog filter should be inserted ahead of the analog to digital converter to avoid aliasing, which is the reflection into lower end of the spectrum of high-frequency content above sampling-rate capability of the analog to digital converter.

In the present study, signal conditioning operations which include integration of raw acceleration signals obtained from accelerometer is done in order to extract the displacements near the spindle. Integrating accelerometer time histories without proper filtering will produce drift in the calculated velocities and displacements. Displacements tend to be dominated by low frequencies, but the accelerometers used in this study, like most piezoelectric accelerometers, are not capable of recording very low frequencies. Maximizing the useful amount of low frequency data from the acceleration records is somewhat subjective, requiring careful consideration of signal processing techniques, the instrumentation characteristics, the signal conditioning and data acquisition systems, and the characteristics of the physical system being studied.

The noise characteristics are generally similar in all acceleration-time histories because they all come from the same accelerometer type and pass through the same electronic components before being recorded. A band pass filter is designed to remove the signal content outside a designated frequency band and thus is a low-pass filter in series with a high-pass cut-off frequency. Again, if filtering digitally, the original analog signal has been first passed through an appropriate analog low-pass filter to avoid aliasing. A band pass filter centered at rotor speed is a standard operation in rotor balancing, since only the synchronous vibration component is processed for rotor balancing purposes. The fundamental basis for this is that balancing procedures are inherently based on the tacit assumption that the vibratory system is linear, and thus only the forcing frequency (once-per-rev) vibration amplitude and phase angle are accommodated in rotor balancing procedures. Synchronous band pass filtering thus improves balancing accuracy. Butterworth band pass filter is used in the present study for filtering the acceleration signal acquired. The filtered acceleration signals are then numerically integrated to obtain the displacement signals.

3.7 Experimental Results

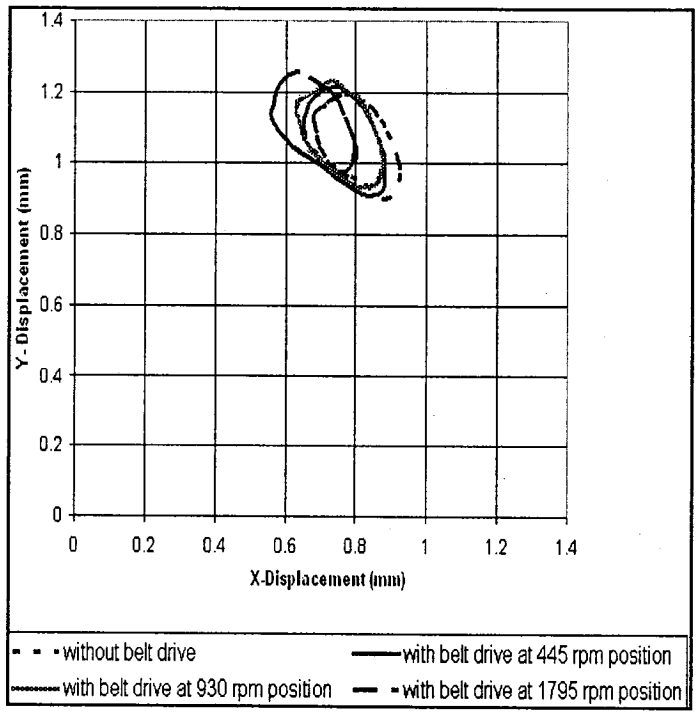

Figure 3.7.1: Comparison of Orbits in Trial-1 for 6.35 mm Diameter Drill

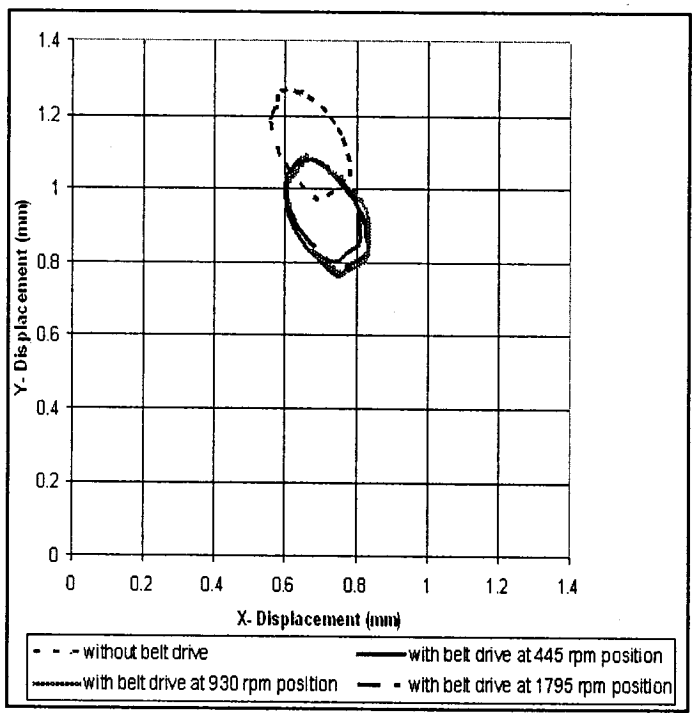

Figure 3.7.2: Comparison of Orbits in Trial-2 for 6.35 mm Diameter Drill

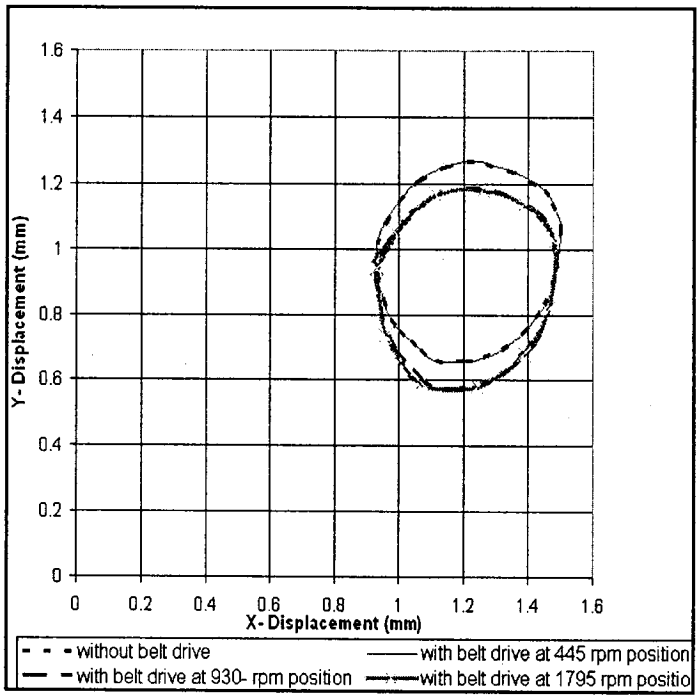

Figure 3.7.3: Comparison of Orbits in Trial-1 for 12.7 mm Diameter Drill

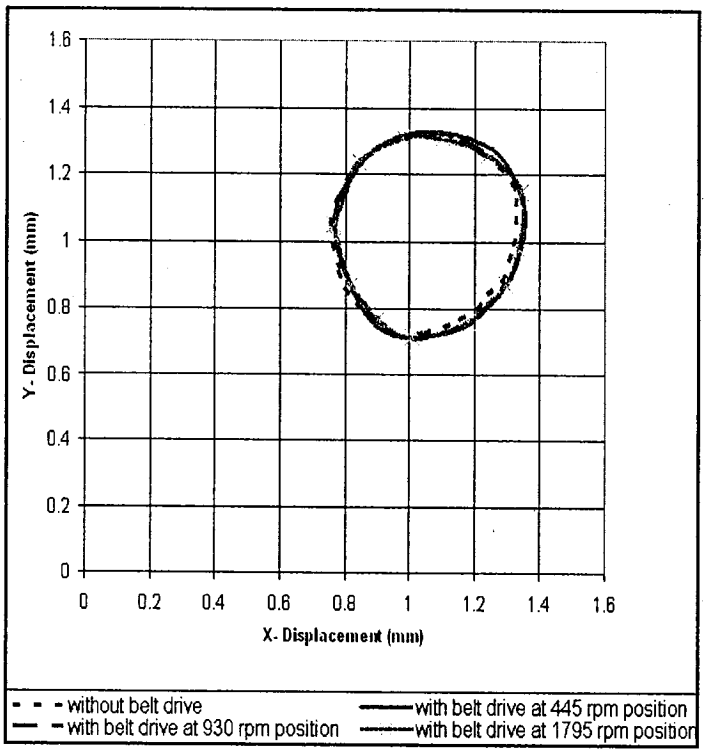

Figure 3.7.4: Comparison of Orbits in Trial-2 for 12.7 mm Diameter Drill

Figures 3.7.1 and 3.7.2 shows two trials for the comparison of free orbits traced for Part-1, Part-2, Part-3 and Part-4 respectively (as explained in Chapter 3, 3.5 Experimental Investigation), for the spindle drill system of 6.35 mm drill diameter near the drill tip. In the first trial, figure 3.7.1, the traced orbits showed a similar kind of pattern for all the four parts. In the second trial, figure 3.7.2, the drill bit angular orientation in the tool holder is rotated approximately to 90°, but the length of shank portion inserted into the chuck is different when compared with the trial one and the orbits traced again were found to be same for the four parts.

A similar experiment was repeated for the case of 12.7 mm diameter drill with two trials and the shape of the orbits traced were found to be same for all the four parts as shown in the figures 3.7.3 and 3.7.4, respectively. One can observe the shift in the orbits traced in the figures 3.7.1 to 3.7.4 which may be due to bow in the spindle. The present investigation gives an insight into the relative spindle run-out. The relative spindle run-out for the case of 6.35 mm diameter drill is found to be approximately 0.2 mm and for the case of 12.7 mm diameter drill is found to be approximately 0.6 mm.

3.7a Results for Drill (6.35 mm Diameter)

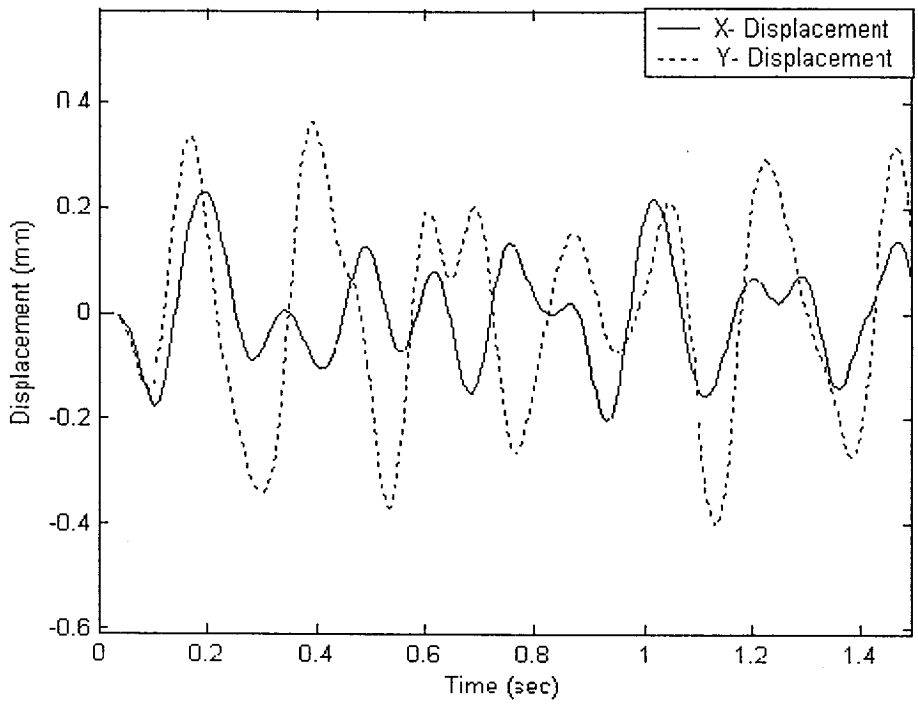

Figure 3.7.5: Time-displacement Response of Spindle at 445 rpm

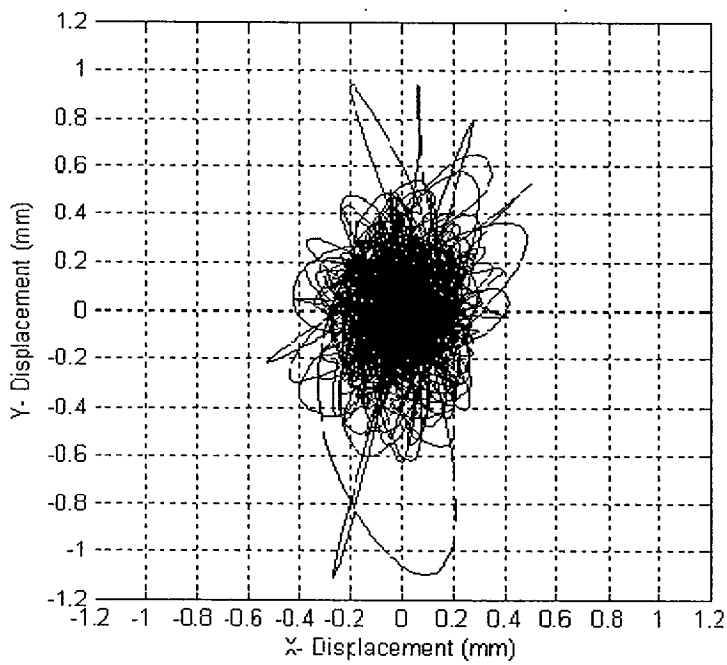

Figure 3.7.6: Whirl Orbit of Spindle at 445 rpm

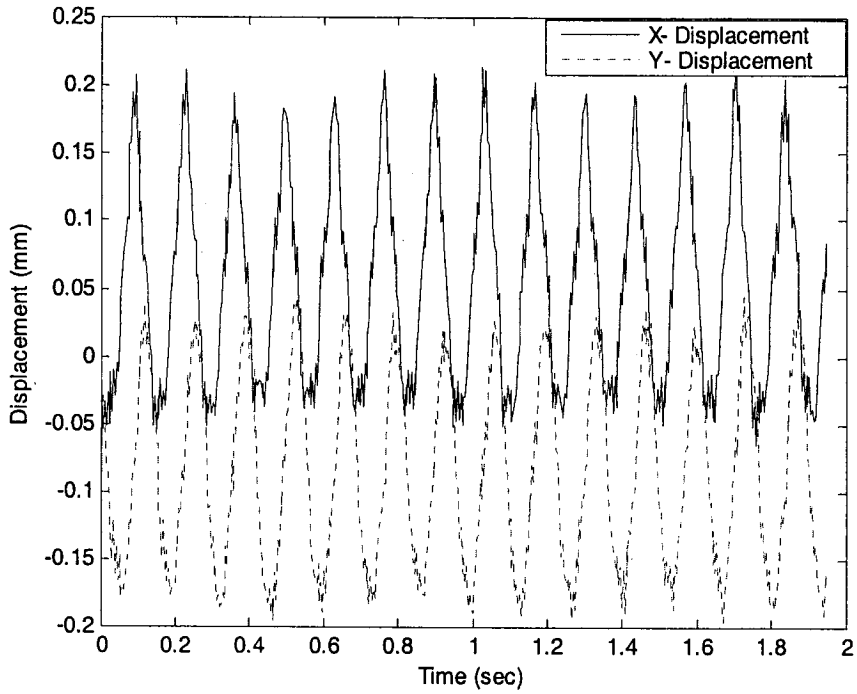

Figure 3.7.7: Time-displacement Response near Drill Tip at 445 rpm

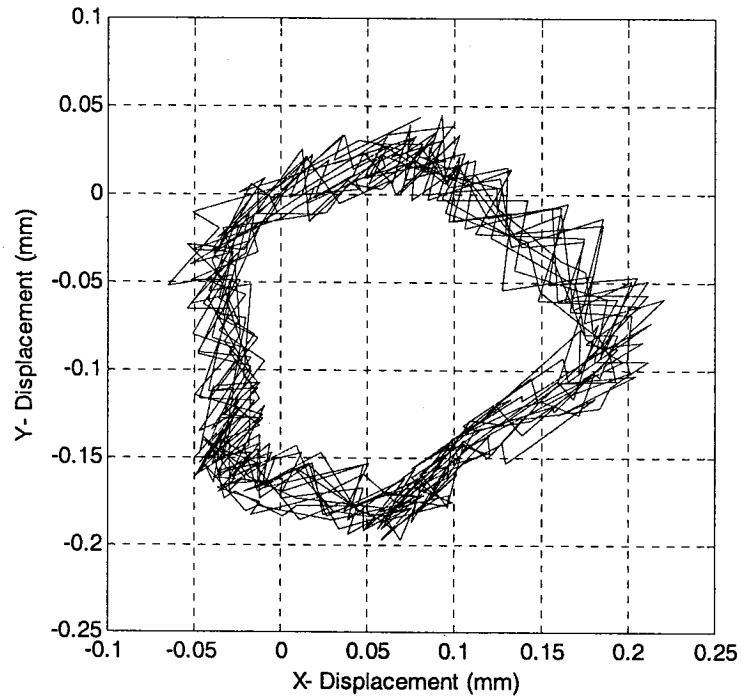

Figure 3.7.8: Whirl Orbit near Drill Tip at 445 rpm

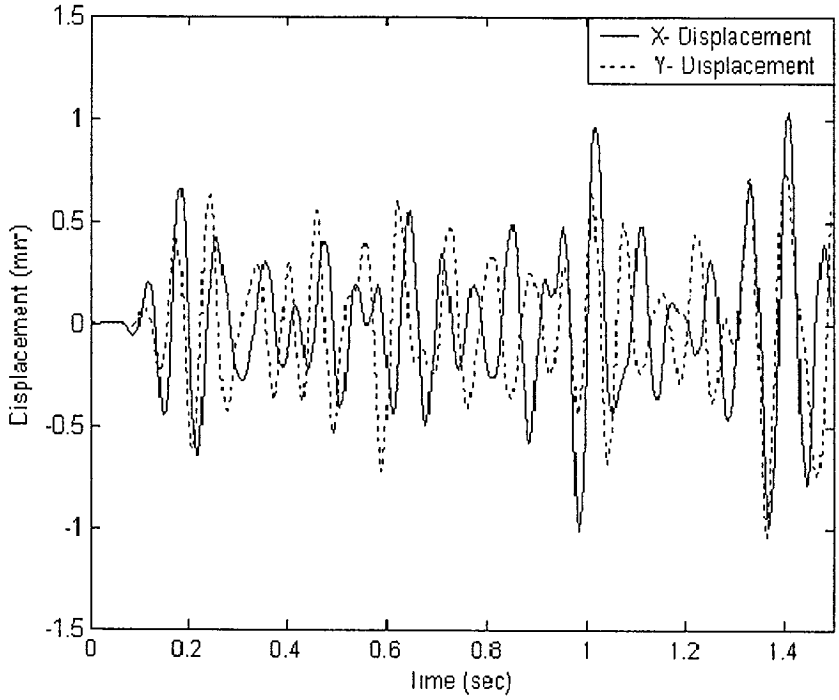

Figure 3.7.9: Time-displacement Response of Spindle at 930 rpm

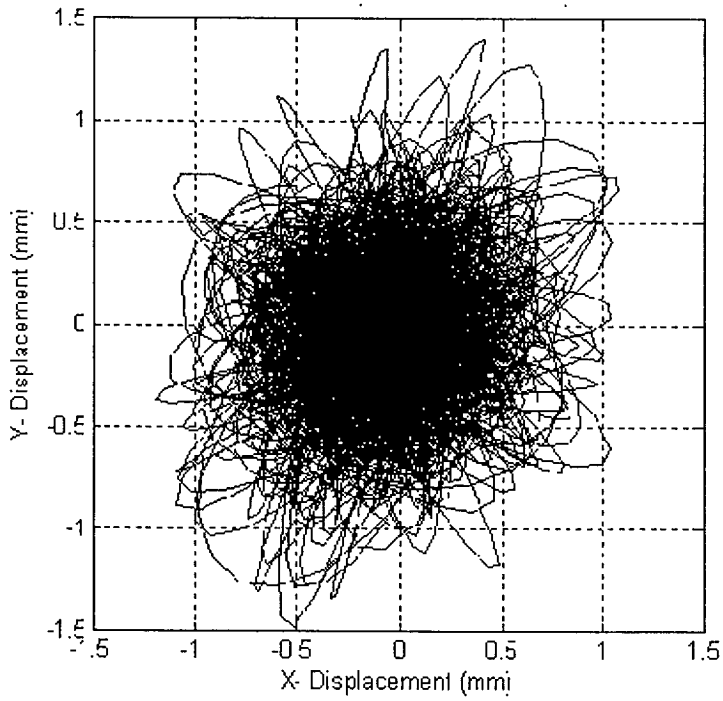

Figure 3.7.10: Whirl Orbit of Spindle at 930 rpm

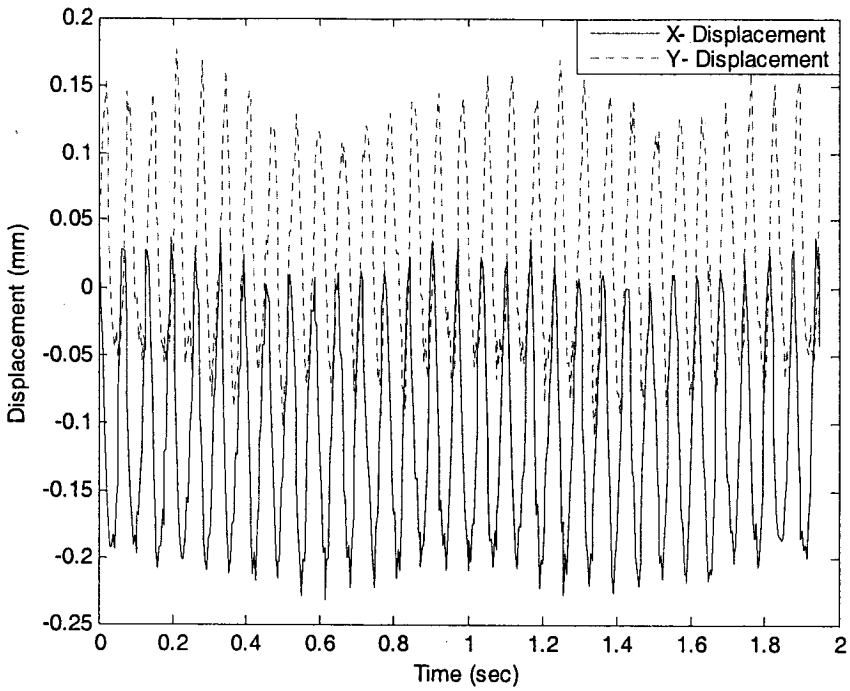

Figure 3.7.11: Time-displacement Response near Drill Tip at 930 rpm

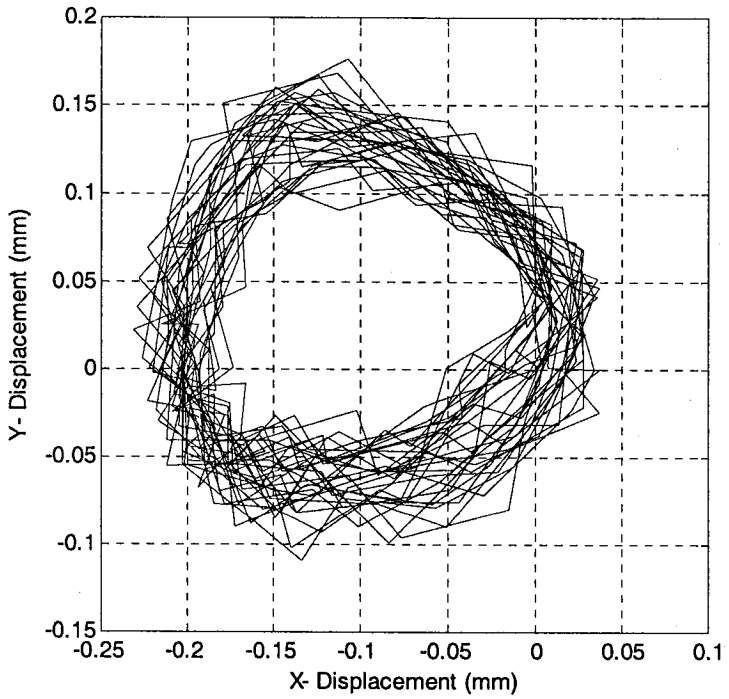

Figure 3.7.12 Whirl Orbit near Drill at 930 rpm

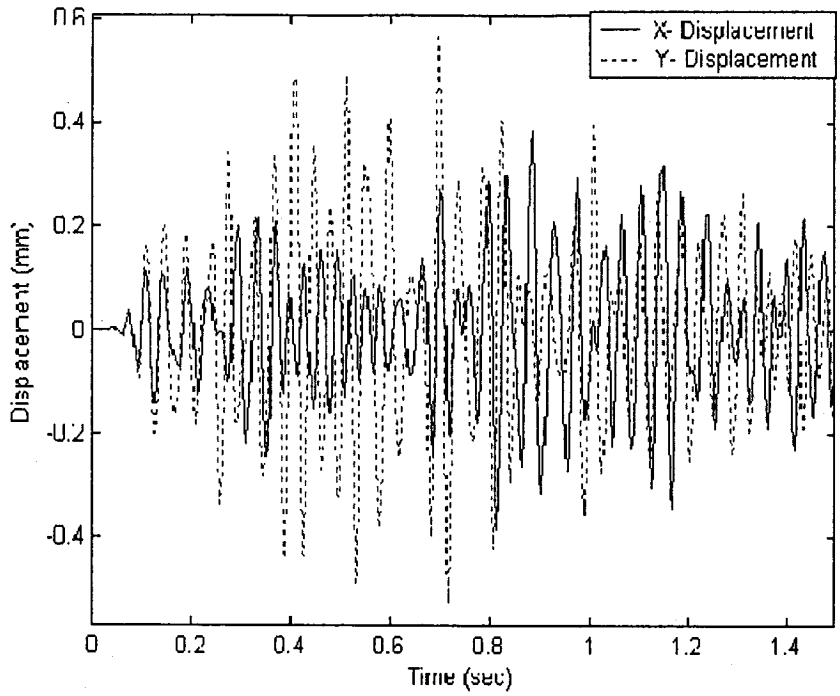

Figure 3.7.13: Time-displacement Response of Spindle at 1795 rpm

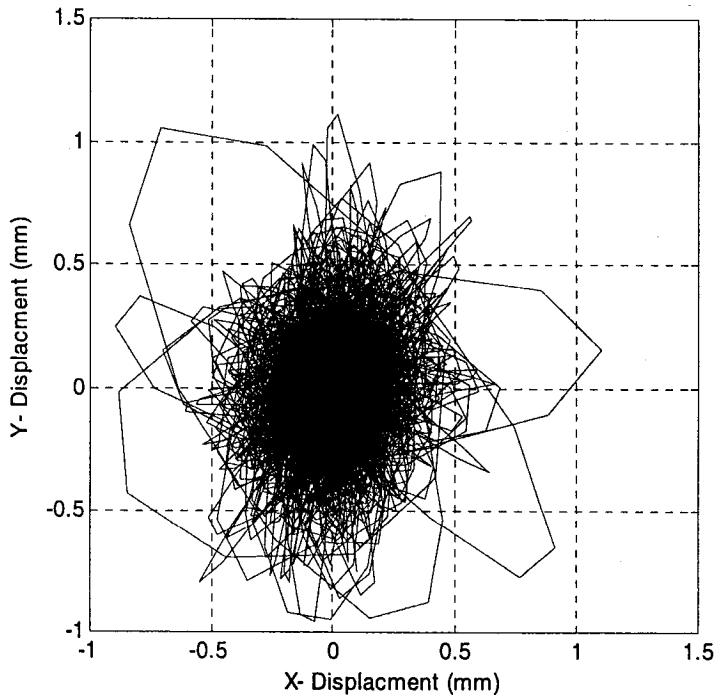

Figure 3.7.14: Whirl Orbit of Spindle at 1795 rpm

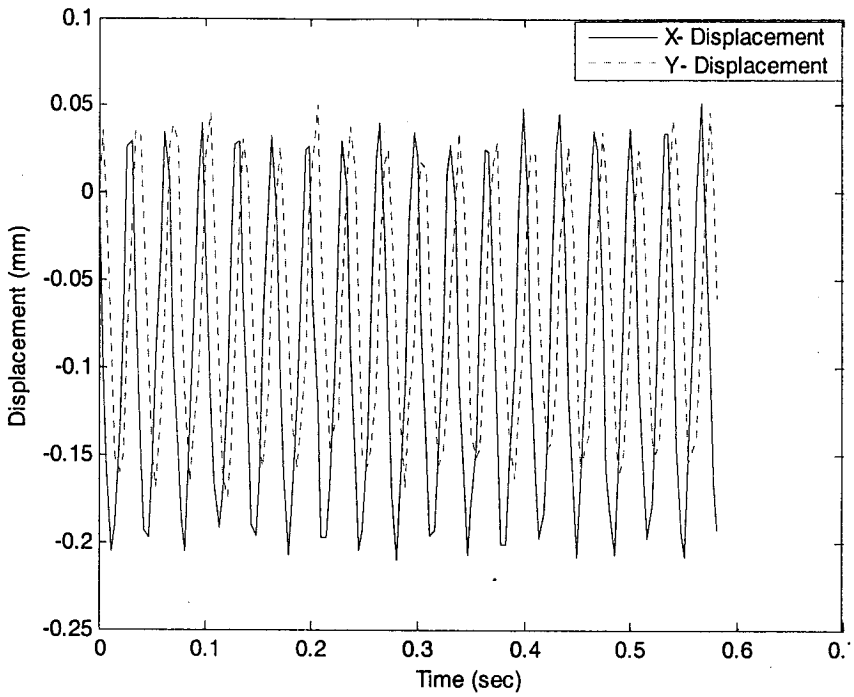

Figure 3.7.15: Time-displacement Response near Drill Tip at 1795 rpm

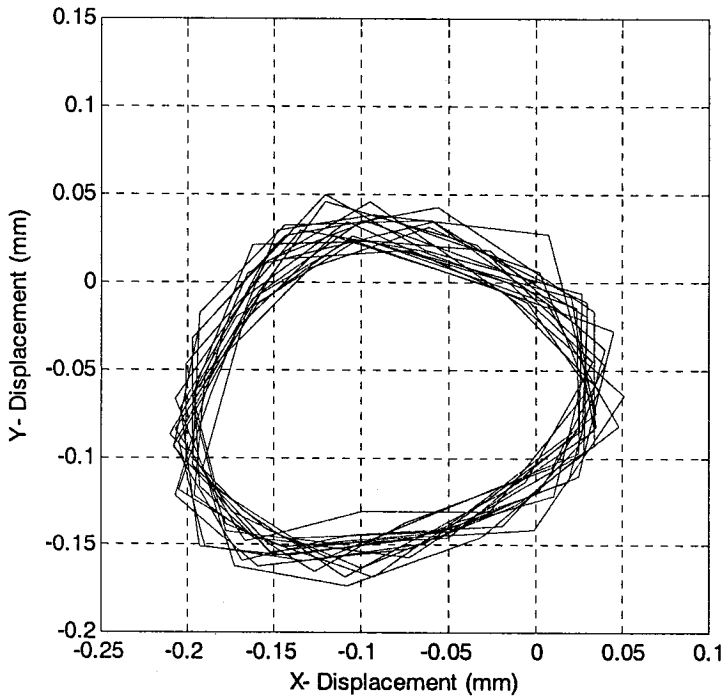

Figure 3.7.16: Whirl Orbit near Drill Tip at 1795 rpm

Figures 3.7.5, 3.7.9, and 3.7.13 represents the time-displacement responses obtained using accelerometers at spindle, for running speeds of 445 rpm, 930 rpm, and 1795 rpm, respectively without performing any cutting operation. Figures 3.7.7, 3.7.11, and 3.7.15 represents the time-displacement responses obtained using proximity sensors near the drill tip at 445 rpm, 930 rpm, and 1795 rpm, respectively. The solid line indicates the displacement in X-direction and the dotted line represents the displacement in Y-direction. Figures 3.7.6, 3.7.10, and 3.7.14, represent the whirl orbits obtained near spindle at 445 rpm, 930 rpm, and 1795 rpm, respectively without performing cutting operation. Figures 3.7.8, 3.7.12, and 3.7.16 shows the whirl orbits obtained near the drill tip, by running the drilling machine without performing the cutting operation at 445 rpm, 930 rpm, and 1795 rpm, respectively, for 6.35 mm diameter drill. The major whirl length is found to be 0.25 mm. The orbits obtained near the drill tip of the constant whirl length are close to the spindle run-out. The increase of speed from 445 rpm to 1795 rpm resulted in the change in the shape of the orbit from 5 lobes to three lobes but no change is noticed in the whirl major length.

3.7b Results for Drill (12.7 mm Diameter)

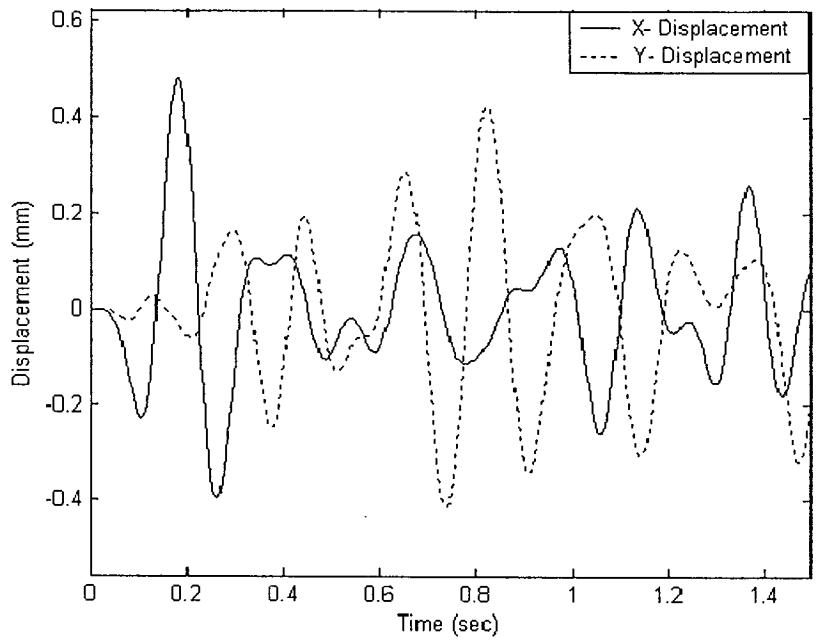

Figure 3.7.17: Time-displacement Response of Spindle at 445 rpm

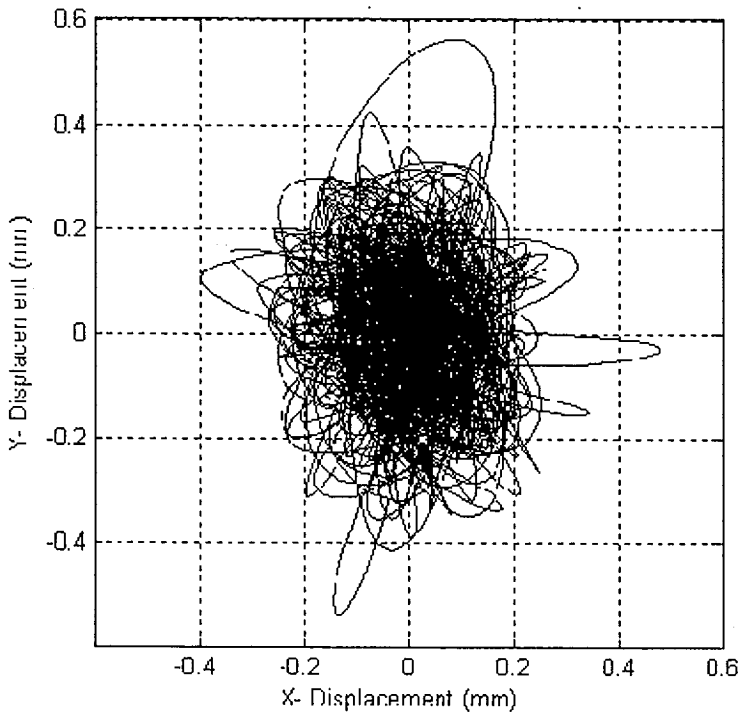

Figure 3.7.18: Whirl Orbit of Spindle at 445 rpm

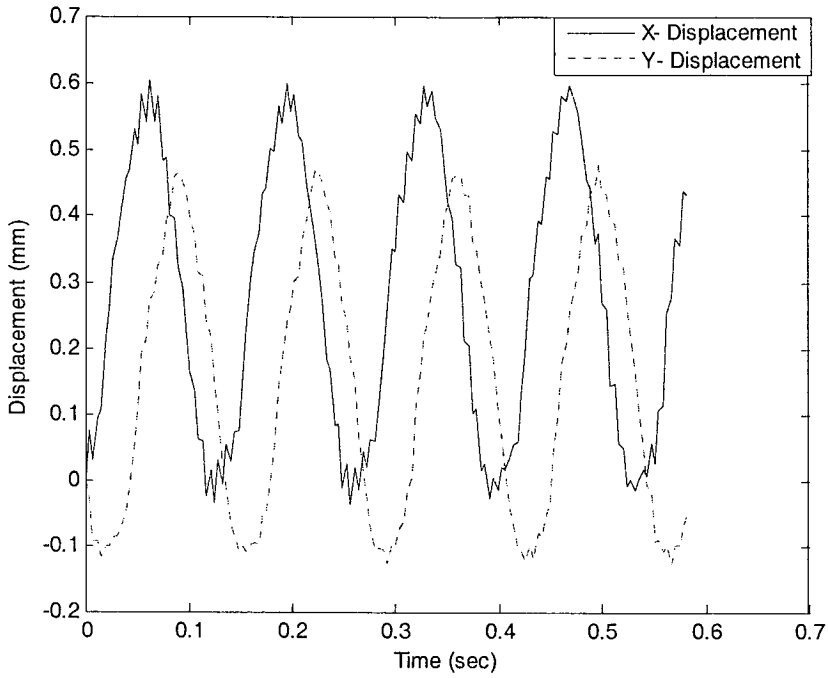

Figure 3.7.19: Time-displacement Response near Drill Tip at 445 rpm

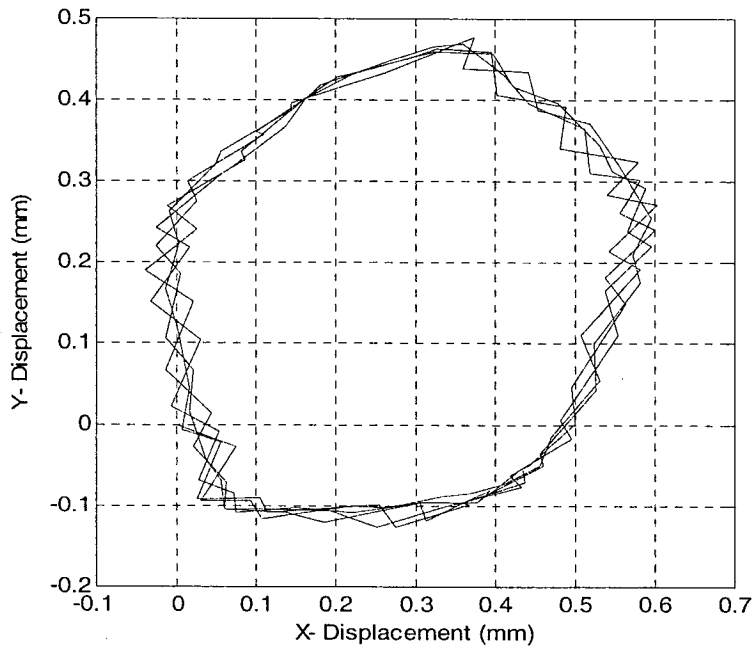

Figure 3.7.20: Whirl Orbit near Drill Tip at 445 rpm

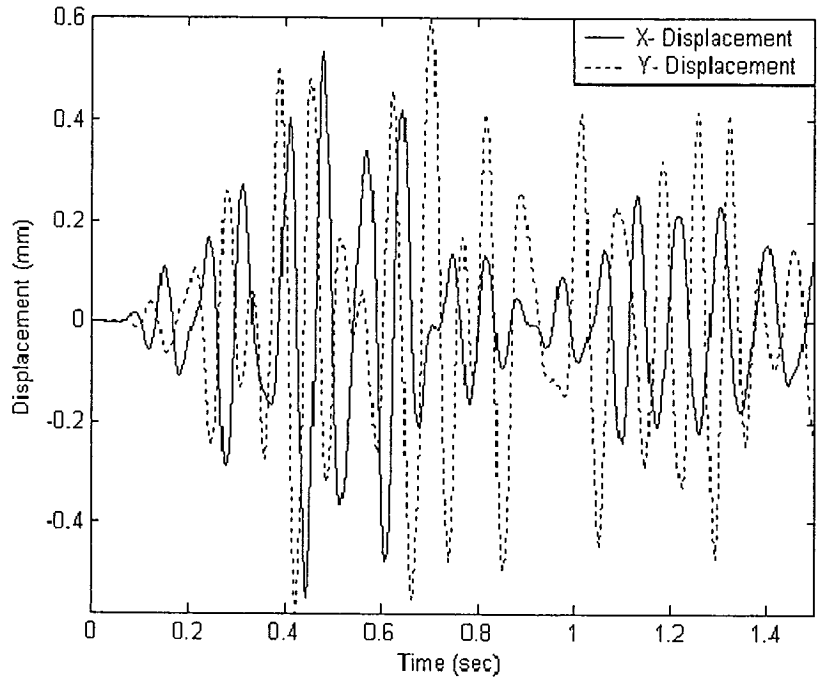

Figure 3.7.21: Time-displacement Response of Spindle at 930 rpm

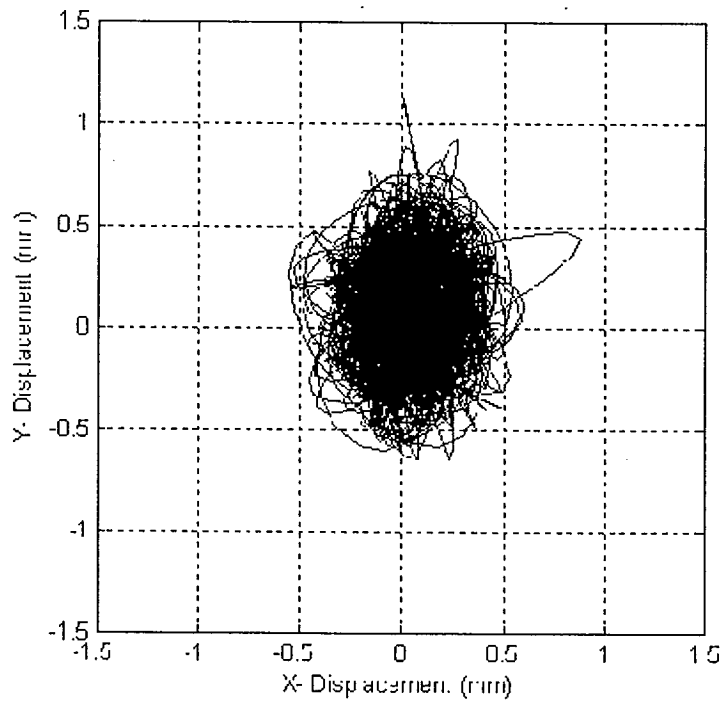

Figure 3.7.22: Whirl Orbit of Spindle at 930 rpm

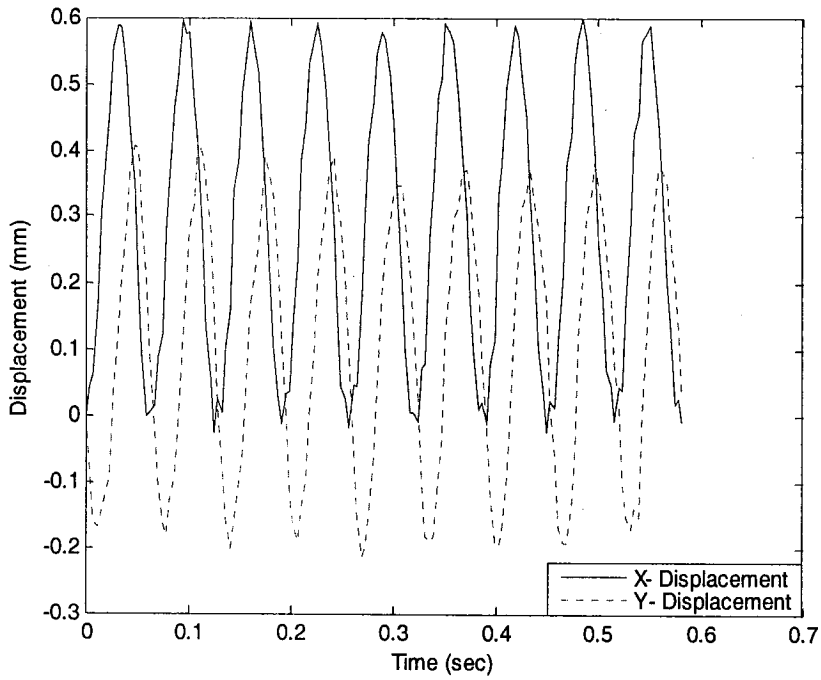

Figure 3.7.23: Time-displacement Response near Drill Tip at 930 rpm

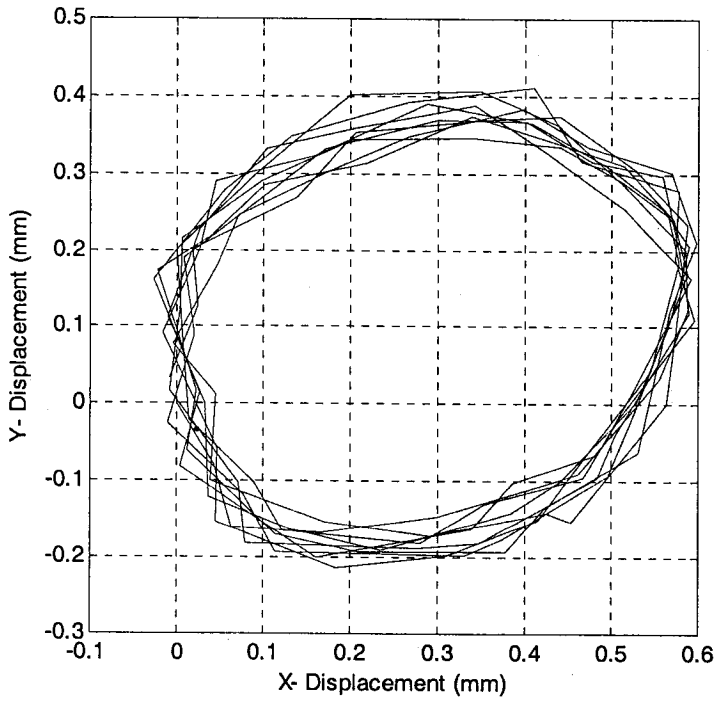

Figure 3.7.24: Whirl Orbit near Drill Tip at 930 rpm

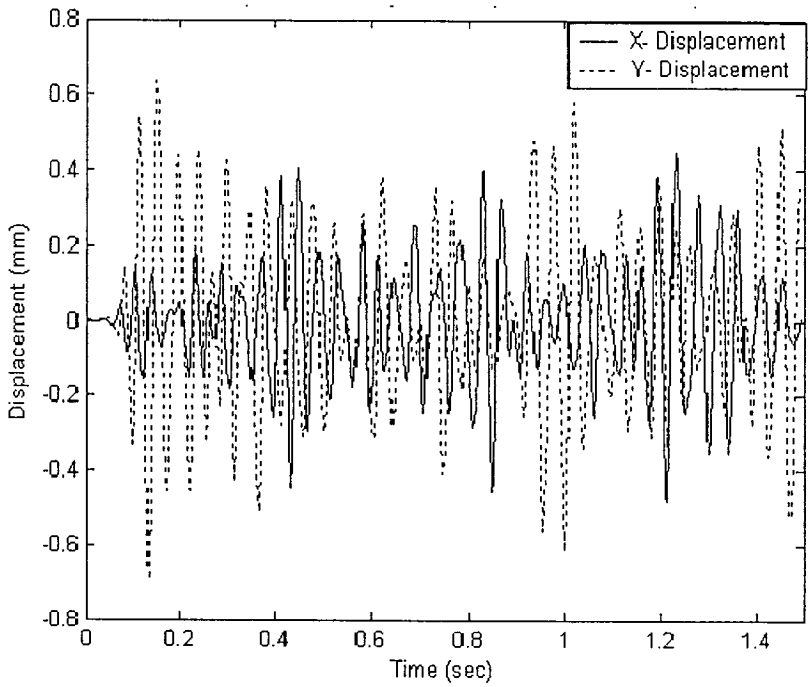

Figure 3.7.25: Time-displacement Response of Spindle at 1795 rpm

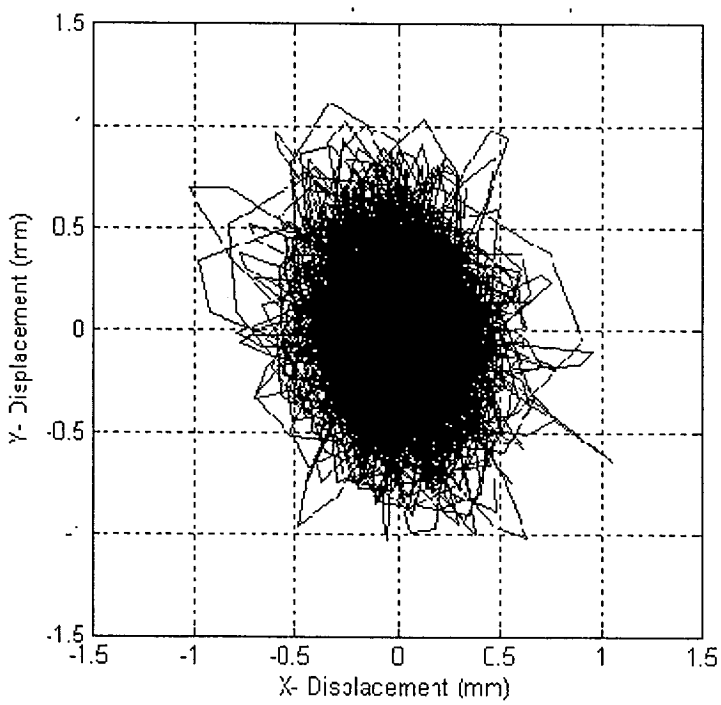

Figure 3.7.26: Whirl Orbit of Spindle at 1795 rpm

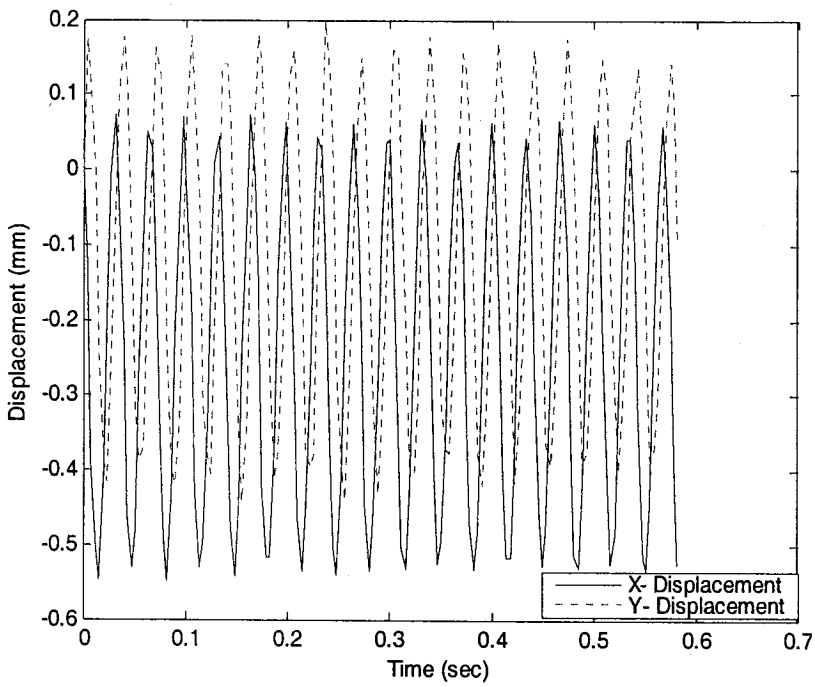

Figure 3.7.27: Time-displacement Response near Drill Tip at 1795 rpm

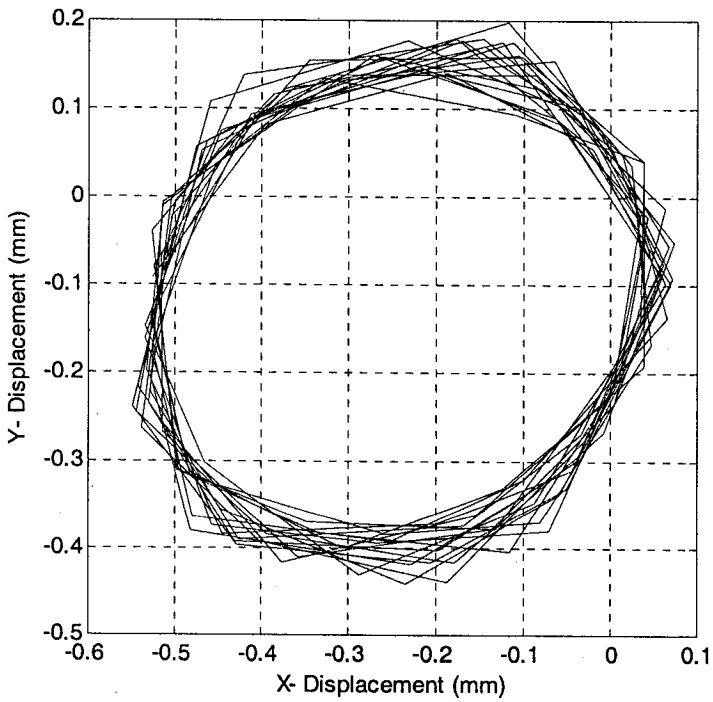

Figure 3.7.28: Whirl Orbit near Drill Tip 1795 rpm

Figures 3.7.17, 3.7.21, and 3.7.25, represents the time-displacement responses obtained using accelerometers at spindle, for running speeds of 445 rpm, 930 rpm, and 1795 rpm, respectively, without performing any cutting operation. Figures 3.7.19, 3.7.23, and 3.7.27, represents the time-displacement responses obtained using proximity sensors near the drill tip at 445 rpm, 930 rpm, and 1795 rpm, respectively. The solid line indicates the displacement in X-direction and the dotted line represents the displacement in Y-direction. Figures 3.7.18, 3.7.22, and 3.7.26, represents the whirl orbits obtained near spindle at 445 rpm, 930 rpm, and 1795 rpm, respectively, without performing cutting operation. Figures 3.7.20, 3.7.24, and 3.7.28, shows the whirl orbits obtained near the drill tip, by running the drilling machine without performing the cutting operation at 445 rpm, 930 rpm, and 1795 rpm, respectively, for 12.7 mm diameter drill. The major whirl length is found to be 0.6 mm. The orbits obtained near the drill tip of the constant whirl length are close to the spindle run-out. The increase of speed from 445 rpm to 1795 rpm resulted in the change in the shape of the orbit, but no change is noticed in the whirl major length.

3.8 Summary

In this Chapter an experimental investigation of drilling machine has been done in order to study the effect of other components of drilling machine on the twist drill transverse motion. The experimental results show that there is some amount of spindle run-out already present in the system, which resulted in the rotation of the twist drill at an eccentricity. One can even observe lobed contour present in the motion when the twist drill is made to rotate freely without performing any cutting operation. The orbits obtained at spindle shows that there is some amount of lateral displacement present in

complete system, which cannot be ignored. A finite element model for Drill-Shaft-Drive assembly is presented in the next chapter and the dynamics of the entire structure is studied.

CHAPTER 4

FINITE ELEMENT ANALYSIS OF DRILLING MACHINE TOOL SYSTEM

In Chapter 3, an experimental investigation has been performed in order to study the effect of drilling machine components on the transverse motion of twist drill. The experimental results showed that combined machine-tool system should be studied for analyzing its dynamic behavior. In the present Chapter, a Finite Element Model for Drill-Shaft-Drive assembly is presented in order to study the dynamics of the complete structure.

4.1 Introduction

The finite element method (FEM) is a numerical analysis method used for solving complex engineering problems. Since the proliferation of modern computers, the FEM has proven to be a powerful tool in the analysis of such problems. This is partly due to the fact that the method benefits from the computer's fast speed in performing the large number of computations associated with the FEM. Another reason is that the FEM can be readily adapted to many different types of engineering problems including stress analysis, heat transfer, fluid flow, and vibration problems.

The drill press used for experiments (in Chapter 3) consists of several parts: spindle, multiple diameter pulley with five different speeds, V-belt, chuck for holding the drill, and 1 HP motor for driving the spindle. For the present analysis, V-belt, multiple

diameter pulley, spindle with bearings, chuck (or tool holder) and drill bit are incorporated into the model. As shown in the figure 4.1 (dimensions specified are in 'mm'), the spindle is supported by single row deep groove ball bearings at B1, B2, and B3, respectively. SKF 6205-2RS type of bearing, supports the spindle at position B1, and FAG WC 88503 type of bearing, supports at B2 and B3, respectively. The dimensions of the bearings are obtained from the bearings manual [33].

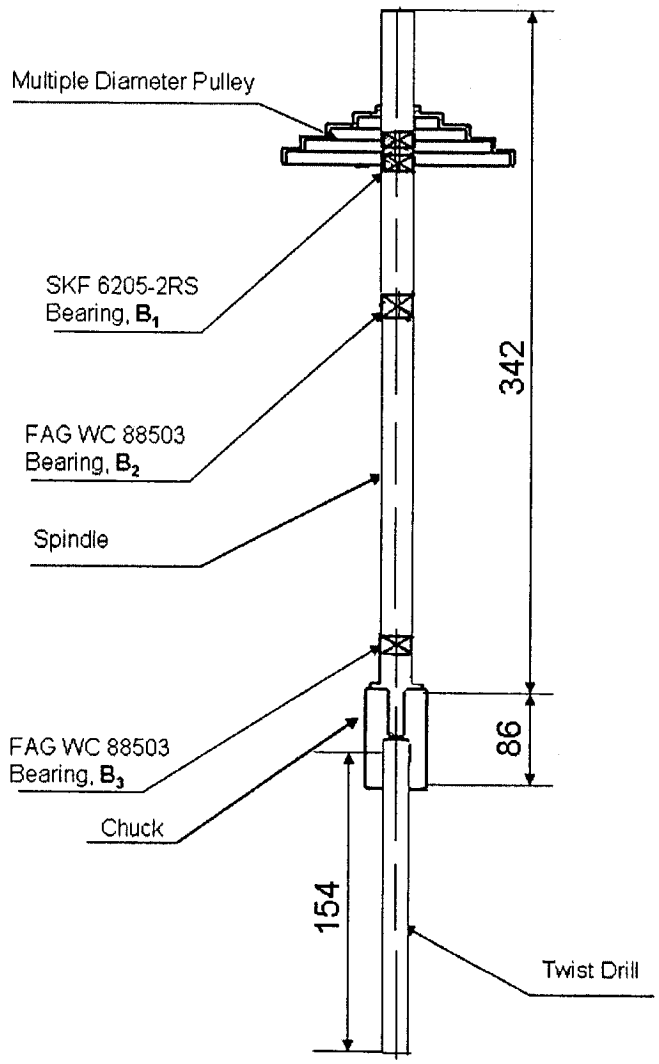

Figure 4.1: A Longitudinal View of Combined Spindle-drill Considered for Study

4.2 Modeling and Analysis of Drill Machine Tool System

4.2.1 Spindle Model

For the present analysis, the spindle is modeled as a shaft supported by a set of bearings, as shown in the simplified sketch in the figure 4.2.1, and this kind of representation has been used in [37, 38, and 39].

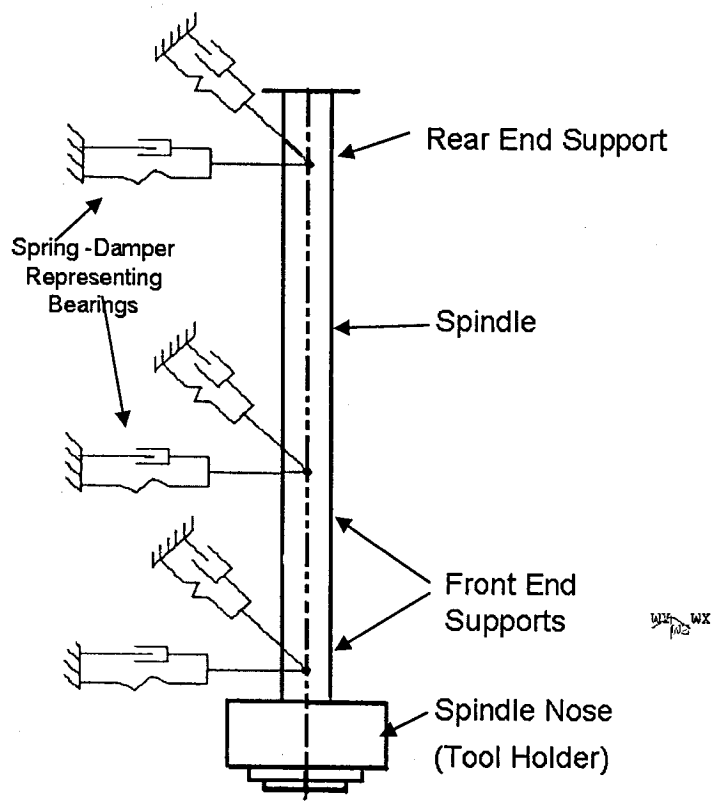

Figure 4.2.1: Simplified Sketch of Spindle [37, 38 and 39]

The spindle is assumed to be a uniform body. This means that there are no significant variations in the material properties and dimensions of the shaft. Further, it is assumed that the bearing supports of the shaft can be modeled as a direct spring-damper system.

4.2.2 Drill bit Model

Researchers have paid considerable attention to the complex geometrical considerations in drill design [40, 41]. In the present model the distributed and twisted shape of the drill bit is not considered, and the drill geometry has been limited to a cylindrical cross-section. It is also assumed that there are no significant variations in the material properties and dimensions of the twist drill.

4.2.3 Multiple Diameter Belt drive Pulley and Chuck

The multiple diameter belt drive pulley has been approximated as a stepped cone pulley and the chuck (or tool holder) as a cylindrical mass.

4.2.4 Element Selection

The spindle and drill bit are meshed with BEAM 44 ANSYS element. It is a uniaxial element with tension, compression, torsion, and bending capabilities. The element has six degrees of freedom at each node, translations in the nodal X, Y, and Z directions and rotations about the nodal X, Y, and Z-axes.

The multiple diameter belt drive pulley and chuck are meshed with MASS 21 ANSYS element. This element is a point element which has six degrees of freedom, translations in the nodal X, Y, and Z directions and rotations about the nodal X, Y, and Z-axes.

The bearing supports, which are considered as equivalent direct spring-dampers are meshed with COMBIN14 ANSYS element. This element has longitudinal or torsional capability in 1D, 2D, or 3D applications. Table 4.2.4a, 4.2.4b, and 4.2.4c give the list of

physical properties, bearing properties and the measured actual part dimensions required for building the model.

Table 4.2.4a: Physical Parameters for Combined Spindle-drill Model

Part Name	Mass (kg)	Mass Moment of Inertia (kg-m^2)		
		I_{xx}	I_{yy}	I_{zz}
Multiple Diameter Cone Pulley	0.716	0.59508e-3	0.59508e-3	0.0010849
Chuck	0.947	0.00073164	0.00073164	0.00029594
Drill	-	Area Moment of Inertia (m^4)		
		I_x	I_y	I_z
		1.277e-9	1.277e-9	2.554e-9

Table 4.2.4b: Bearing Properties

Part Name	Stiffness Coefficient K (N/m)	Damping Coefficient C (N-s/m)
Bearing SKF 6205-2RS [35, 36]	8e7	400
Bearing FAG WC 88503 [35, 36]	6.17e7	154.25

Table 4.2.4c: Part Dimensions

Part Name	Length (m)	Diameter (m)
Spindle	0.342	0.01586
Drill	0.154	0.0127
Chuck	0.086	0.05

The finite element model created by considering the combined spindle and drill with multiple belt pulley drive, direct bearing supports in X and Y directions and chuck are as shown in the figures 4.2.4a and 4.2.4b, respectively, whose model parameters are specified in the table 4.2.4a, table 4.2.4b, and table 4.2.4c, respectively. In the figure 4.2.4a WX, WY, and WZ represents the working plane coordinates along X, Y, and Z axis respectively. The axis of spindle-tool system is Z-axis. The total structure is divided into 14 elements with 15 nodes; each node has six degrees of freedom.

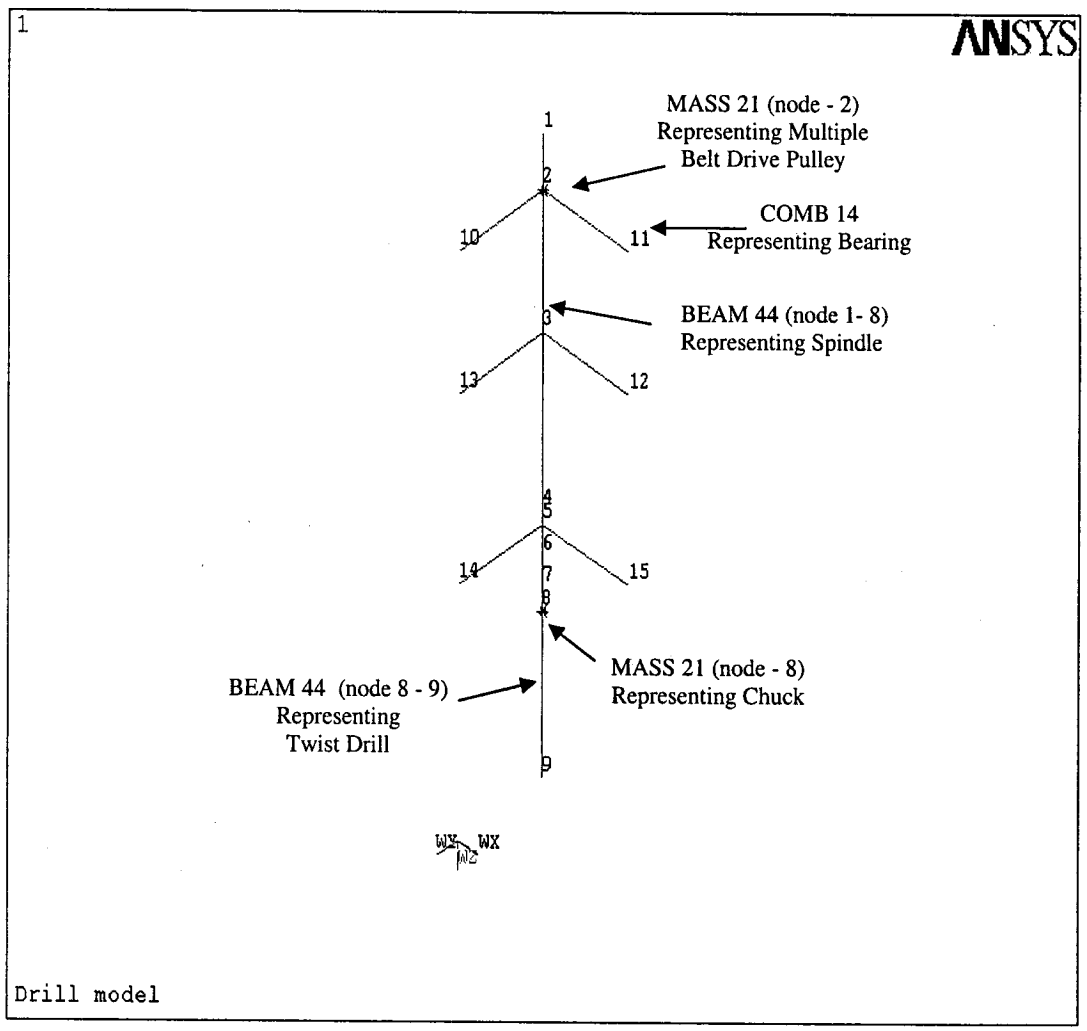

Figure 4.2.4a: 3D Line Model

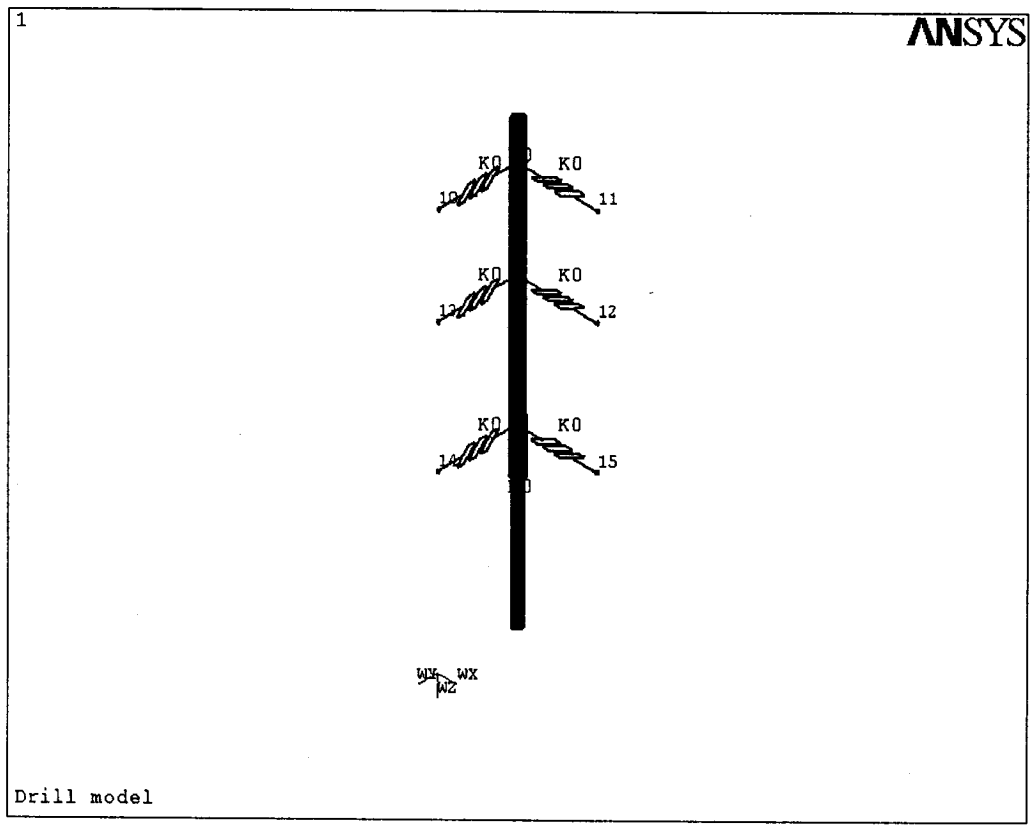

Figure 4.2.4b: 3D Element Model

4.3 Modal Analysis

Modal analysis is generally done to determine the vibration characteristics (natural frequencies and mode shapes) of a structure or a machine component while it is being designed. The natural frequencies and mode shapes are important parameters in the design of a structure for dynamic loading conditions. Several mode extraction methods available in ANSYS 8.1 are: Block Lanczos (default), Subspace, Power Dynamics, Reduced, Unsymmetric, Damped, and QR damped. The default Block Lanczos modal analysis method has been used in the present analyses. The goal is to correlate the natural frequencies of the finite element model (machine-tool structure) to the actual machine tool system test results. The material properties considered for the analysis are as shown in table 4.3.

Table 4.3: Material Properties

Element	Material Type	Modulus of Elasticity (N / m^2)	Density (kg / m^3)	Poisson's ratio (ν)
BEAM 44	Steel AISI-C1020	2.07 e11	7850	0.29
MASS 21	-	-	-	-
COMBINATION 14	-	-	-	-

The structure is supported by the bearings at nodal points 2, 3, and 5, respectively, as shown in figure 4.2.4a. The bending natural frequencies of the system are found by imposing the boundary conditions at the nodal points 1 through 9 with the axial and rotational degrees of freedom (i.e., Z and R_Z) constrained. At nodal points 10, 11, 12, 13, 14, and 15 all degrees of freedom (X, Y, Z, R_X, R_Y and R_Z) are constrained, and hence the

entire structure has 36 active degrees of freedom and the first ten natural frequencies are extracted.

4.3.1 Validation

For vibration analyses, using the FEM, the natural frequencies of the lower modes can be determined more accurately than the higher modes [42, 43]. Typically, only enough eigenvalues whose total mass participation factor equals about 80% to 90% of the object's actual mass are needed to accurately describe how a part vibrates [44]. Therefore, in order to have an initial estimate of what the natural frequency of the machine tool should be, the minimum first natural frequency was determined using modal testing experiment (3.4 Modal Testing, Chapter 3) and it was found to be 148-150 Hz.

The fundamental natural frequency obtained using modal analysis (FEM) is 155.955 Hz, which is close to the value obtained using modal testing (Chapter 3). In general 5% is a standard accuracy used to correlate the natural frequencies of a finite element model to actual test results [44]. Hence, the present finite element model is considered to be representative of the actual machine-tool system.

4.3.2 Results

The first 10 mode shapes are shown in the figures from 4.3.2i to 4.3.2x. The list of tables from 4.3.2a until 4.3.2j which summarize the nodal displacements for the first 10 natural frequencies of the system and the tables from 4.3.2k to 4.3.2p which provide the details for mass participation factors are provided in Appendix.

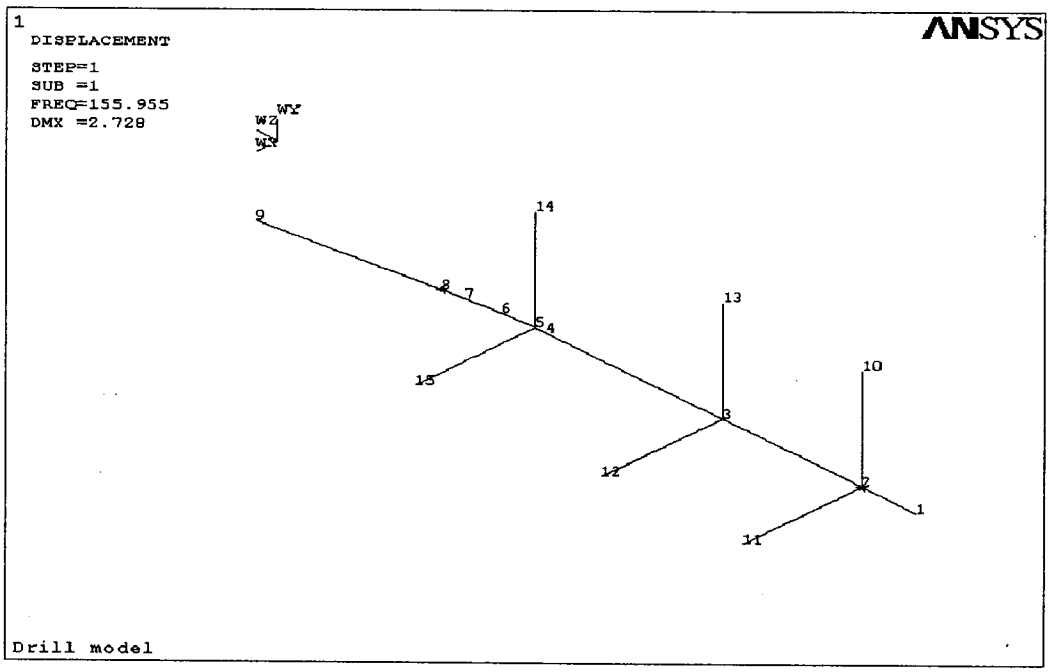

Figure 4.3.2i: First Mode

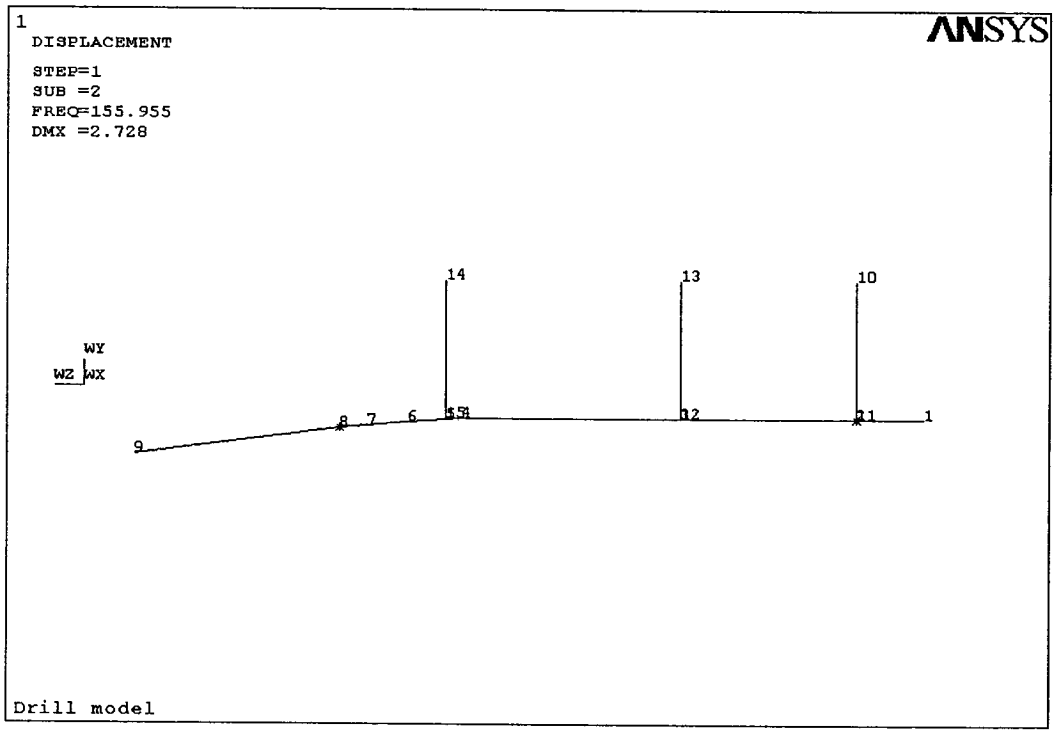

Figure 4.3.2ii: Second Mode

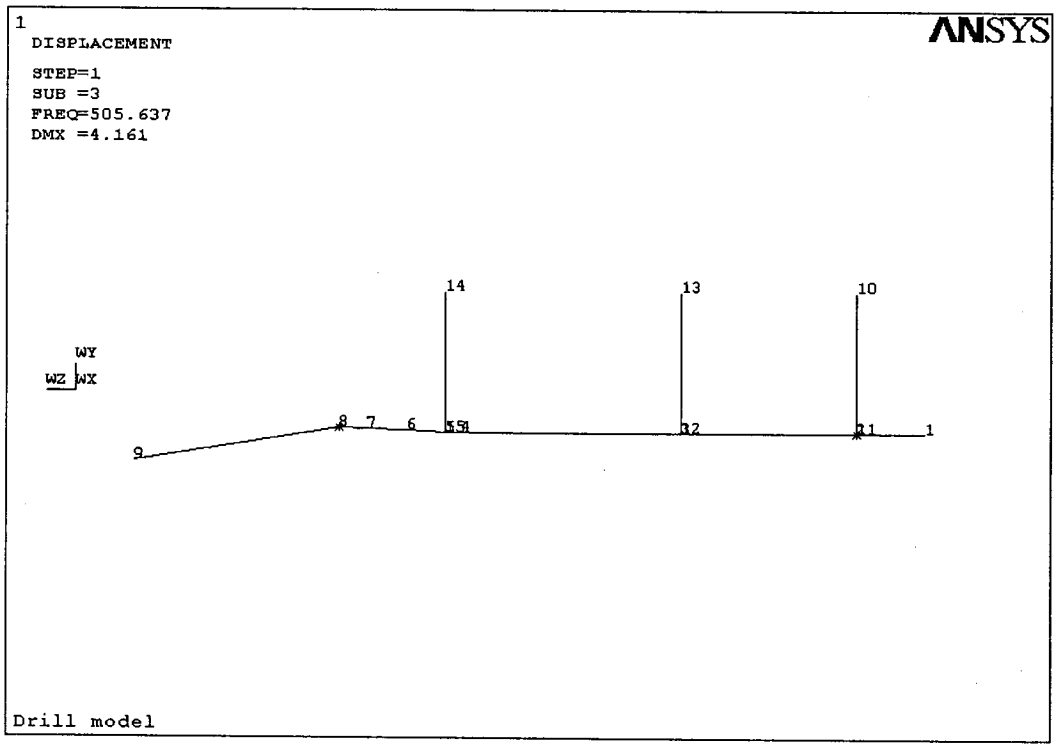

Figure 4.3.2iii: Third Mode

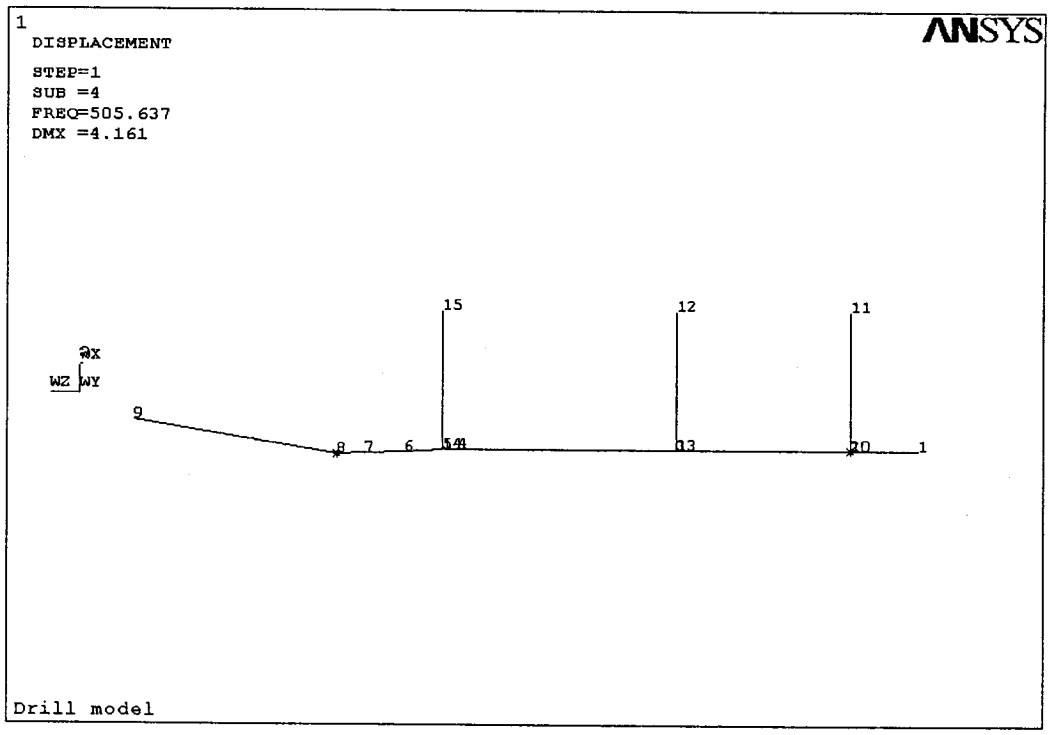

Figure 4.3.2iv: Fourth Mode

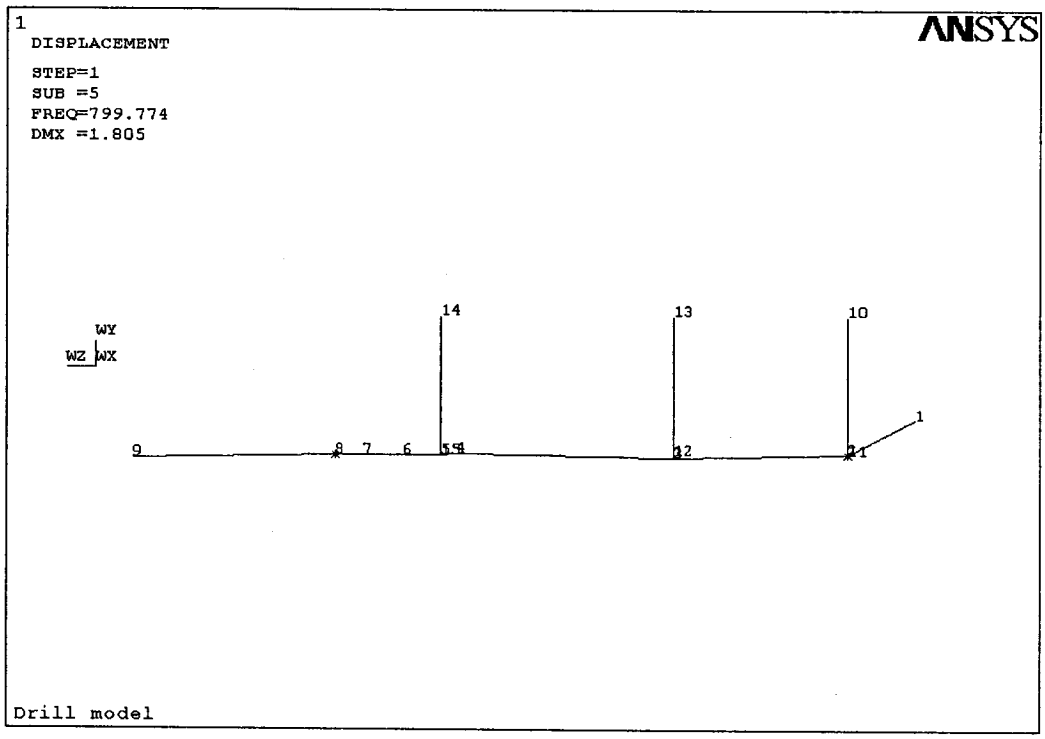

Figure 4.3.2v: Fifth Mode

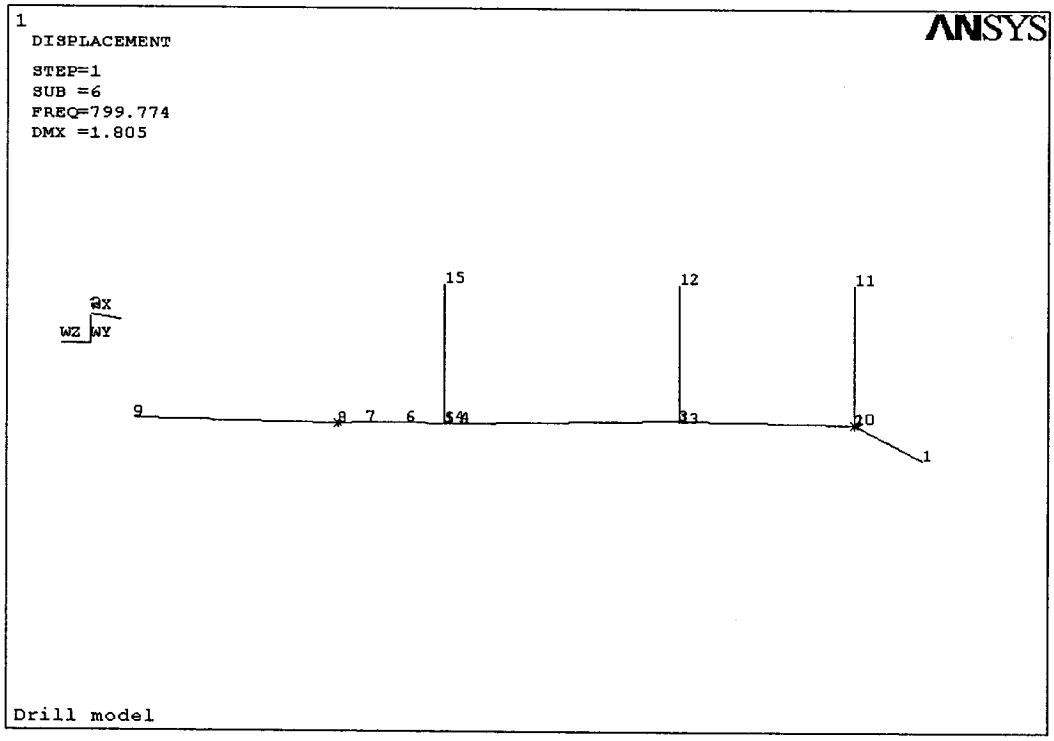

Figure 4.3.2vii: Sixth Mode

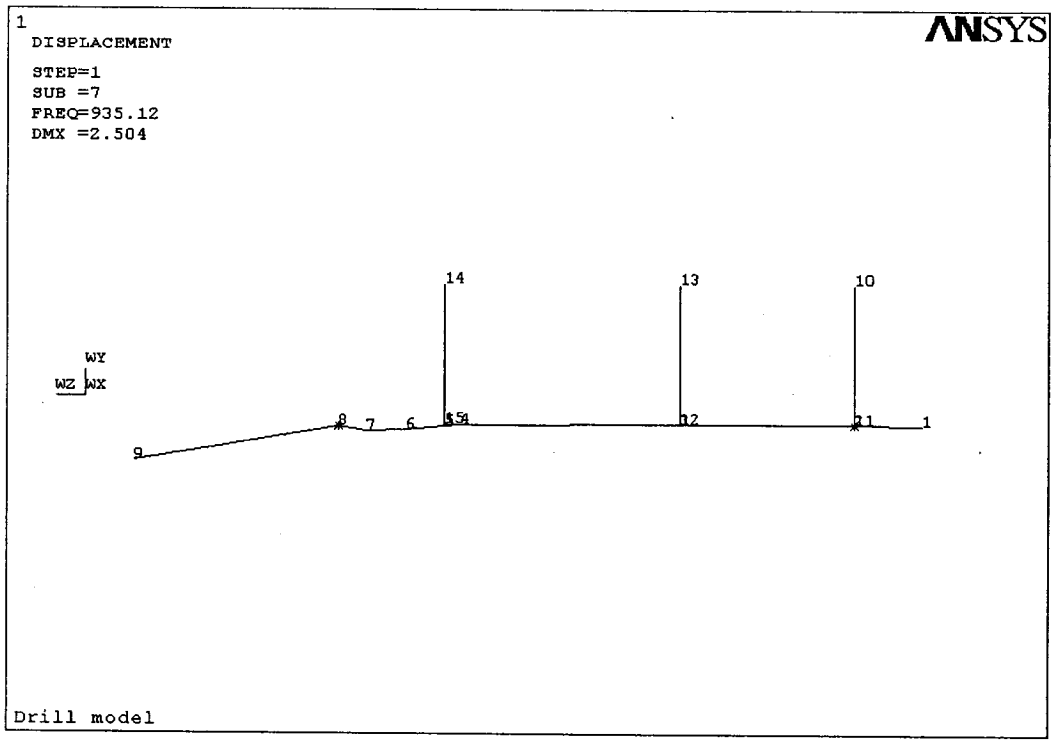

Figure 4.3.2vii: Seventh Mode

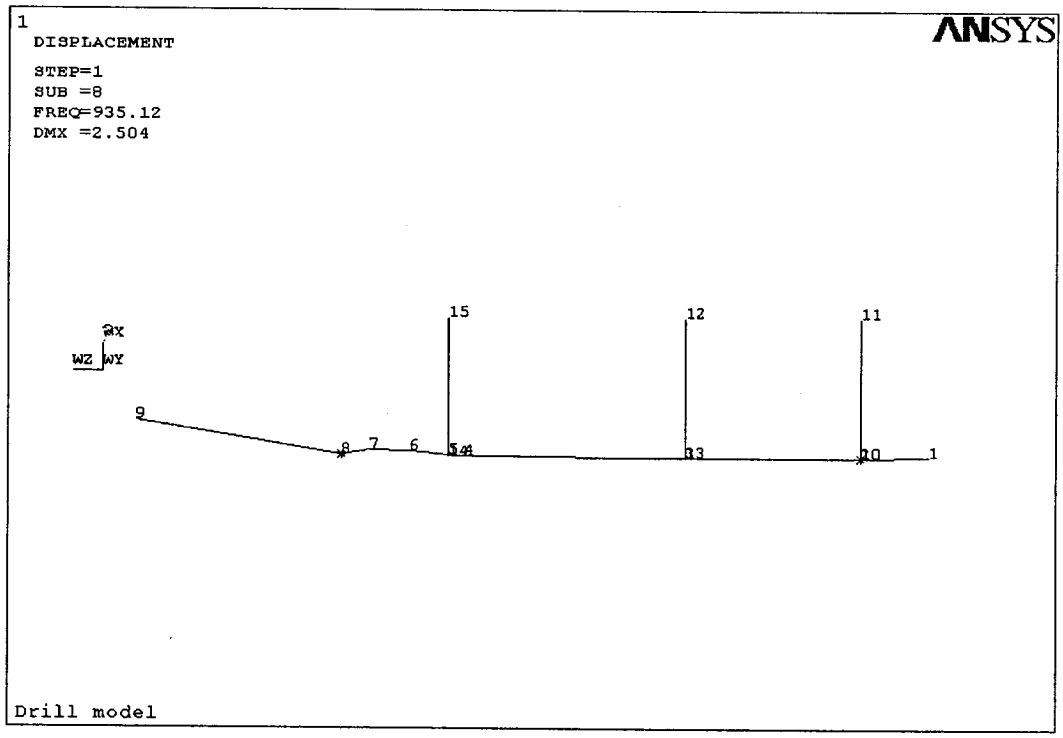

Figure 4.3.2viiiii: Eight Mode

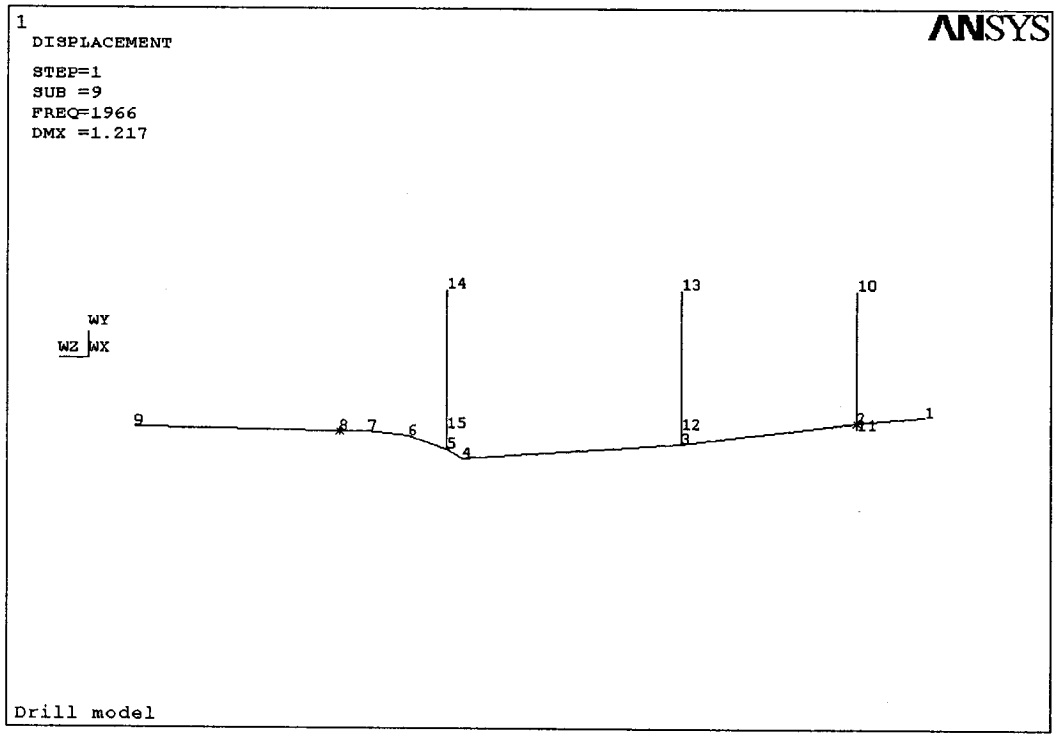

Figure 4.3.2ix: Ninth Mode

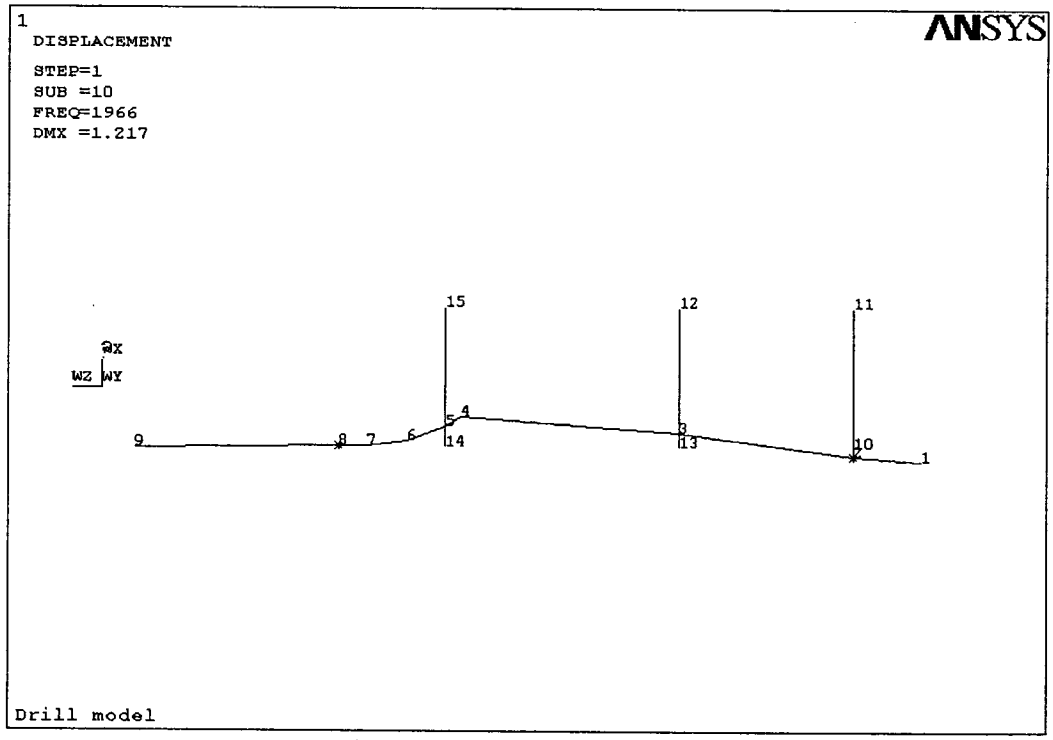

Figure 4.3.2x: Tenth Mode

4.3.3 Discussion

Referring to the tables 4.3.2k to 4.3.2p from Appendix, during the first mode of vibration the maximum effective mass is concentrated in X-direction, hence the first mode of vibration is in that direction. Comparing the nodal displacements UX, UY, UZ, ROTX, ROTY, and ROTZ in table 4.3.2a from Appendix, the maximum displacement is occurring at node 9 (UX = 2.7273 normalized linear displacement) and maximum rotation is ROTY = 15.876 (normalized rotational displacement) hence the first mode is more dominant in X-direction which can be seen from the figure 4.3.2i.

During the second mode of vibration the maximum effective mass is concentrated in Y-direction, hence the second mode is in that direction and comparing the nodal displacements in table 4.3.2b from Appendix, at node 9 the maximum displacement UY is -2.7273 (normalized linear displacement) and maximum rotation ROTX is 15.876 (normalized rotational displacement) hence, the second mode is more dominant in Y-direction. The negative sign indicates the direction of bending, which is in the negative Y-direction that can be seen from the figure 4.3.2ii. A similar kind of explanation can be given for the remaining eight modes of vibration.

From the above analysis one can estimate the behavior of the structure; it can be seen from the mode shapes (figure 4.3.2i to 4.3.2x) that the structure is subjected to larger amount of bending at the drill tip (node 9) during the first four modes of vibrations.

4.4 Transient Dynamic Analysis

Transient dynamic analysis (also called as time-history analysis) is a technique used to determine the dynamic response of a structure under the action of any general time-dependent loads. This type of analysis is used to determine the time-varying displacements, strains, stresses, and forces in a structure as it responds to any combination of static, transient, and harmonic loads. The time-scale of the loading is such that the inertia or damping effects are considered to be important.

There are three methods available in ANSYS for transient dynamic analysis: Full method, Mode Superposition Method, and Reduced Method. For the present analysis Full Method is employed because, it uses the full system matrices. In dynamic analysis of structures damping plays a vital role. However, due to the limitation in our knowledge about damping the most effective way to treat damping within modal analysis framework is to treat the damping value as an equivalent Rayleigh damping in the form $[C] = \alpha^* [M] + \beta [K]$.

where,

[C] = damping matrix of the physical system,

[M] = mass matrix of the physical system,

[K] = stiffness matrix of the system,

α^* and β are mass proportional and stiffness proportional damping constants. In many practical structural problems, alpha damping (or mass damping) may be ignored. For the present analysis stiffness proportional damping is considered. The damping ratio of 0.1456 is obtained for first mode from experimental results. In general the relation

between the mass proportional damping constant and stiffness proportional damping constant is given by, $\xi_i^* = \alpha^*/2\omega_i + \beta\omega_i/2$. Since only stiffness proportional damping is considered $\alpha^* = 0$ so that $\xi_i^* = \beta\omega i/2$ and therefore for 0.1456 damping ratio the value of β is 0.0003.

The analysis is done with and without considering the belt tensions acting on the multiple sleeve pulley.

4.4.1 Without Belt Tension

In this analysis, the dynamic behavior of the combined Spindle-drill structure as shown in the figure 4.2.4a is analyzed by exciting the structure with unbalance force generated during cutting process. The unbalance force functions (2.3 Cutting Force Imbalance Consideration, Chapter 2)

$$F_{imbx} = F_{imb}^{**}\{1-\lambda\sin(3\omega t)\}\cos(\omega t+\phi) \text{ and}$$

$$F_{imby} = F_{imb}^{**}\{1-\lambda\sin(3\omega t)\}\sin(\omega t+\phi)$$

as considered in dimensional form, are applied as loading conditions at node 9 in X and Y directions, respectively, which represents cutting edge forces as shown in the figure 4.4a. The time-varying displacements are collected in both X and Y directions at different nodal points on the structure and the orbital plots are obtained. The above analysis is performed for different values of forcing frequencies, amplitude modulation factor λ, and imbalance cutting force amplitude F_{imb}^{**}.

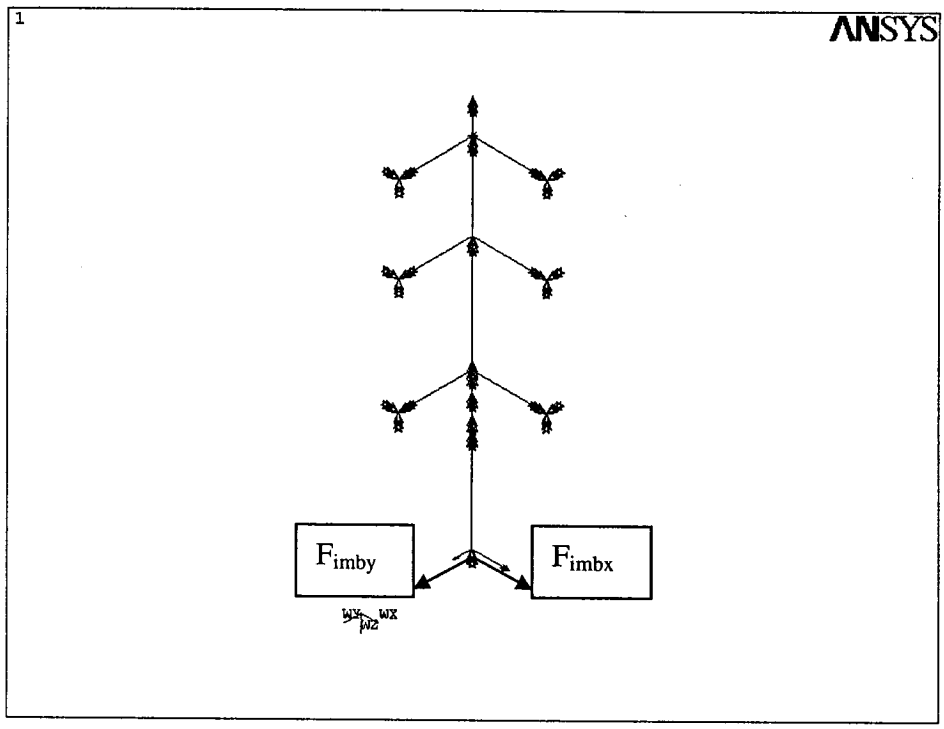

Figure 4.4 a: Spindle-drill System Subjected to Cutting Forces in X and Y directions

4.4.2 Results

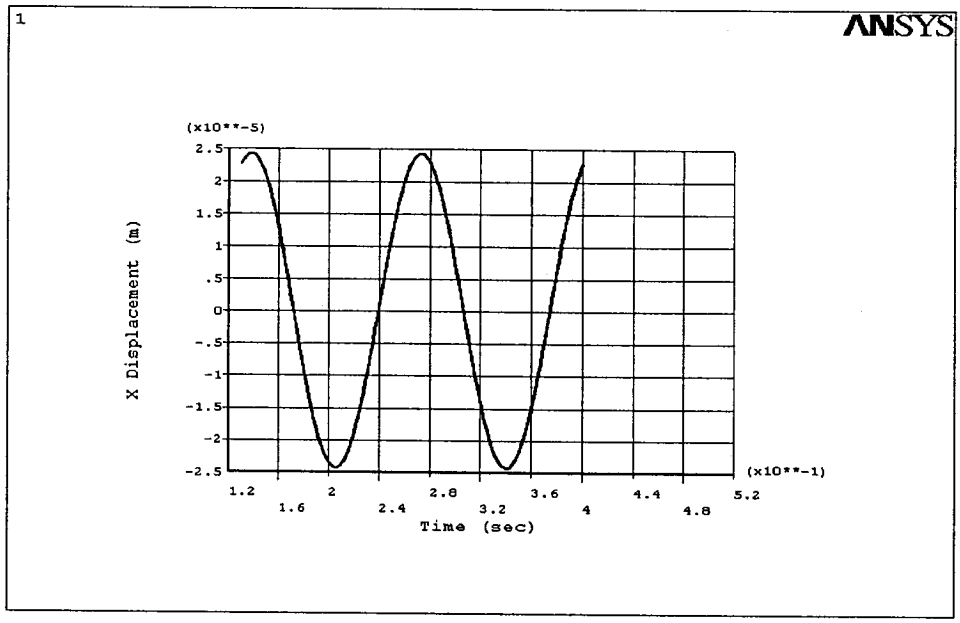

Figure 4.4.2a: Time-displacement Response in X-Direction for $\lambda = 0, \phi = 0.1$ Imbalance Force Amplitude = 2.5 N and Forcing Frequency = 46.57 rad/sec at Drill Tip (node 9)

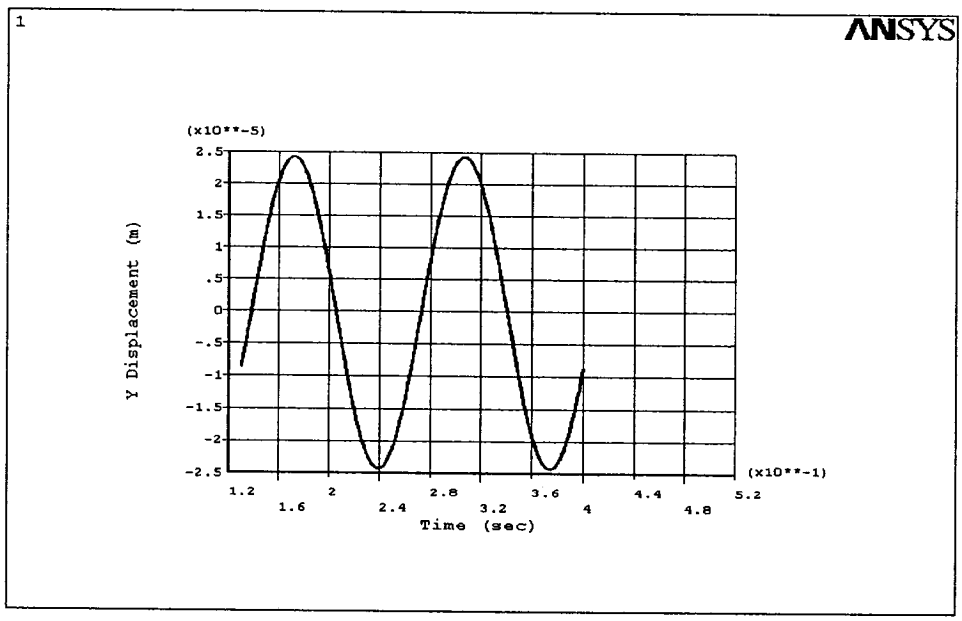

Figure 4.4.2b: Time-displacement Response in Y-Direction for $\lambda = 0, \phi = 0.1$ Imbalance Force Amplitude = 2.5 N and Forcing Frequency = 46.57 rad/sec at Drill Tip (node 9)

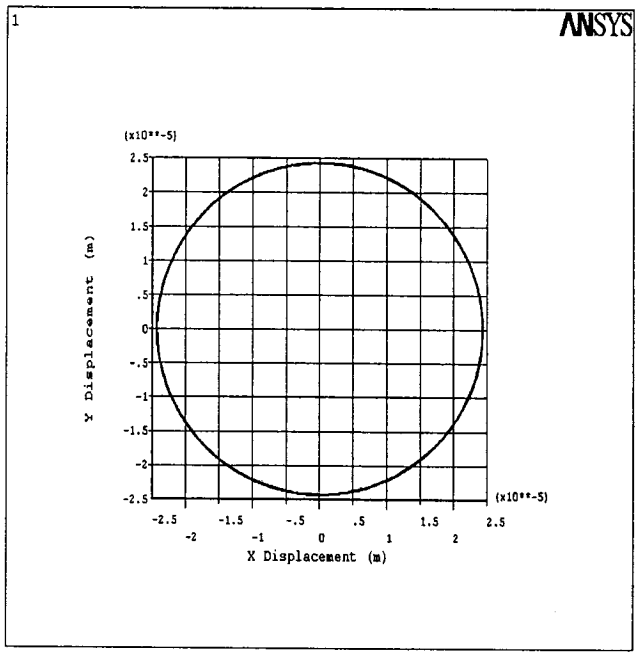

Figure 4.4.2c: Orbital Plot for $\lambda = 0, \phi = 0.1$, Imbalance Force Amplitude = 2.5 N and Forcing Frequency = 46.57 rad/sec at Drill Tip (node 9)

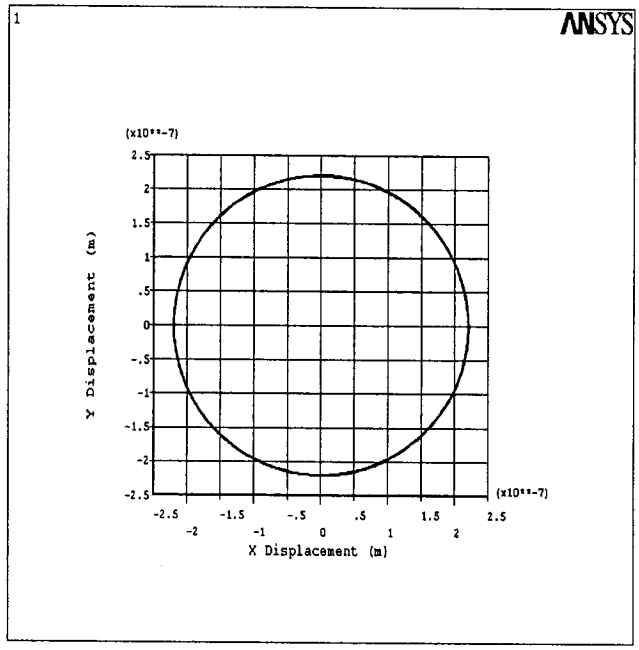

Figure 4.4.2d: Orbital Plot for $\lambda = 0, \phi = 0.1$, Imbalance Force Amplitude = 2.5 N and Forcing Frequency = 46.57 rad/sec at Spindle (node 4)

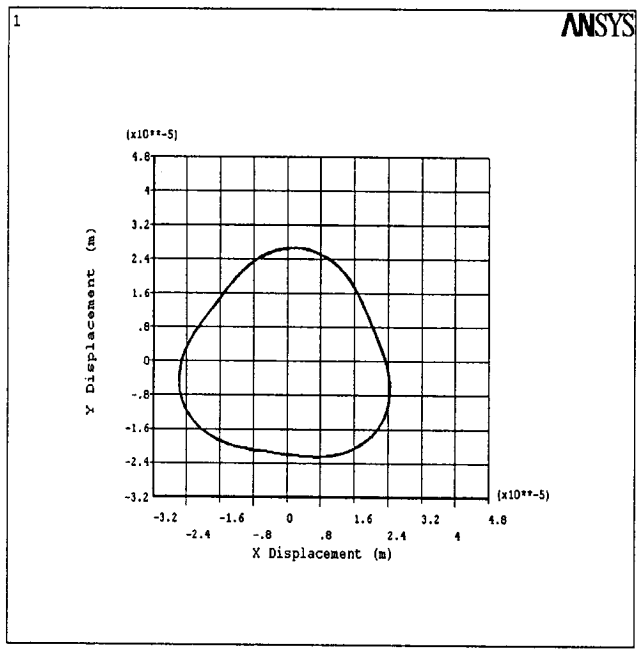

Figure 4.4.2e: Orbital Plot for $\lambda = 0.1, \phi = 0.1$, Imbalance Force Amplitude = 2.5 N and Forcing Frequency = 46.57 rad/sec at Drill Tip (node 9)

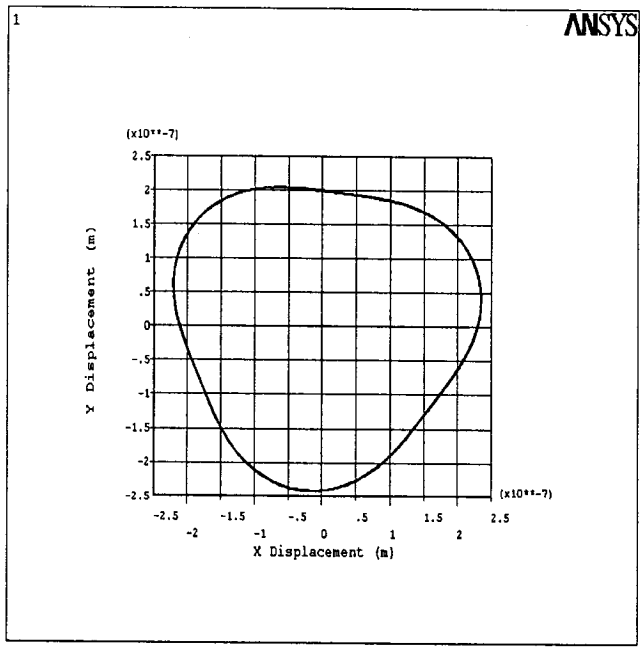

Figure 4.4.2f: Orbital Plot for $\lambda = 0.1, \phi = 0.1$, Imbalance Force Amplitude = 2.5 N and Forcing Frequency = 46.57 rad/sec at Spindle (node 4)

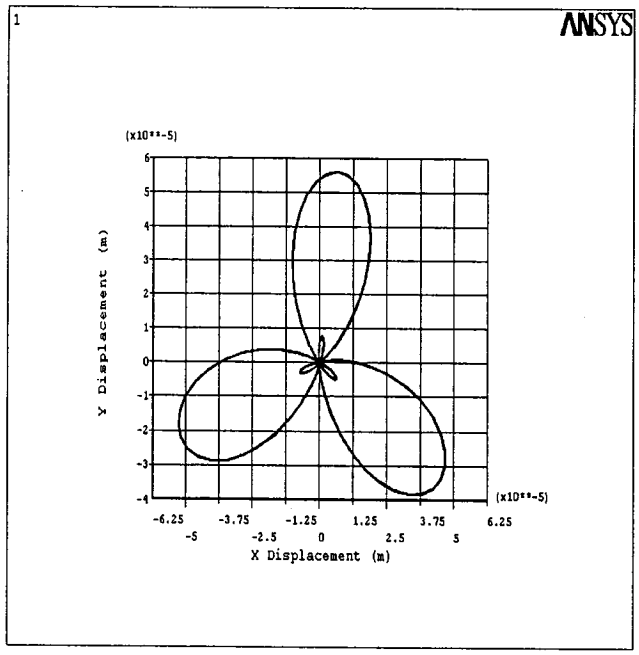

Figure 4.4.2g: Orbital Plot for $\lambda = 1.3, \phi = 0.1$, Imbalance Force Amplitude = 2.5 N and Forcing Frequency = 46.57 rad/sec at Drill Tip (node 9)

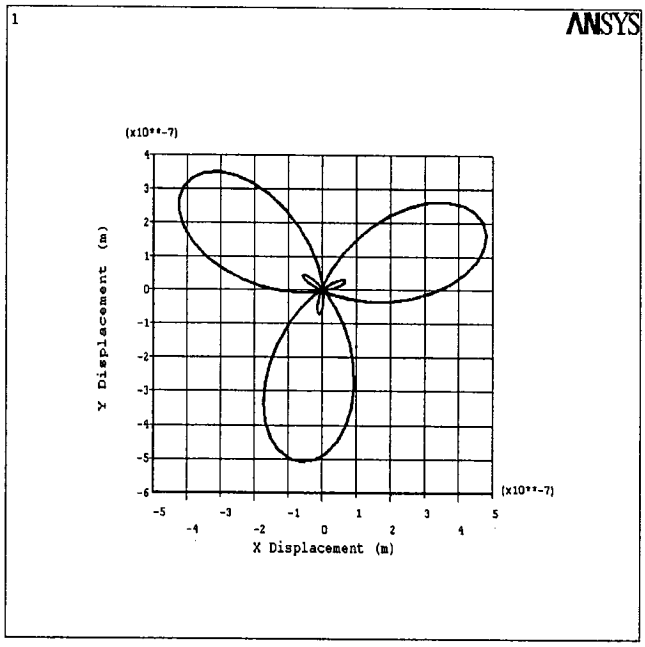

Figure 4.4.2h: Orbital Plot for $\lambda = 1.3, \phi = 0.1$, Imbalance Force Amplitude = 2.5 N and Forcing Frequency = 46.57 rad/sec at Spindle (node 4)

The figures 4.4.2a and 4.4.2b represent time-displacement response obtained in X and Y directions at the twist drill tip (at node 9) when the cutting force imbalance of 2.5 N and forcing frequency of 46.57 rad/sec was considered, without any cutting force amplitude modulation. Figures 4.4.2c and 4.4.2d represents the whirl orbits obtained at node 9 and node 4, respectively. Figures 4.4.2e and 4.4.2g represents the whirl orbits obtained at node 9 (at drill tip) by considering different cutting force modulation factors, with force amplitude of 2.5 N and forcing frequency of 46.57 rad/sec, and figures 4.4.2f and 4.4.2h represents the orbits obtained at node 4. The orbits obtained at node 4 are similar to that obtained at node 9. The above figures show that there is some amount of lateral displacement occurring at the spindle (node 4) too.

Figures 4.4.2e and 4.4.2f represents the orbits obtained at node 9 and node 4 for the twist drill and spindle, respectively, for a force modulation factor of 0.1 with all other parameters remaining same as explained before. One can observe a three lobed orbit at node 4 which is found to be 180° out of phase when compared with the orbit at node 9. Three lobed orbit behavior is observed as discussed in Chapter 3. A similar kind of explanation can be given for the figures 4.4.2g and 4.4.2h, respectively.

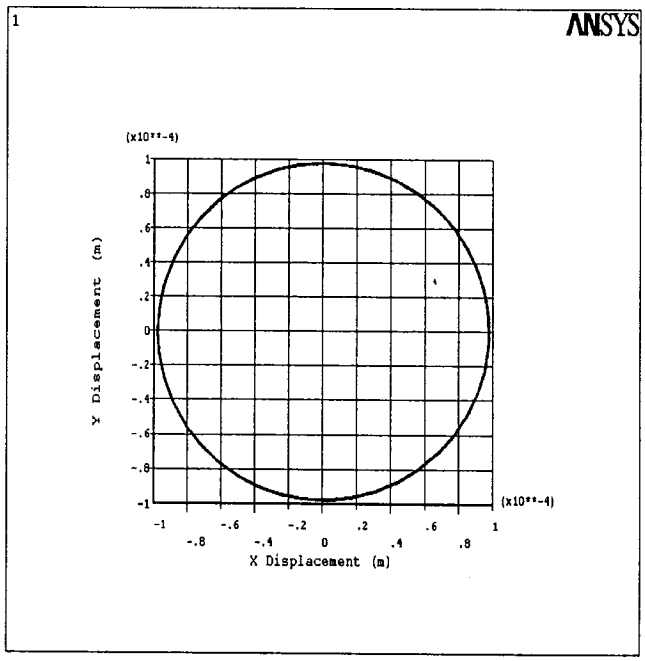

Figure 4.4.2i: Orbital Plot for $\lambda = 0, \phi = 0.1$, Imbalance Force Amplitude = 10 N and Forcing Frequency = 97.34 rad/sec at Drill Tip (node 9)

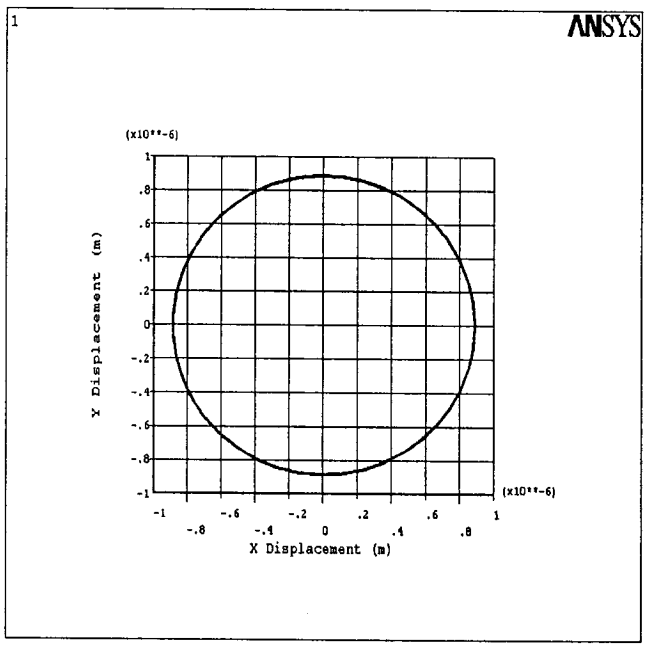

Figure 4.4.2j: Orbital Plot for $\lambda = 0, \phi = 0.1$, Imbalance Force Amplitude = 10 N and Forcing Frequency = 97.34 rad/sec at Spindle (node 4)

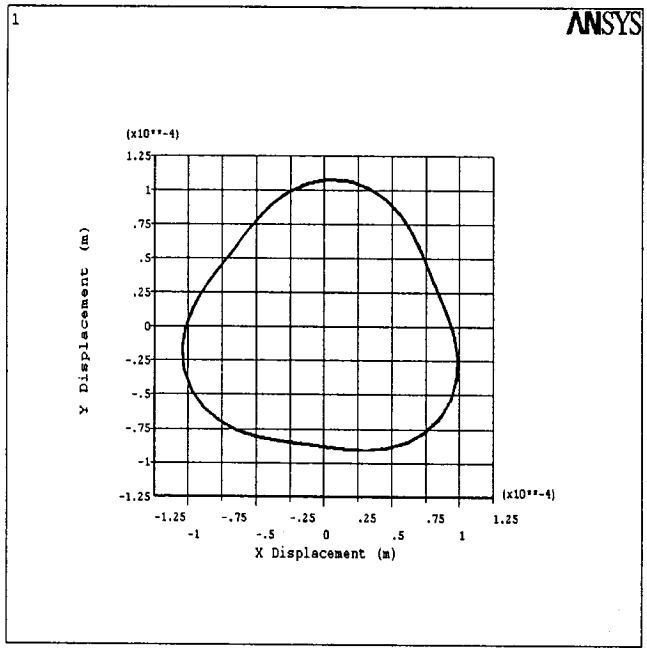

Figure 4.4.2k: Orbital Plot for $\lambda = 0.1, \phi = 0.1$, Imbalance Force Amplitude = 10 N and Forcing Frequency = 97.34 rad/sec at Drill Tip (node 9)

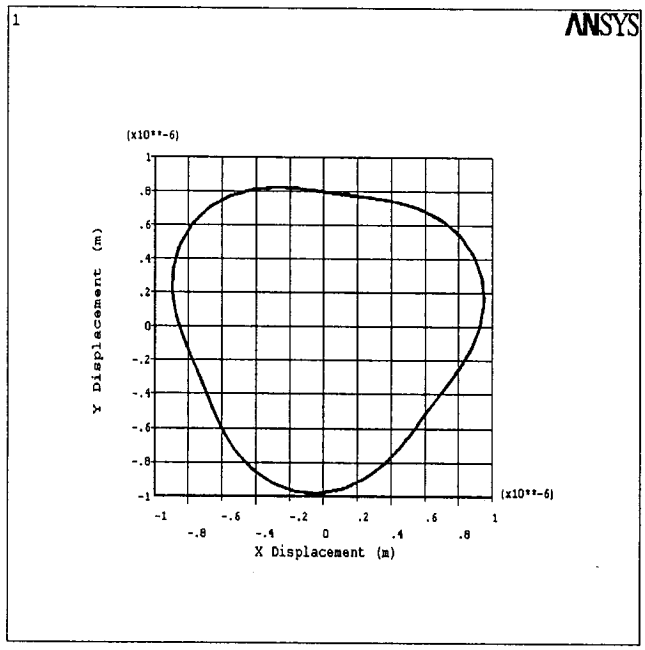

Figure 4.4.2l: Orbital Plot for $\lambda = 0.1, \phi = 0.1$, Imbalance Force Amplitude = 10 N and Forcing Frequency = 97.34 rad/sec at Spindle (node 4)

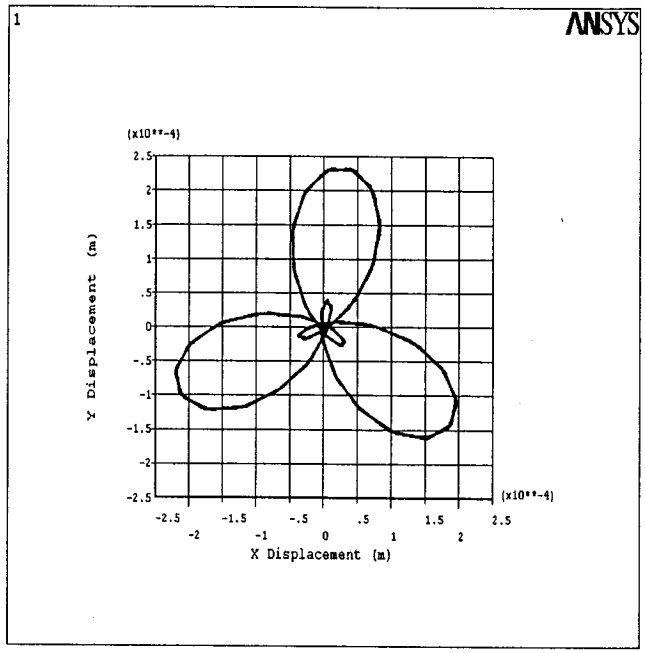

Figure 4.4.2m: Orbital Plot for $\lambda = 1.3, \phi = 0.1$, Imbalance Force Amplitude = 10 N and Forcing Frequency = 97.34 rad/sec at Drill Tip (node 9)

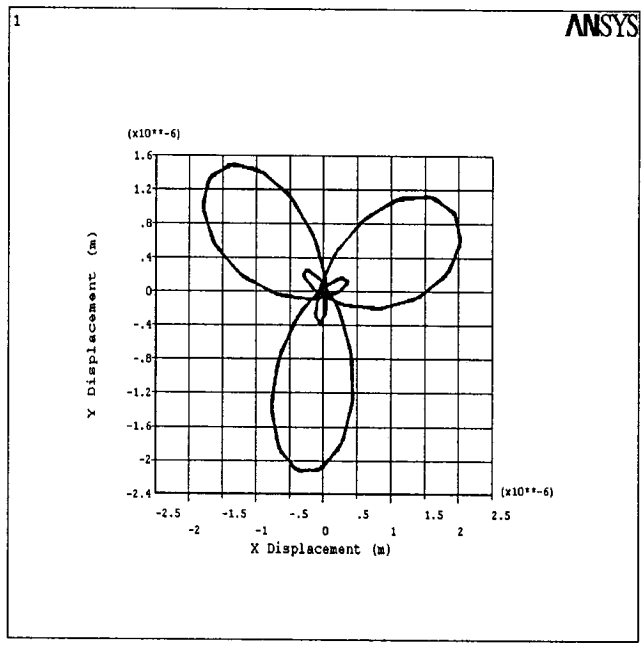

Figure 4.4.2n: Orbital Plot for $\lambda = 1.3, \phi = 0.1$, Imbalance Force Amplitude = 10 N and Forcing Frequency = 97.34 rad/sec at Spindle (node 4)

Figures 4.4.2i, 4.4.2k, and 4.4.2m, represent the orbits at drill tip (node 9) and figures 4.4.2j, 4.4.2l, and 4.4.2n, represent the orbits at spindle (node 4), which are obtained by considering the cutting force imbalance amplitude of 10 N and forcing frequency of 97.34 rad/sec by varying the cutting force amplitude modulation factor λ. One can observe a change in the orbit from circle to three lobed shape. Increasing the forcing frequency did not affect the shape of the orbit. The orbital shapes remained same as discussed in the figures 4.4.2a to 4.4.2.h, but one can observe a change in the whirl major amplitude which is more for the present simulation condition, because of increase in force imbalance amplitude.

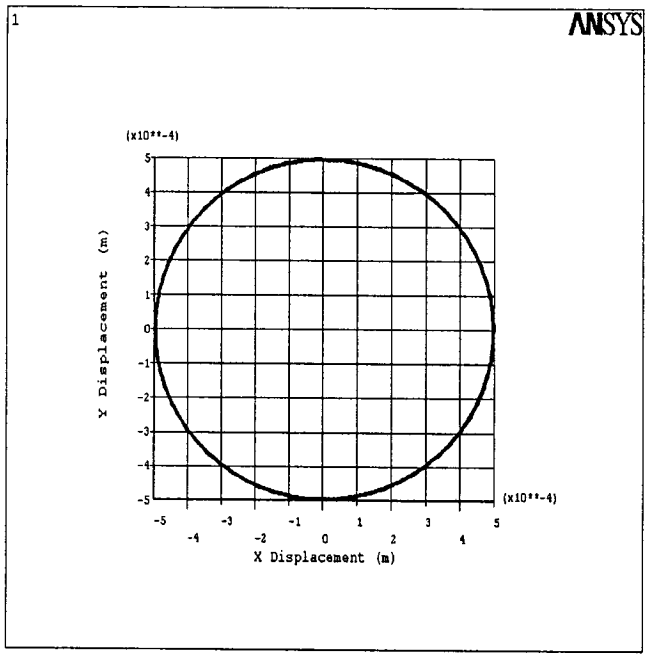

Figure 4.4.2o: Orbital Plot for $\lambda = 0, \phi = 0.1$, Imbalance Force Amplitude = 50 N and Forcing Frequency = 187.87 rad/sec at Drill Tip (node 9)

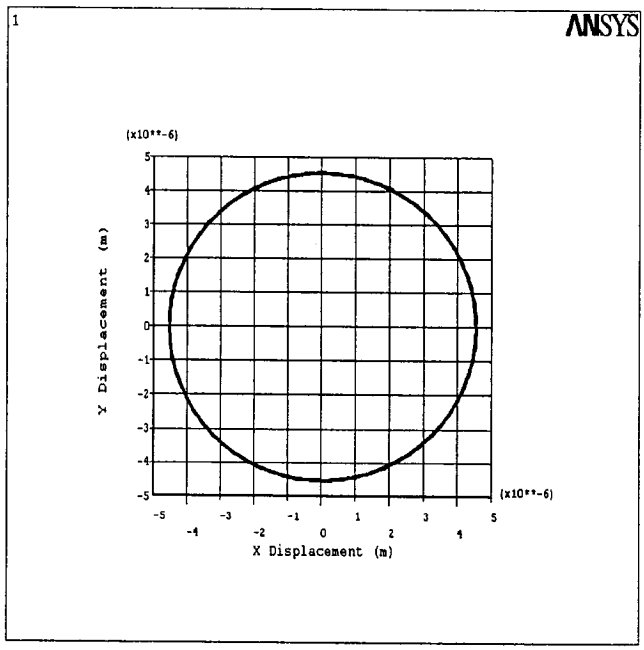

Figure 4.4.2p: Orbital Plot for $\lambda = 0, \phi = 0.1$, Imbalance Force Amplitude = 50 N and Forcing Frequency = 187.87 rad/sec at Spindle (node 4)

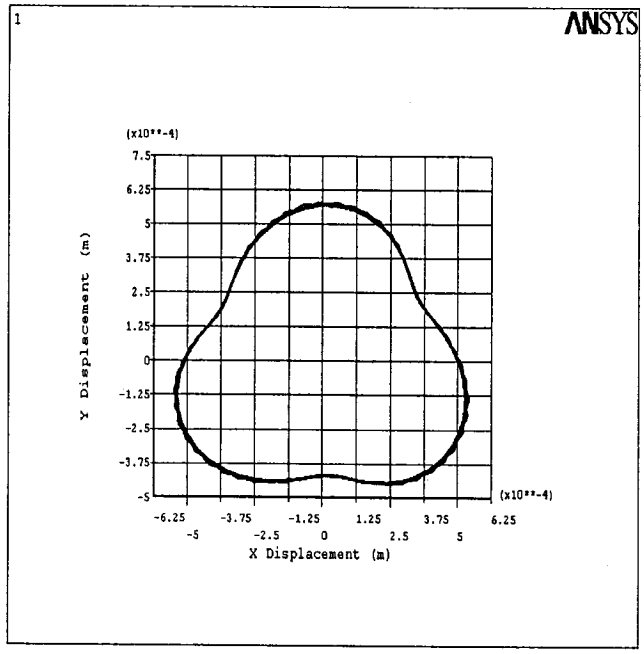

Figure 4.4.2q: Orbital Plot for $\lambda = 0.1, \phi = 0.1$, Imbalance Force Amplitude = 50 N and Forcing Frequency = 187.87 rad/sec at Drill Tip (node 9)

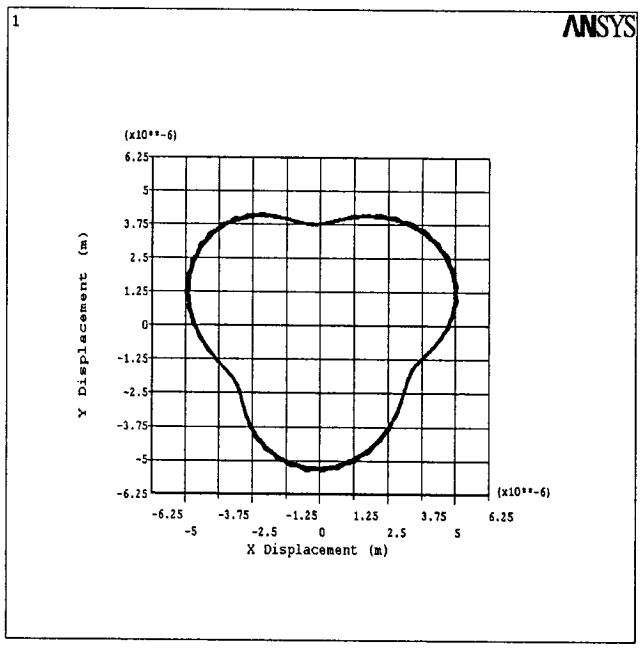

Figure 4.4.2r: Orbital Plot for $\lambda = 0.1, \phi = 0.1$, Imbalance Force Amplitude = 50 N and Forcing Frequency = 187.87 rad/sec at Spindle (node 4)

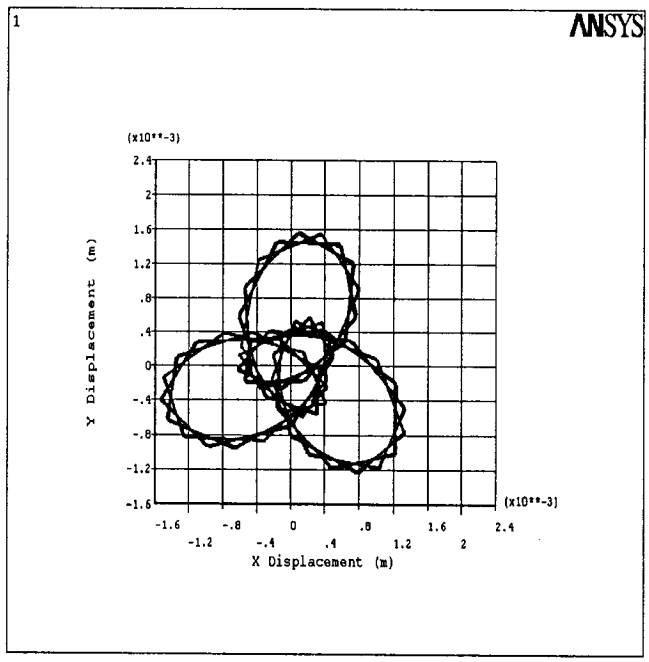

Figure 4.4.2s: Orbital Plot for $\lambda = 1.3, \phi = 0.1$, Imbalance Force Amplitude = 50 N and Forcing Frequency = 187.87 rad/sec at Drill Tip (node 9)

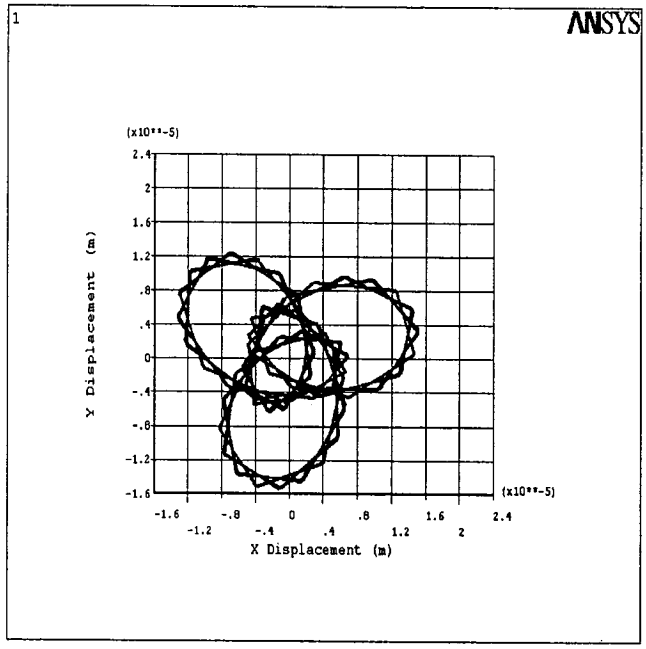

Figure 4.4.2t: Orbital Plot for $\lambda = 1.3, \phi = 0.1$, Imbalance Force Amplitude = 50 N and Forcing Frequency = 187.87 rad/sec at Spindle (node 4)

A similar kind of simulation results are presented in the figures 4.4.2o to 4.4.2t, by considering imbalance force amplitude of 50 N and forcing frequency of 187.87 rad/sec, by varying the amplitude modulation factor λ. Figure 4.4.2q and 4.4.2r represent the orbits obtained at node 9 and node 4, respectively for a modulation factor of 0.1. Figures 4.4.2s and 4.4.2t represents the orbit obtained with the modulation factor of 1.3.

4.4.3 With Belt Tension

In this part the transient analysis is performed considering the belt tensions acting on the multiple diameter pulley in order to study the effect of belt tensions on the lateral displacement at dill tip. The multiple diameter pulley is driven by 4L430C 2T type standard V-belt. The following relations are employed [45] for finding the tight side and slack side tensions T_1, and T_2 respectively as shown in the figure 4.4.3.

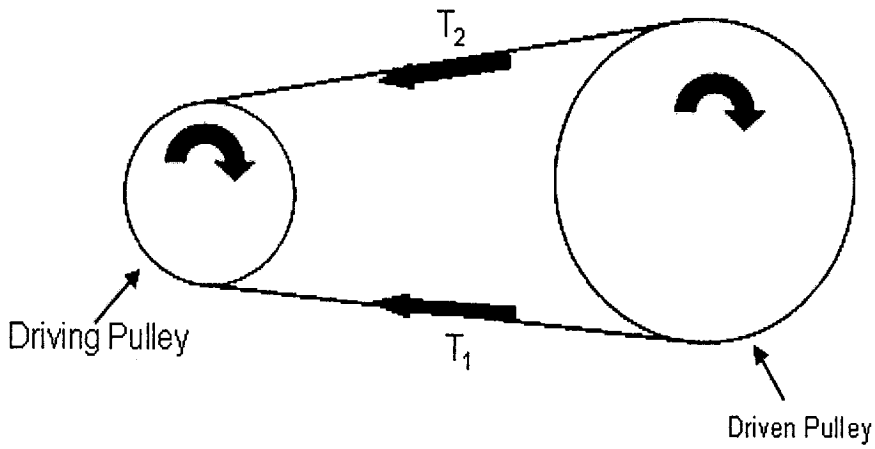

Figure 4.4.3: Schematic of Belt Drive Pulley

$$\left(\frac{T_1}{T_2}\right) = e^{\frac{\mu' \theta}{\sin \beta^*}} \quad \text{and} \quad P = (T_1 - T_2)\, v$$

where, μ' is the coefficient of friction between the belt and sides of the groove, θ is the angle of wrap, $2\beta^*$ is the angle of V-groove, P is the power transmitted, v is the velocity of the belt. The tensions evaluated for power transmission of 745.6 watt and for different speeds are given in the table 4.4.3.

Table 4.4.3: Tensions for Different speeds

Speed rpm / rad sec^{-1}	Diameter of Driving Pulley (mm)	Diameter of Driven Pulley (mm)	Tension (N)	
			Tight Side Tension T_1 (N)	Slack Side Tension T_2 (N)
445 / 46.57	23	120	417.9	151.04
930/97.34	46	100	235.04	81.28
1795/187.84	74	74	159.89	53.299

4.4.4 Results

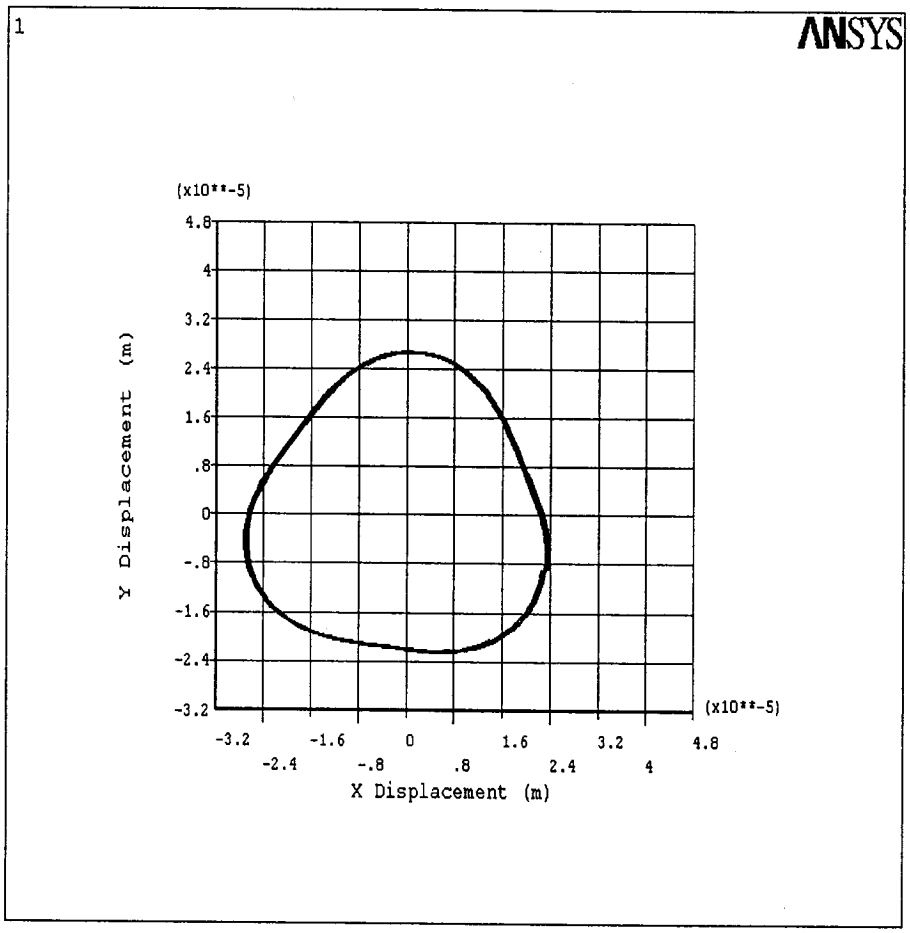

Figure 4.4.4a: Orbital Plot at Drill Tip (node 9) for $\lambda = 0.1, \phi = 0.1$, Imbalance Force Amplitude = 2.5 N and Forcing Frequency = 46.57 rad/sec with the Component of Belt Tensions acting (node 2)

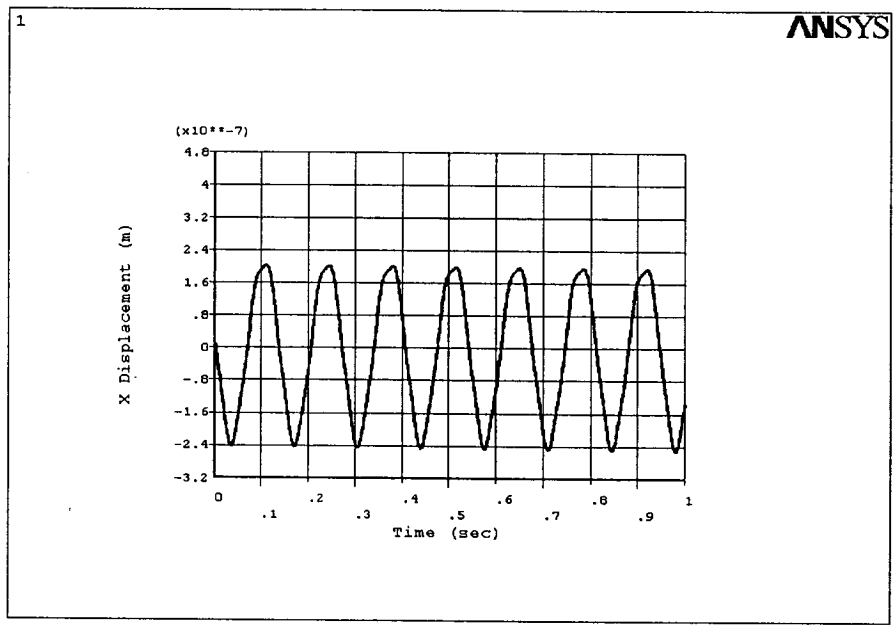

Figure 4.4.4b: Time-Displacement Response at Spindle (node 4) in X- Direction for $\lambda = 0$, $\phi = 0.1$ Imbalance Force Amplitude = 2.5 N and Forcing Frequency = 46.57 rad/sec with the Component of Belt Tensions acting (node 2)

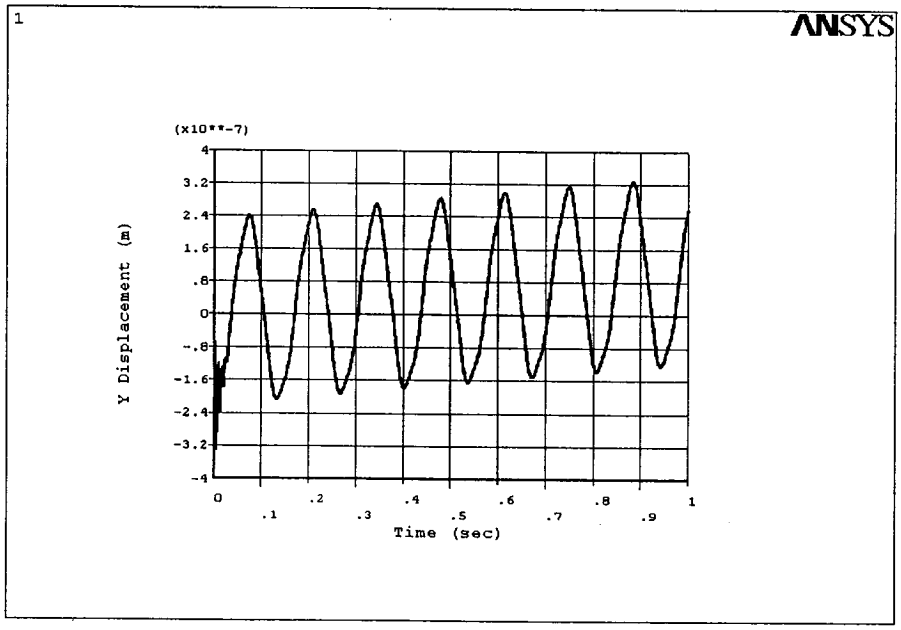

Figure 4.4.4c: Time-Displacement Response at Spindle (node 4) in Y-Direction for $\lambda = 0$, $\phi = 0.1$ Imbalance Force Amplitude = 2.5 N and Forcing Frequency = 46.57 rad/sec with the Component of Belt Tensions acting (node 2)

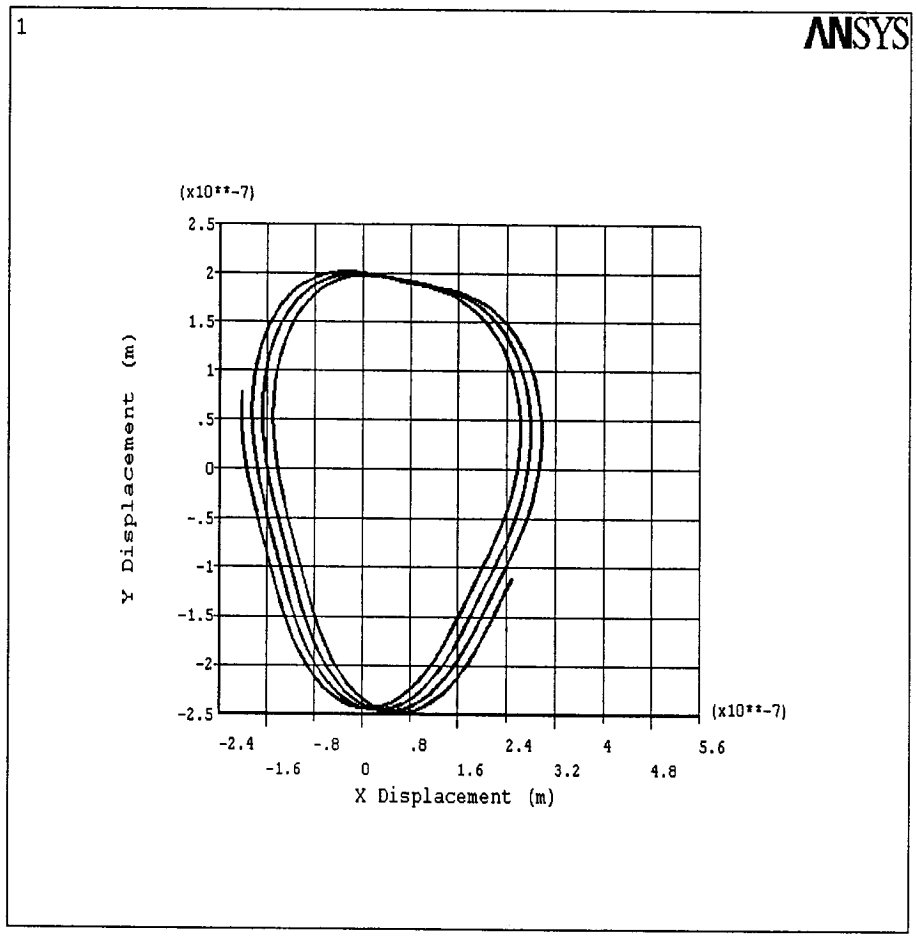

Figure 4.4.4d: Orbital Plot at Spindle (node 4) for $\lambda = 0.1, \phi = 0.1$, Imbalance Force Amplitude = 2.5 N and Forcing Frequency = 46.57 rad/sec with the Component of Belt Tensions acting (node 2)

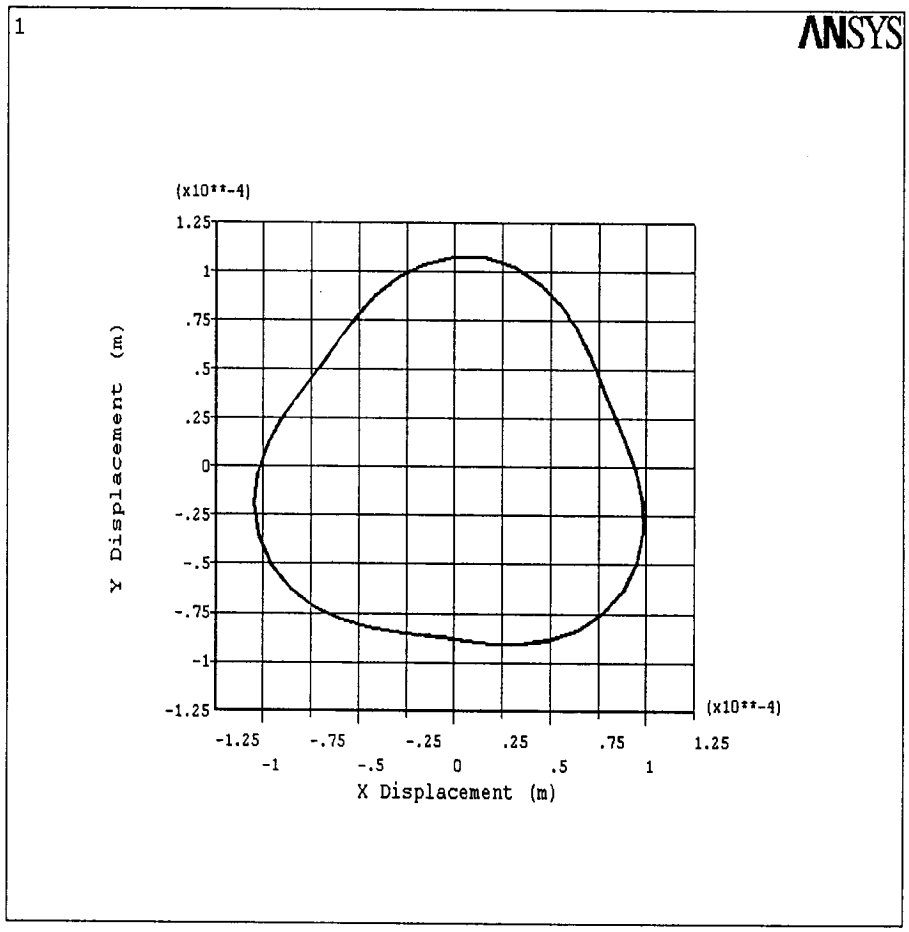

Figure 4.4.4e: Orbital Plot at Drill Tip (node 9) for $\lambda = 0.1, \phi = 0.1$, Imbalance Force Amplitude = 10 N and Forcing Frequency = 97.34 rad/sec with the Component of Belt Tensions acting (node 2)

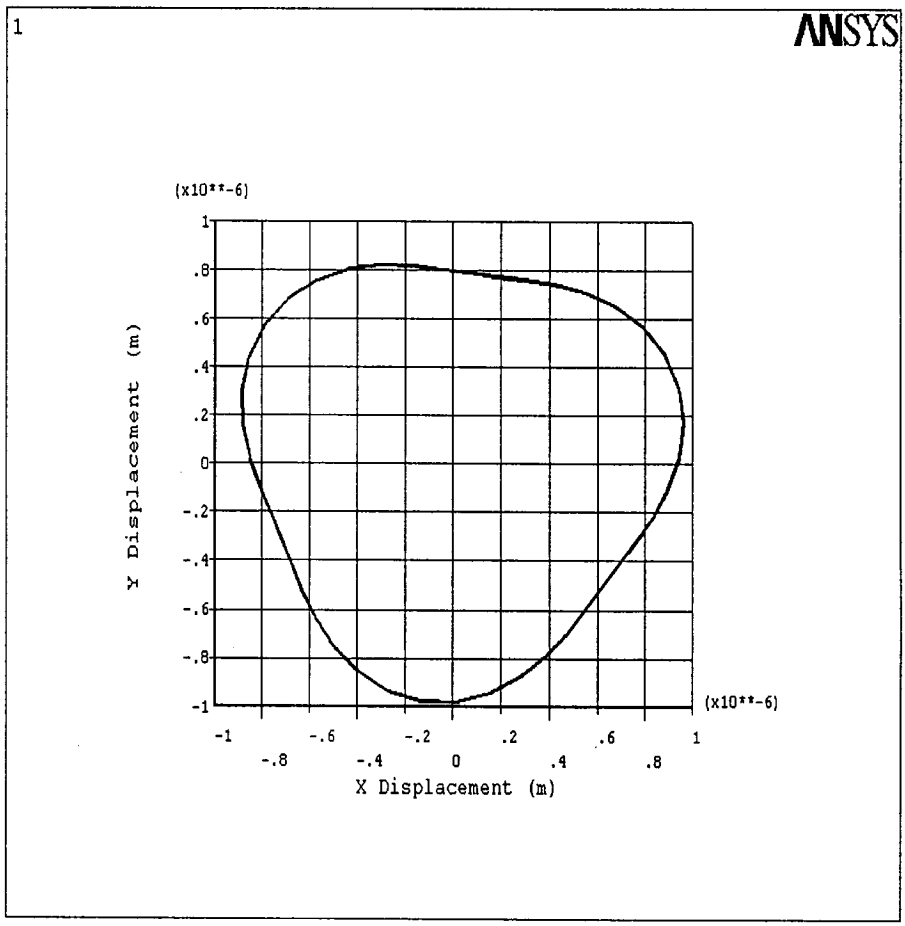

Figure 4.4.4f: Orbital Plot at Spindle (node 4) for λ=0.1, ϕ = 0.1, Imbalance Force Amplitude =10 N and Forcing Frequency = 97.34 rad/sec with the Component of Belt Tensions acting (node 2)

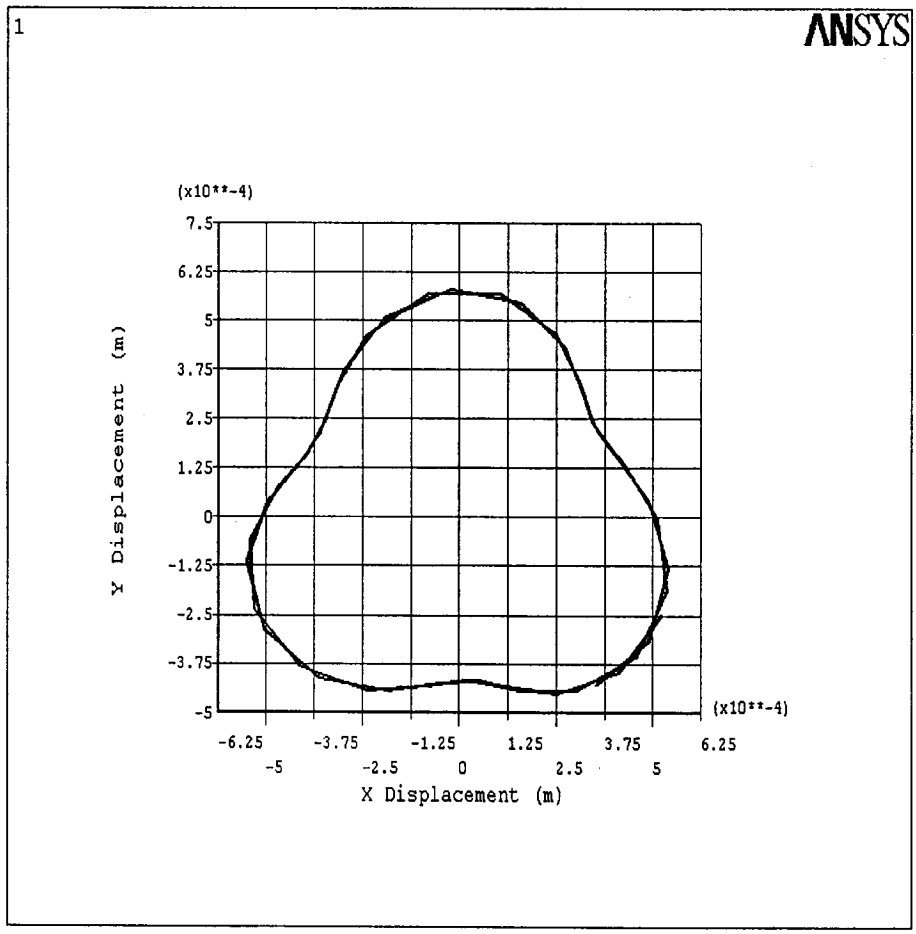

Figure 4.4.4g: Orbital Plot at Drill Tip (node 9) for λ=0.1, ϕ = 0.1, Imbalance Force Amplitude = 50 N and Forcing Frequency = 187.84 rad/sec with the Component of Belt Tensions acting at (node 2)

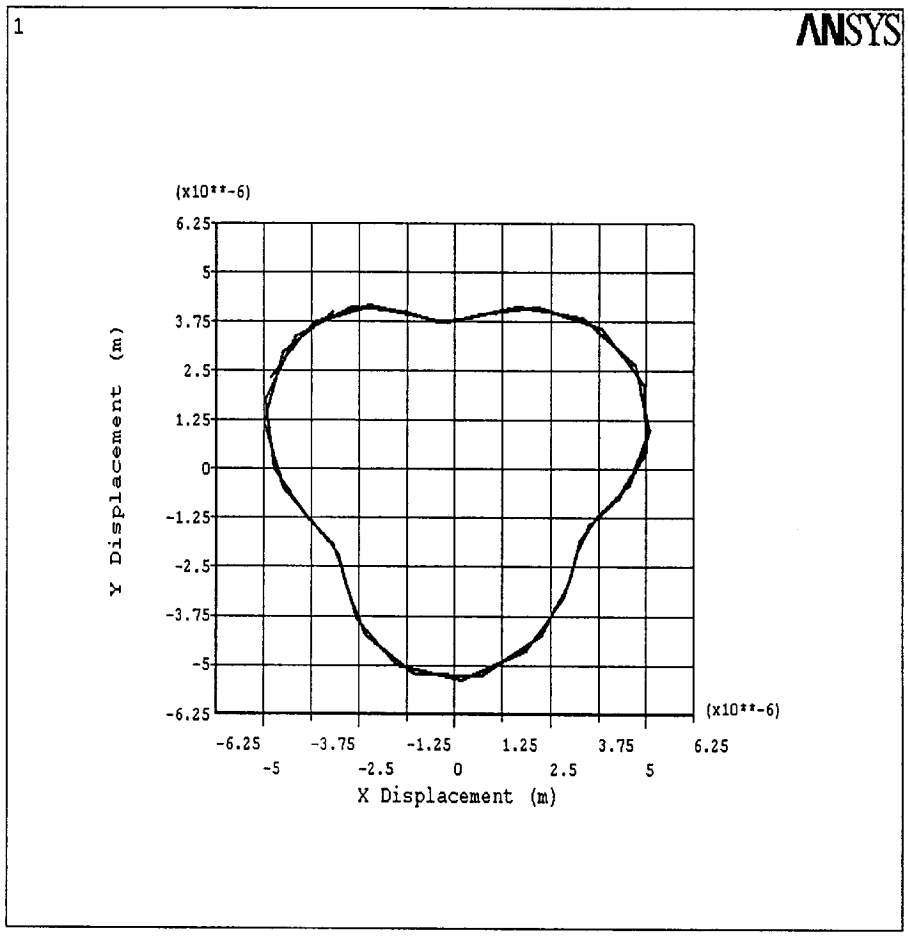

Figure 4.4.4h: Orbital Plot at Spindle (node 4) for λ=0.1, ϕ = 0.1, Imbalance Force Amplitude = 50 N and Forcing Frequency = 187.84 rad/sec with the Component of Belt Tensions acting at (node 2)

Figure 4.4.4a shows the orbit obtained at the end of the drill tip with the same simulation parameters used as that of for the figure 4.4.2e with an addition of belt tensions acting at node 2, since the belt tensions T_1 and T_2 are acting at an angle, the component of forces are applied at node 2 in X and Y directions respectively. One can observe by comparing the figures 4.4.2e and 4.4.4a that the belt tensions did not affect the drill displacement at the tip. Where as the orbit obtained at node 4 as shown in the figure 4.4.4d has an affect compared with the case of without belt tension in the figure 4.4.2f. The orbit is more stable in the latter case but the amplitude of the whirl remains almost same in both the cases. Figure 4.4.4e to 4.4.4h shows the orbits obtained for various combinations of parameters with an addition of belt tension acting at node 2. In all the cases the belt tension has no significant affect on the drill tip displacement.

4.5 Summary

A finite element model is developed considering the complete assembly of Drill-Shaft-Drive assembly. Modal analysis was performed for the finite element model in order to validate the actual system. Transient analysis is also performed in order to study the dynamics of the system, considering the system excited by the cutting force imbalance. The results are presented and discussed.

CHAPTER 5

CONCLUSIONS AND RECOMMENDATIONS FOR FUTURE WORK

5.1 Summary

A two-dimensional mathematical model for the transverse motion of twist drill is formulated considering the combined system as a single mass rotating in a hole with clearance symmetrically supported by vertically sliding spindle housing, the spindle and the drill bit chuck as bilinear spring. The model is excited by a modulated imbalance cutting force generated at the cutting edges of the drill. The second order equations of motions are solved for the transverse displacements in x and y directions for various parameters. The x and y displacements are plotted for predicting the orbital shapes, which gives an insight into the twist drill transverse motion behavior. A series of experimental trials was done to study the instability arising in drill tool bit. The experimental investigation consists of estimation of spindle run-out relative to drill. Experiments were also carried out with drill tool inserted in the tool holder or chuck without performing the drilling operation and modal testing was done to find the fundamental bending frequency of combined machine tool system. The obtained natural frequency has been used as a basis for validating the finite element model of the drilling machine spindle-tool system. The finite element model is created considering the spindle, pulley, chuck, bearings and drill tool by measuring the actual dimensions of the machine system used for the experiment (as shown in figure 3.1).

Finally the cutting forces considered in the mathematical model are used to excite the total structure at the drill tip for the finite element model and the orbital plots are obtained at the drill tip as well as at the spindle, the effect of belt tensions on the structure are also studied.

5.1 Conclusions

The main conclusions that can be drawn from the present work are

1. The geometric quality of high-precision holes is highly dependent on the dynamic performance of the entire machining system, which can be determined by the interrelated dynamics of machine tool mechanical structure and cutting process.
2. The two-dimensional mathematical model is not enough to have a clear understanding of the effect of other machine elements on the drill transverse motions.
3. Experimental results reveal that the certain amount of spindle run-out is present in the system which causes the twist drill to rotate at an eccentricity which reflects on the hole-profile if drilled. It was also found that some amount of lateral motion present at the spindle. The effect of mass imbalance is not present in the system; this can be predicted from the orbits obtained by the free rotation of twist drill without cutting at different speeds.
4. The finite element model of the combined machine drill system can be helpful in predicting the behavior of the machine structure at the spindle when the drilling process is initiated.

5. The transient analysis performed considering the constant belt tensions acting on the pulley did not show significant effect on the displacements at drill tip.

5.1 Recommendations for Future Work

1. The present work can be extended considering the effect of cross coupling stiffness of bearing on the combined spindle-tool system.
2. Effect of coupled bending and torsion should be considered for the combined spindle-tool system and should be analyzed.
3. Present study considered no mass unbalance for the pulley and chuck, the effects of centrifugal forces due to belt drive are also neglected considering all these effects, one can have some more insight into the system.
4. Measuring the relative spindle displacements should be done using a LVDT transducers instead of accelerometers so that, proper correlation can be made between the displacements obtained at the spindle and the displacements measured at the drill tip, as the displacements at the drill tip are sensed by proximity sensors.
5. The effect of eccentric arrangement of the driving and the driven pulleys may result in time varying belt tensions coming on to the spindle; these forces can be considered and the spindle-tool system can be analyzed for transverse motions.
6. Further experimental validation is needed by performing the actual cutting process.

REFERENCES

1. D. F. Galloway, *"Some Experiments on the Influence of Various Factors on Drill Performance"*, 1957, Transactions of ASME, Journal of Engineering for Industry, Vol. 10, pp. 191-231.

2. C. H. Kahng, I. Ham, *"Study on Sequential Quality Improvement in Hole-making Processes"*, 1975, CIRP Annals, Vol. 24, pp. 27-32.

3. R. Venkatraman, J. Lambert, F. Koenigsberger, *"Analysis and Performance Testing of a Dynamometer for the use in Drilling and Allied Processes"*, 1965, International Journal of Machine Tool Design, Vol. 5, pp. 233-261.

4. M. Tsuwa, Y. Hasegawa, H. Kimura, *"On Walking Phenomenon of Drills"*, 1961, Transactions of Japan Society of Mechanical Engineers, Vol. 27, pp. 816-825.

5. M. W. Burnham, *"An Analysis of Drill Deflection for Deep Miniature Holes"*, 1980, Society of Manufacturing Engineers, Vol. 106, pp. 196-203.

6. M. W. Burnham, *"The Mechanics of Drilling Small Holes"*, 1982, Manufacturing Engineering Transactions, Vol. 101, pp. 65-68.

7. S. Kaldor, E. Lenz, *"Drill Point Geometry and Optimization"*, 1982, Transactions of ASME, Journal of Engineering for Industry, Vol. 105, pp. 173-182.

8. S. M. Wu, J. M. Shen, *"Mathematical Model for Multifacet Drills"*, 1983, Transactions of ASME, Journal of Engineering for Industry, Vol. 105, pp. 83-185.

9. T. R. Chandrupautla, W. D. Webster, *"Effect of Drill Geometry on the Deformation of Twist Drill"*, 1985, Proceedings of Twenty Fifth International MTDR Conference, Vol. 5, pp. 231-236.

10. J. Rotberg, A. Ber, *"A Method for Drilling Parameter Evaluation Applied for Drill Point Development"*, 1987, CIRP Annals, Vol. 36, pp. 21-25.

11. S. V. Muthukrishnaselvam, C. Sujatha, *"Twist Drill Deformation and Optimum Drill Geometry"*, 1994, Journal of Computers and Structures, Vol. 57, pp. 903-914.

12. E. J. A. Armarego, A. J. R. Smith, Z. J. Gong, *"Four Plane Facet Point Drills-Basic Design and Cutting Model Predictions"*, 1990, CIRP Annals, Vol. 39, pp. 41-45.

13. C. DE Beer, *"The Web Thickness of Twist Drills"*, 1992, CIRP Annals, Vol. 25, pp. 81-85.

14. A. G. Ulsoy, O. Tekinalp, *"Dynamic Modelling of Transverse Drill Bit Vibrations"*, 1984, CIRP Annals, Vol. 33, pp. 253-258.

15. M. Kronenberg, *"Grungzuge der Zerspanungslehre"*, 1963, Vol. 1 and 2, Second Edition, Springer-verlag, Berlin.

16. D. D. Rosard, *"Natural Frequencies of Twisted Cantilever Beams"*, 1952, Transactions of ASME, Journal of Engineering for Industry, Vol. 52-A-15, pp. 1-5.

17. B. Dawson, W. Carneige, *"Modal Curves of Pre-twisted Beams of Rectangular Cross-section"*, 1969, Journal of Mechanical Engineering Science, Vol. 11, pp. 1-13.

18. E. B. Magrab, D. E. Gilsinn, *"Buckling Loads and Natural Frequencies of Drill Bits and Fluted Cutters"*, 1984, Transactions of ASME, Journal of Engineering for Industry, Vol. 106, pp. 196-204.

19. J. C. MacBain, K.G. Harding, O. Tekinalp, *"Vibration Modes and Frequencies of Twist Drills using LASER Holographic Interferometry"*, 1985, Transactions of ASME, Production Engineering Division (Publication) PED, Vol. 18, pp. 1-10.

20. M. Kohring, *"Modal Analysis of Twist Drills"*, 1985, Proceedings of Third International Modal Analysis Conference, Vol. 2, pp. 1171-1177.

21. P. G. Reinhall, D. W. Storti, *"Modeling and Analysis of the Dynamics of a Drill Penetrating a Thin Plate"*, 1986, Journal of Applied Mechanics, Vol. 53, pp. 690-694.

22. A. G. Ulsoy, *"A Lumped Parameter Model for the Transverse Vibration of Drill Bits"*, 1987, Transactions of ASME, Journal of Engineering for Industry, Vol. 10, pp. 15-25.

23. H. Fujii, E. Marui, S. Ema, *"Whirling Vibration in Drilling. Part 1: Cause of Vibration and Role of Chisel Edge"*, 1986, Transactions of ASME, Journal of Engineering for Industry, Vol. 108, pp. 157-162.

24. H. Fujii, E. Marui, S. Ema, *"Whirling Vibration in Drilling. Part 2: Influence of Drill Geometries, Particularly of the Drill Flank, on the Initiation of Vibration"*, 1986, Transactions of ASME, Journal of Engineering for Industry, Vol. 108, pp. 163-167.

25. S. J. Lee, K. F. Eman, S. M. Wu, *"Analysis of Drill Wandering Motion"*, 1987, Transactions of ASME, Journal of Engineering for Industry, Vol. 109, pp. 297-305.

26. S. Ema, H. Fujii, E. Marui, *"Chatter Vibration in Drilling"*, 1988, Transactions of ASME, Journal of Engineering for Industry, Vol. 110, pp. 309-313.

27. O. Tekinalp, A. G. Ulsoy, *"Modeling and Finite Element Analysis of Drill Bit Vibrations"*, 1989, Transactions of ASME, Journal of Engineering for Industry, Vol. 111, pp. 148-155.

28. S. A. Basile, *"Modeling Transverse Motions of Drill Bit for Process Understanding"*, 1993, Precision Engineering, Vol. 15, pp. 258-265.

29. D. A. Stephenson, J. S. Agapiou, *"Calculation of Main Cutting Edge Forces and Torque for Drills with Arbitrary Point Geometries"*, 1991, International Journal of Machine Tool Manufacturing, Vol. 32, pp. 521-538.

30. D. M. Rincon, A. G. Ulsoy, *"Effects of Drill Vibrations on Cutting Forces and Torque"*, 1994, CIRP Annals, Vol. 43, pp. 59-62.

31. Z. Zhixiong, L. Cheng, *"Study on the Mechanism of Chatter Vibration of Initial Penetration in Drilling"*, 1999, Chinese Journal of Mechanical Engineering (English Edition), Vol. 12, pp. 135-141.

32. Z. Katz, A. Poustie, *"On the Hole Quality and Drill Wandering Relationship"*, 2001, International Journal of Manufacturing Technology, Vol. 17, pp. 233-237.

33. FAG and SKF Bearings Manual, 1998.

34. *"Non-contacting Displacement Measuring System, Instruction Manual of KD-2300, Kaman Instrumentation Operations"*, 1989, 3450 North Nevada Avenue, Colorado Springs, CO80907.

35. H. R. El-Sayed, *"Stiffness of Deep Groove Ball Bearings"*, 1980, *Wear*, Vol. 63, pp. 89-94.

36. M. Tiwari, K. Gupta, O. Prakash, *"Effect of Radial Internal Clearance of a Ball Bearing on the Dynamics of a Balanced Horizontal Rotor"*, 2000, Journal of Sound and Vibration, Vol. 238, pp. 723-756.

37. E. V. Bordatchev, *"Modeling and Parameter Identification of the Impulse Response Matrix of Mechanical Systems"*, 1998, Proceedings of SPIE, 3518, pp. 106-117.

38. E. V. Bordatchev, P. E. Orban, *"Machining Process as a Subject of Automatic Control"*, 1999, Proceedings of SPIE, 3833, pp. 59-68.

39. E. V. Bordatchev, R. Henriksen, *"State Space Modeling of Machine Tool Spindle using Subspace Identification"*, 1999, Proceedings of Second IASTED International Conference on Control and Application, Vol. 20, pp. 11-16.

40. S. Kaldor, E. Lenz, *"Drill Point Geometry and Optimization"*, 1981, ASME paper No: 81-WA / Prod-18.

41. S. Fujii, M. F. Devries, S. M. Wu, *"Analysis of Drill Geometry for Optimum Drill Design by Computer"*, 1970, Transactions of ASME, Journal of Engineering for Industry, Vol. 10, pp. 647-666.

42. I. Fried, *"Accuracy of Finite Element Eigen Problems"*, 1971, Journal of Sound and Vibration, Vol. 18, pp. 289-295.

43. J. N. Reddy, *"An Introduction to the Finite Element Method"*, 1993, Second Edition, McGraw Hill, Boston.

44. NASA, *"Load Analyses of Spacecraft and Payloads"*, 1996, NASA-STD-5002.

45. J. E. Shigley, L. D. Mitchell, *"Mechanical Engineering Design"*, 1983, McGraw-Hill Book Company, Japan.

APPENDIX

A1- Data Acquisition System (DAQ)

The DAQ card - 6025E series board which are high in performance multifunction analog, digital and timing I/O boards for PCI, PXI, PCMCIA, and compact PCI bus computers. The 6025E features 16 channels (eight differentials) of analog input, two channels of analog output, a 100-pin connector, and 32 lines and digital I/O. The 6025E features 16 channels of analog input, two channels of analog output, a 68-pin connector and eight lines of digital I/O.

These devices use the national instruments DAQ-STC system timing controller for time-related functions. The DAQ-STC consists of three timing groups that control analog input, analog output, and general-purpose counter/timer functions. These groups include a total of seven 24-bit and three 16-bit counters and a maximum timing resolution of 50 ns [34].

A2- Non-contacting Displacement Measuring System (KD-2300)

Kaman instrumentation's family is of displacement measuring systems, which uses inductive technology to determine the position of the target relative to the system sensor. There are many sensor models available for use with KD-2300 electronics and the standard performance. The specification of the sensors used in this study is listed in the table A.

Table A: The Standard Performance Specifications for 2S model [33].

Sensor Model	Measuring Range Inch (mm)	Typical offset Inch (mm)	Linearity % FS*	Analog Voltage V dc	Displacement Sensitivity mV/ mil (mm)
2S	0.100 (2.5)	0.010 (0.25)	1.00%	1.00(2.5)	10(100)

***Full Scale.**

A3- Twist drill Nomenclature

Various parts of the Drill, Measurements and Angles mentioned in the following nomenclature are illustrated in figure 1.1 [1].

Axis: The longitudinal central line.

Body: The part of the drill extending from the chisel edge to the shank end of the flutes.

Shank: The part of the drill by which it is held and driven.

Tang: The tongued portion of the end of the drill shank.

Flutes: The grooves in the body of the drill which provide lips and chip space.

Web: The central part of the drill situated between the roots of the flutes and extending from the point end towards the shank; the point end forms the chisel edge.

Lands: The cylindrically ground surfaces on the leading edges of the drill flutes. The width of the land is measured at right angles to flute helix.

Body clearance: The part of the body surface reduced in diameter to provide diametral clearance.

Heel: The edge formed by the intersection of the flute surface and the body clearance.

Point: The sharpened end of the drill, consisting of all that part of the drill which is shaped to produce lips, faces, flanks, and chisel edge.

Face: The part of the flute surface adjacent to the lip on which the chip impinges as it is cut from the work.

Flank: The surface or surfaces on a drill point which extend behind the lip to the following flute.

Relief flank: That part of the flank immediately adjacent to the lip.

Clearance flank: that part of the flank extending behind the relief flank.

Lip (cutting edge): The edge formed by the intersection of the flank and face.

Outer corner: the corner formed by the intersection of the lip and the leading edge of the land.

Chisel edge: The edge formed by the intersection of flanks.

Chisel-edge corner: The corner formed by the intersection of a lip and chisel edge.

Diametral flute shape: The profile of the flute in a specified plane at right angles to the axis of the drill.

Helical flute shape: The profile of the flute in a specified plane at right angles to the flute helix at the lands.

Measurements:

Diameter: The measurement over the lands at any specified distance from the shank end of the body.

Over-all length: The length over the extreme ends of the point and the shank.

Flute length: The axial length from the extreme end of the point to the termination of the flutes at the shank end of the body.

Lead of helix: The distance measured parallel to the drill axis between the corresponding points on the leading edge of a flute in one complete turn of the flute.

Back taper: The reduction in diameter per inch length of the drill point towards the shank.

Land height: the height of the land surface above the body surface behind the land, where it emerges with the land surface.

Web-thickness: The minimum dimension of the web measured at the point end of the drill.

Web taper: The increase in the web thickness per inch length from the point of the drill to the shank.

Lip length: The minimum distance between the outer corner and the chisel-edge corner of the lip.

Relative lip height: The axial displacement of the lips measured at a given radius and determined by the axial distance of the lips from a reference plane perpendicular to the drill axis.

Relief-flank width: The dimension (or angle) which defines the extent of the relief flank from the lip.

Point run-out: The radial run-out, with respect to the axis of the shank, of the circle containing the lands at the point end of the drill.

Percentage flute area: The sum of the areas of the flutes measured in a specified plane perpendicular to the drill axis expressed as a percentage area of a circle equal in diameter to the diameter of the drill in the specified plane.

Angles:

Helix angle: The acute angle between the leading edge of a land and drill axis.

Rake: The angle between the face and a plane parallel to the drill axis and the line joining the corresponding outer and chisel edge corners, measured in a plane perpendicular to this line.

Point angle: The sum of the acute angles between the drill axis and the lines joining each outer corner to the corresponding corners of the chisel edge.

Inclined relief angle: The angle between the relief flank and a surface generated by the corresponding lip as the drill rotates about its axis, measured around the surface of a cone whose included angle is supplementary to the drill point angle; i.e., around the surface of a cone coaxial with the center of the drill having an included angle of 180 deg minus drill-point angle and with its apex pointing toward the shank.

Nominal relief angle: The nominal relief angle is the angle between the relief flank and a plane perpendicular to the drill axis, measured in a plane parallel to the drill axis and perpendicular to the radius. The angle is usually measured from the lip.

Clearance angle: The clearance angle is the angle between the clearance flank and a plane perpendicular to the drill axis, measured in a plane parallel to the drill axis and perpendicular to a radius.

Chisel edge angle: The obtuse angle included by the chisel edge and a line from either outer corner to the corresponding end of the chisel edge; the angle is measured in a plane perpendicular to the drill axis.

Lip-spacing angle: The angle between the lips at any specified radius measured in a diametric plane.

A4- List of Nodal Displacements and Mass Participation Factors

The list of Nodal displacements is provided from pages 140 to 144 and the list of Mass Participation Factors are provided from pages 145 to 147.

Table 4.3.2a: Nodal Displacements for First Mode (155.955 Hz)

NODE	UX	UY	UZ	USUM
1	-2.28E-02	3.07E-04	0	2.28E-02
2	1.17E-03	-1.57E-05	0	1.17E-03
3	-1.46E-02	1.97E-04	0	1.46E-02
4	-3.11E-02	4.18E-04	0	3.11E-02
5	2.54E-02	-3.41E-04	0	2.54E-02
6	0.21974	-2.96E-03	0	0.21976
7	0.47613	-6.40E-03	0	0.47618
8	0.6845	-9.21E-03	0	0.68456
9	2.7273	-3.67E-02	0	2.7275
10	0	0	0	0
11	0	0	0	0
12	0	0	0	0
13	0	0	0	0
14	0	0	0	0
15	0	0	0	0
NODE	ROTX	ROTY	ROTZ	RSUM
1	7.15E-03	0.53176	0	0.53181
2	7.14E-03	0.53114	0	0.53119
3	-1.99E-02	-1.4791	0	1.4793
4	7.00E-02	5.2034	0	5.2039
5	8.33E-02	6.1943	0	6.1948
6	0.11473	8.5307	0	8.5315
7	0.13756	10.228	0	10.229
8	0.16888	12.557	0	12.558
9	0.21351	15.876	0	15.877
10	0	0	0	0
11	0	0	0	0
12	0	0	0	0
13	0	0	0	0
14	0	0	0	0
15	0	0	0	0

Table 4.3.2b: Nodal Displacements for Second Mode (155.955 Hz)

NODE	UX	UY	UZ	USUM
1	3.07E-04	2.28E-02	0	2.28E-02
2	-1.57E-05	-1.17E-03	0	1.17E-03
3	1.97E-04	1.46E-02	0	1.46E-02
4	4.18E-04	3.11E-02	0	3.11E-02
5	-3.41E-04	-2.54E-02	0	2.54E-02
6	-2.96E-03	-0.21974	0	0.21976
7	-6.40E-03	-0.47613	0	0.47618
8	-9.21E-03	-0.6845	0	0.68456
9	-3.67E-02	-2.7273	0	2.7275
10	0	0	0	0
11	0	0	0	0
12	0	0	0	0
13	0	0	0	0
14	0	0	0	0
15	0	0	0	0
NODE	ROTX	ROTY	ROTZ	RSUM
1	0.53176	-7.15E-03	0	0.53181
2	0.53114	-7.14E-03	0	0.53119
3	-1.4791	1.99E-02	0	1.4793
4	5.2034	-7.00E-02	0	5.2039
5	6.1943	-8.33E-02	0	6.1948
6	8.5307	-0.11473	0	8.5315
7	10.228	-0.13756	0	10.229
8	12.557	-0.16888	0	12.558
9	15.876	-0.21351	0	15.877
10	0	0	0	0
11	0	0	0	0
12	0	0	0	0
13	0	0	0	0
14	0	0	0	0
15	0	0	0	0

Table 4.3.2c: Nodal Displacements for Third Mode (505.637 Hz)

NODE	UX	UY	UZ	USUM
1	-3.15E-02	-3.84E-02	0	4.96E-02
2	7.43E-04	9.06E-04	0	1.17E-03
3	-1.25E-02	-1.52E-02	0	1.97E-02
4	8.35E-03	1.02E-02	0	1.32E-02
5	6.14E-02	7.48E-02	0	9.67E-02
6	0.23408	0.28522	0	0.36897
7	0.40258	0.49054	0	0.63459
8	0.42736	0.52072	0	0.67364
9	-2.64	-3.2168	0	4.1614
10	0	0	0	0
11	0	0	0	0
12	0	0	0	0
13	0	0	0	0
14	0	0	0	0
15	0	0	0	0
NODE	ROTX	ROTY	ROTZ	RSUM
1	-0.87251	0.71606	0	1.1287
2	-0.86154	0.70706	0	1.1145
3	1.6289	-1.3369	0	2.1073
4	-5.9988	4.9232	0	7.7603
5	-7.0095	5.7526	0	9.0678
6	-8.1437	6.6835	0	10.535
7	-6.0254	4.945	0	7.7947
8	4.2682	-3.5029	0	5.5216
9	36.285	-29.779	0	46.94
10	0	0	0	0
11	0	0	0	0
12	0	0	0	0
13	0	0	0	0
14	0	0	0	0
15	0	0	0	0

Table 4.3.2d: Nodal Displacements for Fourth Mode (505.637 Hz)

NODE	UX	UY	UZ	USUM
1	3.84E-02	-3.15E-02	0	4.96E-02
2	9.06E-04	-7.43E-04	0	1.17E-03
3	1.52E-02	-1.25E-02	0	1.97E-02
4	1.02E-02	-8.35E-03	0	1.32E-02
5	7.48E-02	-6.14E-02	0	9.67E-02
6	0.28522	-0.23408	0	0.36897
7	0.49054	-0.40258	0	0.63459
8	0.52072	-0.42736	0	0.67364
9	3.2168	-2.64	0	4.1614
10	0	0	0	0
11	0	0	0	0
12	0	0	0	0
13	0	0	0	0
14	0	0	0	0
15	0	0	0	0
NODE	ROTX	ROTY	ROTZ	RSUM
1	-0.71606	-0.87251	0	1.1287
2	-0.70706	-0.86154	0	1.1145
3	1.3369	1.6289	0	2.1073
4	-4.9232	-5.9988	0	7.7603
5	-5.7526	-7.0095	0	9.0678
6	-6.6835	-8.1437	0	10.535
7	-4.945	-6.0254	0	7.7947
8	3.5029	4.2682	0	5.5216
9	29.779	36.285	0	46.94
10	0	0	0	0
11	0	0	0	0
12	0	0	0	0
13	0	0	0	0
14	0	0	0	0
15	0	0	0	0

Table 4.3.2e: Nodal Displacements for Fifth Mode (799.74 Hz)

NODE	UX	UY	UZ	USUM
1	-0.32702	1.775	0	1.8049
2	-8.78E-03	4.77E-02	0	4.85E-02
3	2.48E-02	-0.13485	0	0.13712
4	-1.01E-02	5.49E-02	0	5.58E-02
5	-6.52E-03	3.54E-02	0	3.60E-02
6	-2.22E-03	1.20E-02	0	1.22E-02
7	-2.69E-03	1.46E-02	0	1.48E-02
8	-5.47E-03	2.97E-02	0	3.02E-02
9	3.05E-02	-0.1657	0	0.16849
10	0	0	0	0
11	0	0	0	0
12	0	0	0	0
13	0	0	0	0
14	0	0	0	0
15	0	0	0	0
NODE	ROTX	ROTY	ROTZ	RSUM
1	38.55	7.1025	0	39.199
2	37.263	6.8654	0	37.891
3	-10.931	-2.014	0	11.115
4	2.0839	0.38395	0	2.119
5	1.599	0.29459	0	1.6259
6	0.36379	6.70E-02	0	0.36992
7	-0.38289	-7.05E-02	0	0.38934
8	-1.026	-0.18902	0	1.0432
9	2.4345	0.44854	0	2.4755
10	0	0	0	0
11	0	0	0	0
12	0	0	0	0
13	0	0	0	0
14	0	0	0	0
15	0	0	0	0

Table 4.3.2f: Nodal Displacements for Sixth Mode (799.74 Hz)

NODE	UX	UY	UZ	USUM
1	-1.775	-0.32702	0	1.8049
2	-4.77E-02	-8.78E-03	0	4.85E-02
3	0.13485	2.48E-02	0	0.13712
4	-5.49E-02	-1.01E-02	0	5.58E-02
5	-3.54E-02	-6.52E-03	0	3.60E-02
6	-1.20E-02	-2.22E-03	0	1.22E-02
7	-1.46E-02	-2.69E-03	0	1.48E-02
8	-2.97E-02	-5.47E-03	0	3.02E-02
9	0.1657	3.05E-02	0	0.16849
10	0	0	0	0
11	0	0	0	0
12	0	0	0	0
13	0	0	0	0
14	0	0	0	0
15	0	0	0	0
NODE	ROTX	ROTY	ROTZ	RSUM
1	-7.1025	38.55	0	39.199
2	-6.8654	37.263	0	37.891
3	2.014	-10.931	0	11.115
4	-0.38395	2.0839	0	2.119
5	-0.29459	1.599	0	1.6259
6	-6.70E-02	0.36379	0	0.36992
7	7.05E-02	-0.38289	0	0.38934
8	0.18902	-1.026	0	1.0432
9	-0.44854	2.4345	0	2.4755
10	0	0	0	0
11	0	0	0	0
12	0	0	0	0
13	0	0	0	0
14	0	0	0	0
15	0	0	0	0

Table 4.3.2g: Nodal Displacements for Seventh Mode (935.12 Hz)

NODE	UX	UY	UZ	USUM
1	6.56E-03	-6.09E-02	0	6.12E-02
2	3.97E-04	-3.68E-03	0	3.71E-03
3	-2.56E-03	2.37E-02	0	2.39E-02
4	9.80E-03	-9.10E-02	0	9.15E-02
5	1.72E-02	-0.1597	0	0.16063
6	3.97E-02	-0.36816	0	0.37029
7	4.89E-02	-0.45342	0	0.45604
8	1.79E-02	-0.16564	0	0.1666
9	0.26829	-2.4896	0	2.504
10	0	0	0	0
11	0	0	0	0
12	0	0	0	0
13	0	0	0	0
14	0	0	0	0
15	0	0	0	0
NODE	ROTX	ROTY	ROTZ	RSUM
1	-1.2797	-0.13791	0	1.2872
2	-1.2189	-0.13136	0	1.226
3	-0.91612	-9.87E-02	0	0.92143
4	6.443	0.69434	0	6.4803
5	7.3855	0.79591	0	7.4282
6	6.2852	0.67733	0	6.3216
7	-2.269	-0.24452	0	2.2821
8	-33.165	-3.5741	0	33.357
9	37.369	4.0271	0	37.585
10	0	0	0	0
11	0	0	0	0
12	0	0	0	0
13	0	0	0	0
14	0	0	0	0
15	0	0	0	0

Table 4.3.2h: Nodal Displacements for Eight Mode (935.12 Hz)

NODE	UX	UY	UZ	USUM
1	6.09E-02	6.56E-03	0	6.12E-02
2	3.68E-03	3.97E-04	0	3.71E-03
3	-2.37E-02	-2.56E-03	0	2.39E-02
4	9.10E-02	9.80E-03	0	9.15E-02
5	0.1597	1.72E-02	0	0.16063
6	0.36816	3.97E-02	0	0.37029
7	0.45342	4.89E-02	0	0.45604
8	0.16564	1.79E-02	0	0.1666
9	2.4896	0.26829	0	2.504
10	0	0	0	0
11	0	0	0	0
12	0	0	0	0
13	0	0	0	0
14	0	0	0	0
15	0	0	0	0
NODE	ROTX	ROTY	ROTZ	RSUM
1	0.13791	-1.2797	0	1.2872
2	0.13136	-1.2189	0	1.226
3	9.87E-02	-0.91612	0	0.92143
4	-0.69434	6.443	0	6.4803
5	-0.79591	7.3855	0	7.4282
6	-0.67733	6.2852	0	6.3216
7	0.24452	-2.269	0	2.2821
8	3.5741	-33.165	0	33.357
9	-4.0271	37.369	0	37.585
10	0	0	0	0
11	0	0	0	0
12	0	0	0	0
13	0	0	0	0
14	0	0	0	0
15	0	0	0	0

Table 4.3.2i: Nodal Displacements for Ninth Mode (1966 Hz)

NODE	UX	UY	UZ	USUM
1	0.31468	0.43202	0	0.53448
2	0.19707	0.27055	0	0.33472
3	-0.34975	-0.48017	0	0.59405
4	-0.71663	-0.98386	0	1.2172
5	-0.48953	-0.67207	0	0.83146
6	-0.16181	-0.22214	0	0.27483
7	-4.12E-02	-5.65E-02	0	7.00E-02
8	-4.01E-02	-5.50E-02	0	6.81E-02
9	2.71E-02	3.71E-02	0	4.60E-02
10	0	0	0	0
11	0	0	0	0
12	0	0	0	0
13	0	0	0	0
14	0	0	0	0
15	0	0	0	0
NODE	ROTX	ROTY	ROTZ	RSUM
1	3.9966	-2.9111	0	4.9444
2	1.8015	-1.3122	0	2.2288
3	32.869	-23.941	0	40.664
4	-31.995	23.305	0	39.583
5	-26.207	19.089	0	32.423
6	-11.149	8.1208	0	13.793
7	-3.5105	2.557	0	4.343
8	-0.31605	0.23021	0	0.391
9	-1.2601	0.91785	0	1.559
10	0	0	0	0
11	0	0	0	0
12	0	0	0	0
13	0	0	0	0
14	0	0	0	0
15	0	0	0	0

Table 4.3.2j: Nodal Displacements for Tenth Mode (1966 Hz)

NODE	UX	UY	UZ	USUM
1	-0.43202	0.31468	0	0.53448
2	-0.27055	0.19707	0	0.33472
3	0.48017	-0.34975	0	0.59405
4	0.98386	-0.71663	0	1.2172
5	0.67207	-0.48953	0	0.83146
6	0.22214	-0.16181	0	0.27483
7	5.65E-02	-4.12E-02	0	7.00E-02
8	5.50E-02	-4.01E-02	0	6.81E-02
9	-3.71E-02	2.71E-02	0	4.60E-02
10	0	0	0	0
11	0	0	0	0
12	0	0	0	0
13	0	0	0	0
14	0	0	0	0
15	0	0	0	0
NODE	ROTX	ROTY	ROTZ	RSUM
1	2.9111	3.9966	0	4.9444
2	1.3122	1.8015	0	2.2288
3	23.941	32.869	0	40.664
4	-23.305	-31.995	0	39.583
5	-19.089	-26.207	0	32.423
6	-8.1208	-11.149	0	13.793
7	-2.557	-3.5105	0	4.343
8	-0.23021	-0.31605	0	0.391
9	-0.91785	-1.2601	0	1.559
10	0	0	0	0
11	0	0	0	0
12	0	0	0	0
13	0	0	0	0
14	0	0	0	0
15	0	0	0	0

Table 4.3.2k: Mass Participation Factor in X- Direction

Mode	Cumulative Frequency (Hz) / Mass Fraction	Period	Participation Factor	Ratio	Effective Mass
1	155.955	6.41E-03	0.88524	1	0.783645
	0.683796				
2	155.955	6.41E-03	-1.19E-02	0.013449	1.42E-04
	0.68392				
3	505.637	1.98E-03	0.31042	0.350666	9.64E-02
	0.768004				
4	505.637	1.98E-03	-0.37824	0.427279	0.143068
	0.892842				
5	799.774	1.25E-03	-1.09E-02	0.01227	1.18E-04
	0.892945				
6	799.774	1.25E-03	-5.90E-02	0.066596	3.48E-03
	0.895978				
7	935.12	1.07E-03	2.80E-02	0.031662	7.86E-04
	0.896663				
8	935.12	1.07E-03	0.26008	0.293798	6.76E-02
	0.955687				
9	1966	5.09E-04	-0.13268	0.14988	1.76E-02
	0.971047				
10	1966	5.09E-04	0.18215	0.205769	3.32E-02
	1				

Table 4.3.2l: Mass Participation Factor in R_X- Direction

Mode	Cumulative Frequency / Mass Fraction	Period	Participation Factor	Ratio	Effective Mass
1	155.955	6.41E-03	-1.22E-03	0.013449	1.48E-06
	7.18E-05				
2	155.955	6.41E-03	-9.05E-02	1	8.19E-03
	0.396922				
3	505.637	1.98E-03	6.78E-02	0.7487	4.59E-03
	0.619378				
4	505.637	1.98E-03	5.56E-02	0.614455	3.09E-03
	0.769211				
5	799.774	1.25E-03	4.30E-02	0.475359	1.85E-03
	0.858886				
6	799.774	1.25E-03	-7.93E-03	0.08758	6.28E-05
	0.8619304				
7	935.12	1.07E-03	-5.19E-02	0.573327	2.69E-03
	0.992376				
8	935.12	1.07E-03	5.59E-03	0.061786	3.13E-05
	0.993891				
9	1966	5.09E-04	9.08E-03	0.100286	8.24E-05
	0.997882				
10	1966	5.09E-04	6.61E-03	0.073048	4.37E-05
	1				

Table 4.3.2m: Mass Participation Factor in Y- Direction

Mode	Cumulative Frequency / Mass Fraction	Period	Participation Factor	Ratio	Effective Mass
1	155.955	6.41E-03	-1.19E-02	0.013449	1.42E-04
	1.24E-04				
2	155.955	6.41E-03	-0.88524	1	0.783645
	0.68392				
3	505.637	1.98E-03	0.37824	0.427279	0.143068
	0.808758				
4	505.637	1.98E-03	0.31042	0.350666	9.64E-02
	0.892842				
5	799.774	1.25E-03	5.90E-02	0.066596	3.48E-03
	0.895875				
6	799.774	1.25E-03	-1.09E-02	0.01227	1.18E-04
	0.895978				
7	935.12	1.07E-03	-0.26008	0.293798	6.76E-02
	0.955001				
8	935.12	1.07E-03	2.80E-02	0.031662	7.86E-04
	0.955687				
9	1966	5.09E-04	-0.18215	0.205769	3.32E-02
	0.984639				
10	1966	5.09E-04	-0.13268	0.14988	1.76E-02
	1				

Table 4.3.2n: Mass Participation Factor in R_Y- Direction

Mode	Cumulative Frequency / Mass Fraction	Period	Participation Factor	Ratio	Effective Mass
1	155.955	6.41E-03	-9.05E-02	1	8.19E-03
	0.396851				
2	155.955	6.41E-03	1.22E-03	0.013449	1.48E-06
	0.396922				
3	505.637	1.98E-03	-5.56E-02	0.614455	3.09E-03
	0.546755				
4	505.637	1.98E-03	6.78E-02	0.7487	4.59E-03
	0.769211				
5	799.774	1.25E-03	7.93E-03	0.08758	6.28E-05
	0.772255				
6	799.774	1.25E-03	4.30E-02	0.475359	1.85E-03
	0.86193				
7	935.12	1.07E-03	-5.59E-03	0.061786	3.13E-05
	0.863445				
8	935.12	1.07E-03	-5.19E-02	0.573327	2.69E-03
	0.993891				
9	1966	5.09E-04	-6.61E-03	0.073048	4.37E-05
	0.996009				
10	1966	5.09E-04	9.08E-03	0.100286	8.24E-05
	1				

Table 4.3.2o: Mass Participation Factor in Z- Direction

Mode	Cumulative Frequency	Period	Participation Factor	Ratio	Effective Mass
	Mass Fraction				
1	155.955	6.41E-03	0	0	0
	0				
2	155.955	6.41E-03	0	0	0
	0				
3	505.637	1.98E-03	0	0	0
	0				
4	505.637	1.98E-03	0	0	0
	0				
5	799.774	1.25E-03	0	0	0
	0				
6	799.774	1.25E-03	0	0	0
	0				
7	935.12	1.07E-03	0	0	0
	0				
8	935.12	1.07E-03	0	0	0
	0				
9	1966	5.09E-04	0	0	0
	0				
10	1966	5.09E-04	0	0	0
	0				

Table 4.3.2p: Mass Participation Factor in R_Z- Direction

Mode	Cumulative Frequency	Period	Participation Factor	Ratio	Effective Mass
	Mass Fraction				
1	155.955	6.41E-03	0	0	0
	0				
2	155.955	6.41E-03	0	0	0
	0				
3	505.637	1.98E-03	0	0	0
	0				
4	505.637	1.98E-03	0	0	0
	0				
5	799.774	1.25E-03	0	0	0
	0				
6	799.774	1.25E-03	0	0	0
	0				
7	935.12	1.07E-03	0	0	0
	0				
8	935.12	1.07E-03	0	0	0
	0				
9	1966	5.09E-04	0	0	0
	0				
10	1966	5.09E-04	0	0	0
	0				